Optical Imaging Reveals Functional Network Architecture of Sensorimotor Cortex in Monkeys

by

Nicholas Scott Card

Bachelors of Science in Bioengineering, University of Pittsburgh

Swanson School of Engineering, 2016

Submitted to the Graduate Faculty of

the Swanson School of Engineering in partial fulfillment

of the requirements for the degree of

Doctor of Philosophy

University of Pittsburgh

2022

UNIVERSITY OF PITTSBURGH

SWANSON SCHOOL OF ENGINEERING

This dissertation was presented

by

Nicholas Scott Card

It was defended on

June 10, 2022

and approved by

Omar Gharbawie, PhD, Assistant Professor, Departments of Neurobiology and Bioengineering

Peter Strick, PhD, Thomas Detre Professor, Chair of the Department of Neurobiology

Aaron Batista,PhD, Professor, Department of Bioengineering

Alberto Vazquez, PhD, Associate Professor, Departments of Radiology and Bioengineering

Dissertation Director: Omar Gharbawie, PhD, Assistant Professor, Departments of Neurobiology and Bioengineering

Optical Imaging Reveals Functional Network Architecture of Sensorimotor Cortex in Monkeys

Nicholas Scott Card, PhD

University of Pittsburgh, 2022

Skilled movements require the coordination of neural activity throughout sensorimotor cortex. The most direct route of connectivity within and between sensorimotor cortical areas are corticocortical connections, which bind somatotopic regions of premotor cortex (PM), primary motor cortex (M1), and primary somatosensory cortex (S1). Although many such connections have been identified in previous work, the architecture of the functional network that they form is not clear due to limitations in connectivity tracing approaches. Consequently, how neural activity in sensorimotor cortex is coordinated in service of skilled movements is not known. The studies presented in this dissertation aimed to develop, benchmark, and utilize novel connectivity tracing approaches that were capable of identifying organizational features of connectivity in monkey sensorimotor cortex. Toward this objective, we used intrinsic signal optical imaging (ISOI) in stimulus-evoked and resting state paradigms to measure corticocortical connectivity throughout squirrel monkey sensorimotor cortex. ISOI was capable of measuring connectivity *in vivo* for a large number of cortical sites and at high spatial resolution. We benchmarked our connectivity results against neuroanatomical tracers, the gold standard of connectivity mapping, to show that ISOI accurately measured monosynaptic corticocortical connectivity. Next, we analyzed connectivity throughout sensorimotor cortex using supervised and unsupervised analyses to identify key organizational features of the sensorimotor network. Every point within sensorimotor cortex was preferentially connected to functionally matched zones spanning multiple cortical areas. Connectivity between non-matched functional zones was dependent on cortical area. Connections between motor and sensory areas mostly targeted proprioceptive sensory zones. These organizational features converge to grant insight into how the sensorimotor network contributes to the generation of skilled movements. Collectively, the studies presented here lay the foundation for measuring cortical network architecture at high spatial resolution.

Table of Contents

List of Tables

List of Figures

1.0 General Introduction

Movement is a central component of life that serves as the basis of any organism's ability to navigate its environment. Likewise, sensation informs an organism about itself and its surroundings. Together, movement and sensation enable an organism to interact with the world around it. Generating even the simplest voluntary movements requires intention, planning, and execution. Sensation guides all stages of movement through contextual information and error-correction signals. The neural basis of movement therefore necessitates the coordination of neural activity throughout many brain areas that are responsible for the integration and execution of motor control and sensation.

The primary forms of sensation that influence or guide motor control in primates are vision (Angel et al., 1970), cutaneous somatosensation (Moberg, 1962), and proprioceptive somatosensation (Ghez et al., 1995). Vision gives information about the environment and spatial locations of parts of the body that are within the visual field. Cutaneous somatosensation offers tactile information, which describes contact between the body and an object. Finally, proprioceptive somatosensation offers information about the body's location in space. These forms of sensation are integrated in the brain to enable fine motor control. Motor and sensory functions have been localized to a wide range of brain regions, including cortical areas, subcortical structures, and the cerebellum. Collectively, these brain regions contribute to making decisions about what actions to take, planning and timing motor commands toward that action, and executing those motor commands. In many of these regions, sensory and motor information are tightly intertwined and cointegrated. Interconnectivity between many of these brain regions forms a complex sensorimotor network, wherein closed-loop interactions are central to the generation of fine motor control.

In summary, sensory and motor systems in the brain work together to enable organisms to interact with the world. Connectivity within and between these brain areas is central to achieving the coordination necessary for fine motor control. Efforts to understand the neural basis of movement and sensation in humans and non-human primates have revealed some fundamental relationships between connectivity and function. However, how the complex

circuitry of the sensorimotor system enables this function remains unclear. This dissertation is focused on brain circuitry that gives rise to fine motor control in non-human primates. Toward this focus, I investigated the network structure of cortical sensorimotor areas: primary motor cortex (M1), primary somatosensory cortex (S1), and premotor cortex (PM), collectively referred to as "sensorimotor cortex". These brain areas are the strongest contributors to voluntary movement (He et al., 1993) and somatosensory signals that contribute to motor control through feedback and error correction (Bohlhalter et al., 2002; Gordon et al., 1995; LaMotte and Mountcastle, 1979; Moberg, 1962). Additionally, these brain areas have predictable somatotopic organizations that can be reliably mapped with well-established approaches. Finally, these cortical areas are easily accessible on the surface of the brain. For all of these reasons, sensorimotor cortex was the most approachable component of the sensorimotor system to investigate the relationship between connectivity and function.

The objective of the present dissertation is to identify relationships between connectivity and somatotopy in sensorimotor cortex, which contributes to fine motor control in non-human primates. In the following sections, I will discuss what is known so far about the functional organization and connectivity of the sensorimotor cortex, as well as the unknowns that preclude our understanding of sensorimotor network architecture. I will then elucidate the status quo as it pertains to connectivity mapping and the limitations of current approaches. Finally, I will describe the contributions of each of the subsequent chapters, and how they contribute to the overall objective of the dissertation.

1.1 Functional Organization of Sensorimotor Cortex

Sensorimotor cortical areas have three levels of organization: topographic, laminar, and columnar. The topographic organization of S1, M1 and PM is such that body parts are represented in distinct zones of cortex (i.e., somatotopy). Motor somatotopy can be mapped in the living brain using intracortical microstimulation (ICMS) (e.g., Stoney et al. (1968)). In this approach, a microelectrode is inserted into cortex and electrical stimulation elicits a motor response. S1 somatotopy can be mapped with multi-unit recordings (e.g., Kaas

et al. (1979)), where a recording electrode is inserted in the brain and neural responses to stimulation of the contralateral body are recorded. In primates, PM, M1, and S1 are somatotopically organized following a medial-lateral organization from leg to face (Godschalk et al., 1995; Gould et al., 1986; Mayer et al., 2019; Merzenich et al., 1978; Muakkassa and Strick, 1979; Padberg et al., 2005; Penfield and Boldrey, 1937; Welker et al., 1957)). The somatotopic organization of S1 involves minimal overlap between representations of different body parts. In contrast, somatotopy in M1 and PM has more overlap or intermingling of distinct representations (Schieber, 2001; Schieber and Hibbard, 1993). For example, motor representations of the arm and hand have been shown to be intermixed with one another in old world (Kwan et al., 1978; Park et al., 2001; Sessle and Wiesendanger, 1982) and new world monkeys (Dancause et al., 2008; Donoghue et al., 1992; Gould et al., 1986; Nudo and Milliken, 1996; Strick and Preston, 1982). In premotor areas, face zones are intermixed with arm and hand zones (Godschalk et al., 1995; Schieber, 2001). The amount of cortical territory occupied by each representation is proportional to the precision with which the pertinent body part is controlled in motor areas (Penfield and Boldrey, 1937), or by the sensitivity of receptive fields in S1.

Motor and sensory cortical areas also have laminar organization, wherein the cortex is composed of six layers, each with a characteristic distribution of cytoarchitecture (Ramón y Cajal, 1899). Connections between different types of neurons throughout the six layers form microcircuits that compose cortical columns, which are functional units of cortex (Hubel and Wiesel, 1963; Mountcastle, 1997). Columns receive afferent projections from other brain areas, and send efferent projections. For example, columns in S1 receive sensory information through dense thalamocortical inputs to layer IV. Columns in M1 and PM send motor outputs from layer V pyramidal neurons to influence muscles through the corticospinal or corticobulbar tracts (He et al., 1993). These examples serve as the primary inputs and outputs of cortex responsible for somatosensation and voluntary movements, respectively.

1.2 Connectivity of Sensorimotor Cortex

Neural activity throughout the brain is coordinated by connectivity. Trillions of connections between various types of neurons collectively form complex networks and subnetworks that give rise to function. The brain areas responsible for movement and sensation are no exception. Dense connectivity networks within and between cortical areas, subcortical structures, the cerebellum, the spinal cord, and the peripheral nervous system all contribute to an organisms' ability to efficiently interact with its environment. In order to understand how the brain accomplishes this, we must understand the rules that govern connectivity throughout it.

This dissertation is focused on how coordination is achieved between neural activity in PM, M1, and S1 columns in service of fine motor control. At least three channels of communication have the potential to coordinate activity between sensorimotor columns: thalamocortical projections (Killackey, 1973; Strick, 1975), inter-areal corticocortical projections (Muakkassa and Strick, 1979; Stepniewska et al., 2006), and intra-areal (i.e., intrinsic) connectivity (Gatter et al., 1978; Négyessy et al., 2013). Of these pathways, the latter two provide the most direct anatomical link between columns in sensorimotor cortex. Therefore, inter-areal and intra-areal corticocortical connections are the best suited to coordinate neural activity between columns in sensorimotor cortex, and are the focus of the present dissertation.

Corticocortical connections between PM, M1, and S1 have been identified in many instances (Dancause et al., 2006a,b; Davare et al., 2008; Dea et al., 2016; Dum and Strick, 2005; Gharbawie et al., 2010; Hamadjida et al., 2016; Liao et al., 2013; Muakkassa and Strick, 1979; Padberg et al., 2005; Stepniewska et al., 1993, 2006). Many of these studies have found that corticocortical connections between these areas tend to be reciprocal, pointing toward the importance of closed-loop interactions between PM, M1, and S1 in the generation of skilled movements. Connections between PM and M1 are modularly organized such that mostly non-overlapping zones of M1 are connected to PMv or PMd (Dea et al., 2016; Hamadjida et al., 2016). These connections may serve a direct bridge from motor planning to motor execution, as evidenced by the fact that PM activity selectively modu-

lates M1 outputs depending on movement type and movement phase (Davare et al., 2008; Prabhu et al., 2009). Connections between the individual cortical areas within S1 (areas 3a, 3b, 1, and 2) are dense and tied to the functional map (Friedman et al., 2020; Négyessy et al., 2013). These connections form a hierarchy of receptive field processing (Sur et al., 1985), wherein tactile and proprioceptive information from areas 3a and 3b are integrated into information about texture, size, and shape in areas 1 and 2 (Bensmaia et al., 2008; Pei et al., 2010). Finally, connections between motor and sensory areas are a direct pathway for cutaneous and proprioceptive signals from S1 to influence M1 and PM columns with dense corticospinal projections. This is perhaps best demonstrated by the ability of somatosensory feedback to enhance the performance of a brain computer interface based on M1 activity (Flesher et al., 2021). Collectively, intra-areal corticocortical connections between sensorimotor cortical areas form a complex network that contributes to the neural basis of skilled movement. Despite the extensive research detailing connections between cortical zones, the organizational relationships between these connections and somatotopy or cytoarchitecture have not been comprehensively quantified.

Intrinsic connectivity is the densest and most direct network between cortical zones (Douglas and Martin, 2004). Intrinsic connections densely connect any cortical point with the surrounding 1 mm of cortex (Capaday et al., 2009; Gatter et al., 1978; Gilbert and Wiesel, 1979; Huntley and Jones, 1991; Keller, 1993; Liao et al., 2013). In sensory zones, intrinsic connections beyond 1 mm are well-established to preferentially link functionally matching columns. For example, horizontal connections link zones with similar frequency preferences (Matsubara and Phillips, 1988). Likewise, in visual cortex, horizontal connections link columns with matched orientation tuning (Bosking et al., 1997; Gilbert and Wiesel, 1989; Livingstone and Hubel, 1984; Malach et al., 1993). Thus, patchy intrinsic connectivity is guided by functional organization in many sensory cortical zones. In somatosensory cortex, intrinsic connections are also guided by function. For example, in area 3b, intrinsic connectivity binds adjacent digit representations (Négyessy et al., 2013), but does not cross the hand-face border (Fang et al., 2002).

There are conflicting reports about intrinsic connectivity beyond 1 mm in motor cortex. Horseradish peroxidase injections into the macaque digit representation (Huntley and Jones,

1991) and the cat wrist representation (Keller, 1993) revealed patchy connections that were uniformly distributed throughout the M1 forelimb representation, but did not extend into the face representation. This pattern is consistent with sensory zones where intrinsic connectivity binds together functionally related zones. However, a more recent study suggests that intrinsic M1 connectivity is non-patchy, and binds together representations of a variety of muscles (Capaday et al., 2009). Nevertheless, these studies were quite limited in the number of sites that they studied connectivity for, and also in that they did not quantify connectivity in relation to the functional map. Consequently, the organization of intrinsic M1 connectivity is not well understood.

Collectively, previous research has demonstrated that intra- and inter-areal corticocortical connectivity spans sensorimotor cortex, and tends to bind functionally related zones. However, various limitations in these approaches (detailed below) preclude our understanding of the functional network architecture of sensorimotor cortex. Consequently, how sensorimotor cortical areas coordinate with one another to enable fine motor control remains unclear.

1.3 Connectivity Tracing Approaches

Accurate measurement of connectivity in the brain is central to understanding its function. The cortico-cortical connections of interest can be measured using a variety of techniques. Detailed below are strengths and weaknesses of connectivity tracing approaches that are relevant to the goals of the present dissertation.

1.3.1 Neuroanatomical Tracers

The gold standard of tracing anatomical connections in the brain is with neuroanatomical tracers (Lanciego and Wouterlood, 2020). In this approach, retrograde or anterograde tracers are injected into the living brain. The tracers are then allowed to transport for some amount of time, depending on the type of tracer(s) injected. After transport, the animal is sacrificed

and the brain is fixed, histologically sectioned, and then stained or reacted to reveal labeled cells or fibers. Some modern techniques, such as CLARITY (Chung and Deisseroth, 2013), do not require sectioning the brain. Finally, labeled cells and fibers in each section can be visualized under a microscope. Depending on the type of tracer used, labelled connections may be mono- or polysynaptic and anterograde or retrograde. The experimenter can therefore visualize anatomical connectivity at cellular resolution using this approach. For many applications, this approach is extremely powerful and has been used to answer a wide range of questions regarding the connectivity and function of the brain. Indeed, much of what we know already about connectivity throughout the sensorimotor system was discovered with neuroanatomical tracers.

However, anatomical tracers also have limitations, which circumscribe their usefulness for meeting the objectives of the present dissertation. One such limitation is the number of sites that can be studied in the brain of a single animal. It is difficult to distinguish more than 4-5 tracers from one another. Therefore, one can only measure the connectivity of 4-5 sites per animal, which is insufficient to identify robust relationships between connectivity and functional organization in the sensorimotor cortex. Another major limitation of anatomical tracers in the context of this work is the necessity to sacrifice the animal in order to visualize connectivity. Not being able to view connectivity in vivo may limit the interpretation of the functional relevance of connectivity. For example, the terminal nature of tracer studies precludes the measurement of connectivity before and after the reorganization of circuitry (e.g., motor learning or amputation) in a single animal.

1.3.2 Functional Magnetic Resonance Imaging

Functional magnetic resonance imaging (fMRI) infers brain function and connectivity by measuring changes associated with blood flow (Belliveau et al., 1991; Ogawa et al., 1990) which have been linked to neural activity (Kahn et al., 2011; Logothetis et al., 2001). The blood-related signal that fMRI depends upon is referred to as the blood oxygen level dependent (BOLD) signal. The chief advantages of fMRI are (1) the ability to measure functional activity throughout the entire brain, (2) at a reasonably high spatiotemporal resolution,

(3) in a noninvasive manner, (4) *in vivo*, and (5) using signals intrinsic to the brain (i.e., no extrinsic indicators required). The approach has been used to measure the structure of primate brain networks in stimulus-evoked and resting state paradigms.

In the stimulus-evoked paradigm, BOLD signal is measured in response to a stimulus, which may be peripheral (e.g., shining a light in the subject's eyes) or artificial (e.g., electrically stimulating the brain) in nature. Stimulus-evoked fMRI studies have been used with great success to identify brain regions associated with a given stimulus (e.g., Chen et al. (2013); Kim et al. (2000); Kwong et al. (1992); Ogawa et al. (1992)) or the connectivity of an electrically stimulated brain zone (e.g., Ekstrom et al. (2008); Moeller et al. (2008); Premereur et al. (2016); Tolias et al. (2005)).

In the resting state paradigm (RS-fMRI), spontaneous changes in the BOLD signal are measured and connectivity is inferred between zones with temporally correlated signals. Resting state hemodynamics are tied to underlying neural activity (Ma et al., 2016) and provide a window into the organization of brain networks (Bullmore and Sporns, 2009). RS-fMRI has been used to identify functional connectivity networks throughout the brain and to fingerprint brain pathophysiology (Beckmann and Smith, 2004; Buckner et al., 2013; Fox and Raichle, 2007; Hutchison and Everling, 2012). A large advantage of resting state paradigms in general, including RS-fMRI, is that functional connectivity (FC) can be inferred for thousands of sites throughout the brain from a single dataset. This rich connectivity information can be integrated to generate a measure of network architecture (e.g., Beckmann and Smith, 2004; Beckmann et al., 2005; Damoiseaux et al., 2006). FC measured with RS-fMRI has been compared to anatomical measures of connectivity (AC) in humans (Adachi et al., 2012; Greicius et al., 2009; Hagmann et al., 2008; van den Heuvel et al., 2009; Honey et al., 2009) and nonhuman primates (Hori et al., 2020a; Shen et al., 2012; Wang et al., 2013). These comparisons have shown generally strong, yet imperfect, correspondence between FC and AC. These comparisons have been limited by the discrepancy in spatial resolution between AC and RS-fMRI FC.

Although fMRI is a powerful tool with many advantages for interrogating the functional network architecture of the brain, the approach also carries some limitations that make it impractical for accomplishing the objective of this dissertation. The chief limitation is the

spatial resolution offered by fMRI. In primate studies that use stimulus-evoked fMRI, a $\sim$1 mm voxel size is common (e.g., Premereur et al. (2018)), which is insufficient for answering the questions in this dissertation. The spatial resolution achieved in RS-fMRI is typically even lower (e.g., 1.5 x 1.5 x 2 mm in Thomas et al. (2021)). However, higher resolutions may be achieved in stimulation-evoked fMRI with appropriate paradigms (Chen et al., 2013; Kim et al., 2000), or in RS-fMRI when stronger magnets are used (Huber et al., 2017; Shi et al., 2017). Nonetheless, the spatial resolution achieved in the vast majority of primate fMRI studies would be insufficient for measuring the network architecture of sensorimotor cortex, where somatotopy exists at the columnar scale ($< \sim$250 μm). Another limitation of fMRI in this context is the unclear relationship between FC measured with fMRI and AC, discussed in the previous paragraph. Furthermore, in intracortical microstimulation-evoked fMRI studies, current amplitudes must be quite large to drive a response detectable by fMRI (Matsui et al., 2011; Premereur et al., 2016; Tolias et al., 2005). These large current amplitudes cause significant passive current spread (Stoney et al., 1968), which limits the ability to distinguish between responsive and unresponsive zones close to the stimulation site.

1.3.3 Intrinsic Signal Optical Imaging

Intrinsic signal optical imaging (ISOI) is an optical imaging approach that measures hemodynamic signals in vivo (Grinvald et al., 2000), and is therefore operationally similar to fMRI. As such, many of the advantages of fMRI also apply to ISOI. However, ISOI measures hemodynamic signals optically, rather than magnetically as in fMRI. Therefore, brain regions not visible from the surface (e.g., subcortical structures or sulci) are inaccessible to ISOI. Despite this limitation, a strength of this method, particularly in the context of the objectives of this dissertation, is that ISOI can measure cortical hemodynamic signals at high spatial resolution. This advantage alone makes ISOI an attractive candidate to investigate connectivity in sensorimotor cortex. Like fMRI, ISOI can be used in stimulus-evoked or resting state paradigms, although the resting state approach is not currently well-developed in primates.

Stimulus-evoked ISOI has been used with peripheral stimuli to measure functional maps in sensory regions at a columnar resolution (Bonhoeffer and Grinvald, 1991; Lu and Roe, 2007; Sheth et al., 2004). Functional maps in visual cortex measured with ISOI correspond with long-established functional organization (Lu and Roe, 2007). Additionally, ICMS+ISOI has been used to measure effective connectivity of single cortical columns in primates, in vivo (Brock et al., 2013; Friedman et al., 2020; Stepniewska et al., 2011). Effective connectivity measured in these studies was consistent with known anatomical connections. ICMS+ISOI is an attractive approach for mapping the FC of motor columns for several reasons: (1) the approach identifies causal relationships, (2) at a large number (dozens) of cortical sites, (3) which are consistent with known anatomical connections, (4) at a columnar resolution, (5) in vivo, (6) and without the need for extrinsic agents. (7) Finally, ICMS+ISOI does not rely on peripheral stimulation, which is not an option in motor areas.

Resting state ISOI is an emerging approach that shows promise for tracing connectivity in rodents (Bauer et al., 2018; Kura et al., 2018; Vazquez et al., 2014; White et al., 2011) and ferrets (Vasireddi et al., 2016), but has yet to be used in primates. Given the operational similarities between ISOI and fMRI, RS-ISOI is likely to reveal functional connectivity in primates. Furthermore, demonstrations of high spatial resolution in the aforementioned studies and in stimulus-evoked ISOI studies indicate the potential for RS-ISOI to achieve columnar resolution. As such, RS-ISOI is an attractive candidate to investigate sensorimotor network architecture, especially in large FOVs where the dozens of sites offered by ICMS+ISOI would be insufficient for identifying connectivity rules. However, given the limited previous uses of RS-ISOI, the method would require development and benchmarking in primates.

In summary, stimulus-evoked and resting state ISOI are both attractive candidates for interrogating the network architecture of primate sensorimotor cortex. The chief drawback of ISOI is that it cannot measure connectivity in subcortical structures, but that limitation is irrelevant here because those brain regions are outside the scope of this dissertation. An additional limitation of ISOI is that it requires a craniotomy in animals with thicker skulls, such as primates, and is therefore considerably more invasive than fMRI. However, invasive procedures of this nature are relatively normal in non-human primate research.

1.3.4 Extrinsic Agent Approaches

One additional category of connectivity tracing approaches is those that require extrinsic indicators, such as voltage sensitive dyes (VSD), genetically encoded calcium indicators (GCaMP), or optogenetic approaches. When compared to fMRI and ISOI, these indicators provide better fidelity to neural activity, higher temporal resolution, and, in some cases, a higher spatial resolution (Arieli et al., 1995; Chan et al., 2015; Lim et al., 2013; Mohajerani et al., 2013)). Despite the success of these types of approaches in some animal models, they are difficult to successfully implement in large brains (e.g., monkeys). Given the primate-focused objectives of the present dissertation, this limitation is quite significant.

1.4 Toward the Functional Network Architecture of Sensorimotor Cortex

The rules that govern the organization of connectivity throughout sensorimotor cortex remain unclear. As such, the neural basis of fine motor control is not well understood. The overall objective of this dissertation is to interrogate the functional network architecture of sensorimotor cortex by identifying relationships between connectivity, somatotopy, and cytoarchitecture. As technology has progressed, I am presented with a unique opportunity to accomplish this objective using ISOI-based approaches to measure high resolution connectivity at many sites in the primate brain *in vivo*. This connectivity can be quantified in the context of functional maps to identify organizational features. I will employ this approach in the squirrel monkey sensorimotor cortex, where a lack of major sulci means that the majority of the cortical areas of interest are accessible on the surface of the brain for measurement of somatotopy and connectivity.

In the following chapters, I will develop, benchmark, and utilize ISOI-based connectivity tracing approaches in squirrel monkey sensorimotor cortex. chapter 2, I use microelectrode mapping and ICMS+ISOI to measure somatotopy and connectivity in order to identify the principles of intrinsic M1 connectivity. chapter 3, I develop a RS-ISOI connectivity mapping approach and benchmark it against ICMS+ISOI and neuroanatomical tracers. In chapter 4, I

utilize RS-ISOI to measure connectivity at thousands of sites throughout sensorimotor cortex, which reveals organizational features of sensorimotor network architecture. Collectively, these chapters aim to develop and benchmark novel connectivity tracing approaches, and then utilize them to interrogate the neural basis of fine motor control.

2.0 Principles of Intrinsic Motor Cortex Connectivity in Primates

Text and figures from this chapter are from Card and Gharbawie (2020), reformatted for this dissertation.

2.1 Summary

The forelimb representation in motor cortex (M1) is an important model system in contemporary neuroscience. Efforts to understand the organization of the M1 forelimb representation in monkeys have focused on inputs and outputs. In contrast, intrinsic M1 connections remain mostly unexplored, which is surprising given that intra-areal connections universally outnumber extrinsic connections. To address this knowledge gap, we first mapped the M1 forelimb representation with intracortical microstimulation (ICMS) in male squirrel monkeys. Next, we determined the connectivity of individual M1 sites with ICMS + intrinsic signal optical imaging (ISOI). Every stimulation site activated a distinctive pattern of patches (∼0.25 to 1.0 mm radius) that we quantified in relation to the motor map. Arm sites activated patches that were mostly in arm zones. Hand sites followed the same principle, but to a lesser extent. The results collectively indicate that preferential connectivity between functionally matched patches is a prominent organizational principle in M1. Connectivity patterns for a given site were conserved across a range of current amplitudes, train durations, pulse frequencies, and microelectrode depths. In addition, we found close correspondence in somatosensory cortex between connectivity that we revealed with ICMS+ISOI and connections known from tracers. ICMS+ISOI is therefore an effective tool for mapping cortical connectivity and is particularly advantageous for sampling large numbers of sites. This feature was instrumental in revealing the spatial specificity of intrinsic M1 connections, which appear to be woven into the somatotopic organization of the forelimb representation. Such a framework invokes the modular organization well-established for sensory cortical areas.

2.2 Significance

Intrinsic connections are fundamental to the operations of any cortical area. Surprisingly little is known about the organization of intrinsic connections in motor cortex (M1). We addressed this knowledge gap using intracortical microstimulation (ICMS) concurrently with intrinsic signal optical imaging (ISOI). Quantifying the activation patterns from dozens of M1 sites allowed us to uncover a fundamental principle of M1 organization: M1 patches are preferentially connected with functionally matched patches. Relationship between intrinsic connections and neurophysiological map is well-established for sensory cortical areas, but our study is the first to extend this framework to M1. Microstimulation + imaging opened a unique possibility for investigating the connectivity of dozens of tightly spaced M1 sites, which was the linchpin for uncovering organizational principles.

2.3 Introduction

Primary motor cortex (M1) is central to arm and hand control in primates. The forelimb representation in monkeys is a widely-used model for studying cortical control of movement, neural basis of learning, population coding, and more. To understand the organization of M1 networks, neuroanatomical and neurophysiological investigations have focused on the outputs and inputs of the M1 forelimb representation (e.g. Dum and Strick, 2005; He et al., 1995; Park et al., 2001; Stepniewska et al., 1993). Such efforts have been instrumental in shaping our understanding of how the M1 forelimb representation is connected with the rest of the brain and with the spinal cord. In contrast, far less is known about the organization of the intrinsic connections of the M1 forelimb representation. Mapping these connections and the networks that they establish would provide a useful organizational framework for interrogating the computations that occur within M1 in the service of arm and hand control.

Only a few studies have examined the organization of the intrinsic networks of the M1 forelimb representation (Capaday et al., 1998, 2009; Huntley and Jones, 1991; Keller, 1993). Huntley and Jones (1991) showed in macaque monkeys that patchy horizontal connections

link the M1 digit zone with other hand and arm zones. A similar connectivity pattern was reported in cats for the M1 wrist zone (Keller, 1993). Both studies therefore provided evidence that M1 horizontal connections are spatially selective (i.e. patchy) and at the same time distributed throughout the forelimb representation. However, neither study quantified the traced connections, which complicates our understanding of the relationship between intrinsic M1 connections and somatotopy of the forelimb representation. Even if the results were quantified, the findings would have mostly shed light on the connectivity of hand zones only (i.e. digit and wrist) given that connections of the M1 forelimb representation are likely zone specific (Dea et al., 2016; Hamadjida et al., 2016). The density of intrinsic connections in sensory cortical areas and their role in functional binding (Douglas and Martin, 2004) leave little doubt that our limited understanding of intrinsic M1 connectivity represents a critical knowledge gap about M1 functional architecture.

The present study was motivated by a need for understanding the principles that govern the organization of intrinsic M1 networks. Our main objectives were to (1) determine connectivity for sites throughout the M1 forelimb representation, and (2) quantify the relationship between connectivity and somatotopy of the M1 forelimb representation. To accomplish these objectives, we adopted an imaging-based approach in squirrel monkeys that allowed us to investigate M1 connectivity *in vivo* (Brock et al., 2013; Stepniewska et al., 2011). First, we mapped the M1 forelimb motor representation using intracortical microstimulation (ICMS). Next, we stimulated M1 sites individually and measured the evoked cortical response using intrinsic signal optical imaging (ISOI). Finally, we quantified the activation maps in relation to somatotopy of the M1 forelimb representation as a measure of intrinsic M1 connectivity. Our observations from dozens of stimulation sites showed that intrinsic M1 connectivity is mostly patchy and the patches are spatially organized with respect to the forelimb motor map.

2.4 Methods

2.4.1 Animals

Experiments were performed on 4 adult male squirrel monkeys (*Saimiri sciureus*). Animals were four to eight years old and weighed between 800 and 1200 g. All procedures were approved by the University of Pittsburgh Institutional Animal Care and Use Committee and followed the guidelines of the National Institutes of Health guide for the care and use of laboratory animals.

2.4.2 Surgical Procedures

One cranial opening per studied hemisphere provided access to frontal and parietal cortex. Each cranial opening was accessed multiple times under sterile conditions (Table 2.1). Thirty minutes prior to sedation, animals were treated with an antiemetic (Zofran, 0.3 mg/kg, IM) and Atropine (0.03 mg/kg, IM) to reduce secretions. Ketamine induction (10-15 mg/kg, IM) was followed with isoflurane (0.5-2.5%) in O2 (2-3 L/min). Once sedated, Dexamethasone (1 mg/kg, IM), Ketofen (2 mg/kg, IM) and Gentamicin (2 mg/kg, IM) were administered to prevent brain swelling, pain, and infection, respectively. Animals were intubated, artificially ventilated, wrapped in a heating blanket, and secured in a stereotaxic frame. Heart rate, arterial oxygen saturation, expired CO_2, blood glucose, and body temperature were monitored continuously and adjustments to anesthesia, ventilation, and heat were made accordingly. Fluids (5% dextrose in Lactated Ringer's solution, 2-3 ml/kg/hr, IV) were provided for the duration of each procedure.

An incision was performed for each procedure. All steps from this point onwards were conducted with the aid of a surgical microscope. For the first procedure within a hemisphere, a dental drill was used to open a rectangular window for access to the forelimb representations in motor cortex and in somatosensory cortex. After a durotomy, cortical pulsations were stabilized with 3% agarose (Invitrogen, Carlsbad, CA) solution in physiological saline. Data acquisition proceeded from this point and lasted for several hours. During data acquisition, anesthesia was maintained with ketamine infusion (3-6 mg/kg/hr, IV) and isoflurane (0.25

- 1.0%) mixed in 50% $N_2 2O_2$ and 50% O_2 (2-3 L/min). At all other times, anesthesia was maintained with isoflurane (0.5-2.5%) mixed in O_2 (2-3 L/min). The agar was removed at the conclusion of data acquisition and an artificial dura (Tecoflex; Sakas et al., 1990) was secured into the cranial opening to protect the cortex. The craniotomy was sealed with dental cement and the scalp was sutured closed. The animal was recovered from anesthesia and another dose of the pre-procedure drugs was administered in addition to Vitamin B12 (0.5 mg/kg, IM). Analgesics and corticosteroids were administered every 12 h for the following 72 h. Each procedure lasted ∼14 hours from sedation to recovery and the single terminal experiment lasted 43 h.

Table 2.1: Procedures and data collected from each animal[a]

Monkey	Hemisphere	Procedures	Imaging Runs	Effective Connectivity Sites	Motor Map Sites	Receptive Field Sites
M	Left	14	58	49	223	87
D	Left	4	11	11	108	1
	Right	3	15	1	23	17
R	Left	6	20	18	131	-
G	Left	2	2	2	-	35
Total		29	106	81	485	140

a. Numbers for each animal are limited to the data included in the present study.

2.4.3 Motor Mapping

The objective was to map the forelimb representation in M1 with ICMS. A hydraulic microdrive (Narishige MO-10) connected to a Kopf micromanipulator was used for positioning

a platinum/iridium microelectrode (125 μm shaft, 260 kΩ median impedance, MicroProbes). Electrode impedance was periodically tested in each motor mapping session and a new microelectrode was used if impedance approached 1 MΩ.

Each penetration targeted the approximate depth of layer V (1800 μm below cortical surface). Microstimulation trains (18 cathodal pulses, 0.2 ms pulse width, 300 Hz pulse frequency, 1 Hz train frequency) were delivered with an 8-Channel Stimulator (model 3800, AM Systems). Current amplitude was adjusted with a stimulus isolation unit (model BSI-2A, BAK Electronics) until a movement was evoked and up to a maximum of 150 μA. The threshold recorded for each site was the minimum current amplitude that evoked movement on $\sim$50% of microstimulation trains. Responses to ICMS were generally suppressed with heart rate $<$250 beats per minute. The combination of ketamine infusion and isoflurane was central to achieving a state in which ICMS could evoke movements under anesthesia.

ICMS facilitates and suppresses activity in groups of muscles that lead to observable movements around one or more joints. Two to three experimenters evaluated the evoked responses; only one experimenter was not blind to the microelectrode location. Each ICMS site was classified according to joint (digit, wrist, elbow, shoulder) and movement evoked (e.g. flexion, extension, abduction, etc.) that showed the most robust effect at the lowest current amplitude. Although shoulder responses were readily detected, the type of shoulder movement was often complicated due to positioning within the stereotaxic apparatus. Forearm responses (i.e., pronation and supination) were included with elbow.

The forelimb representation was mapped over the course of several experiments (30-60 ICMS sites/experiment). Distance between ICMS sites was typically $\leq$1 mm (Figure 2.1A). Each site was recorded on a printed, high-resolution photo of cortex. Some sites were tested in multiple procedures to confirm stability over weeks/months. Color coded maps were generated in MATLAB using a Voronoi diagram (*voronoi* function) constrained to a 1.0 mm radius around each site. Medial and lateral borders were drawn to separate the forelimb representation from the trunk and face representations. The rostral M1 border was estimated from threshold to evoke movements ($\geq$80 μA) and distance from central sulcus (Figure 2.1B). The caudal M1 border was estimated from thresholds to evoke movements and from the location of area 3a, which was mapped as described in the following section.

Animals in the present study had a well-defined forelimb representation. In addition, the relative location of the arm zone (i.e., shoulder sites and elbow sites) and the hand zone (i.e., digit sites and wrist sites) was consistent across animals.

2.4.4 Somatosensory Mapping

The objective was to map the forelimb representation in somatosensory cortex with multiunit recordings. For each mapping site, a tungsten microelectrode (125 μm shaft, 500 kΩ median impedance) was lowered to the approximate depth of layer IV (700-800 μm below cortical surface). Multiunit activity was amplified (10,000x) and filtered (bandpass 300-5000 Hz) using an AC Amplifier (Model 2800, AM Systems). The signal was passed through a 50/60 Hz noise eliminator (HumBug, Quest Scientific Instruments Inc.) then visualized on an oscilloscope and broadcasted over a loud speaker. The receptive field for each microelectrode site was determined from modulations in neural activity in response to systematic stimulation of the contralateral forelimb. Receptive fields were classified according to location on the arm or the hand and whether responses were cutaneous (skin contact) or proprioceptive (joint manipulation). Some sites were remapped in multiple procedures to confirm receptive field stability. Somatosensory maps were generated using the same Voronoi function that was used for the motor map.

Cortical borders were estimated from transitions in receptive field properties along the rostro-caudal dimension. Units in areas 3b and 1 responded robustly to cutaneous stimulation and had relatively small receptive fields (e.g. single digit phalanx). In contrast, units in area 3a responded weakly to the manipulation of multiple joints (e.g. entire digit or multiple digits). Area 2 contained a mixture of units that responded to joint manipulation or cutaneous stimulation. The border between areas 3b and 1 was estimated from the representations of the pads of the palm that exist in caudal aspects of area 3b and rostral aspects of area 1 (Sur et al., 1982).

2.4.5 Intrinsic Signal Optical Imaging

We used intrinsic signal optical imaging (ISOI) to measure the ICMS evoked cortical response. Images of cortex were acquired with a 12-bit CCD camera (Photon Focus) connected to an optical imaging system (Imager 3001, Optical Imaging Ltd). Camera frames (250 Hz) were temporally binned to 5 Hz except in initial experiments when temporal binning was purposely set to 20 Hz. Frames were not spatially binned. We chose a tandem lens combination such that the field-of-view (768 x 768 pixels) would include ∼10 x 10 mm of cortex (∼13 μm/pixel). This field-of-view captured the entire M1 forelimb representation and surrounding cortex at high spatial resolution. A counter-weighted swivel arm was maneuvered to position the camera directly above cortex. Fine angle adjustments were achieved with a 3-axis geared head (410 Junior Geared Tripod Head, Manfrotto). Camera position (x, y, and z directions) was translated with independent linear stages. Illumination (620 nm) for ISOI was provided from 3 independently controlled LEDs. Image acquisition was periodically paused to ensure uniform illumination. For spatial reference, blood vessel patterns were imaged (540 nm illumination) at the start of each imaging run.

2.4.6 Measuring the Stimulation Evoked Response

To evoke a cortical response from any point in cortex, a microelectrode (platinum/iridium, 125 μm shaft) was lowered to 1000 μm below cortical surface. Electrode impedance was comparable at the start (median = 260 kΩ) and end of each experiment (median = 320 kΩ). ICMS and concurrent ISOI were conducted in an event-based design. A given ICMS site was tested on at least 50 blocks. Every block included at least one ICMS condition and one blank condition (i.e., no ICMS). Every condition was presented only once per block (i.e., one trial/condition). Unless otherwise stated, image acquisition lasted for 4 s/trial with a 12 s intertrial interval. In ICMS trials, baseline cortical activity was imaged for two data frames (i.e., 400 ms in 5 Hz binning; 100 ms in 20 Hz binning) before stimulation onset. The start of a trial in any condition was synchronized with the ventilation phase to reduce respiration artifact. The ICMS set up was identical to the one used for motor mapping, except here we used a voltage-controlled stimulus isolation unit (Model 3820, AM Systems). Unless other-

wise stated, the stimulation train in a single ICMS trial consisted of 150 biphasic pulses, 0.2 ms phase width, 300 Hz pulse frequency, and 60 μA current amplitude. We set the number of pulses and the pulse frequency based on previous work that showed the effectiveness of long-train, high frequency stimulation, in evoking movements that recapitulate ethologically relevant behavior (Graziano et al., 2002; Stepniewska et al., 2005; Baldwin et al., 2017). Although evoking movements was not our objective for ICMS+ISOI, we reasoned that the same stimulation parameters would effectively drive intrinsic M1 networks.

2.4.7 Experiments on ICMS Parameters

The effects of ICMS parameters on activation maps were tested in a separate set of experiments. A range of microelectrode depths (200, 400, 1000, 1400, and 1800 μm from cortical surface), current amplitudes (20, 40, 60 μA), train durations (18, 36, 75, and 150 pulses), and pulse frequencies (37, 75, 150, and 300 Hz), were tested. Other parameters were consistent with the previous section.

2.4.8 Image Analysis

2.4.8.1 Optical Maps ISOI data was analyzed using custom MATLAB scripts. Two image subtractions were carried out as a pre-processing step to minimize global signals (e.g. cortical pulsations, blood vessels, illumination noise). (1) First-frame subtraction. In every trial, the first data frame was subtracted from subsequent frames. (2) Blank subtraction. For each block of trials, the frames of the blank condition were subtracted from the frames of the ICMS condition. After this pre-processing step, the average frame was calculated from consecutive frames that spanned 400-600 ms of image acquisition. Frame selection was optimized to coincide with peak reflectance change near the tip of the stimulating micro-electrode, which typically occurred 1500-2000 ms from stimulation onset. Finally, the mean frames calculated from the trials of a given condition were averaged together to generate maps for each ICMS condition minus blank condition.

Subtraction maps were then processed to aid visualization. Maps were convolved with a high-pass median filter (kernel = 150-250 pixels) to correct uneven illumination and residual

motion artifact. Maps were also convolved with a low-pass Gaussian filter (kernel = 10 pixels) for smoothing. To enhance contrast, the distribution of pixel values within a map was clipped to ±1.5 standard deviations from the median pixel value. In the final subtraction maps, dark pixels indicate decreased reflectance of red light, which is attributed to the hemodynamic response that ensues as a result of local increases in neural activity. Dark pixels therefore report cortical locations where ICMS evoked a response.

2.4.8.2 Activation Maps Activation maps were generated to objectively determine which pixels darkened in response to stimulation. Individual trials from the ICMS condition and the blank condition were first-frame subtracted and then spatially convolved using the same approach described for the optical maps. However, in the present analysis, mean data frames were calculated separately for ICMS and blank conditions. Mean frames from the ICMS condition were then compared on a pixel-by-pixel basis to the mean frames from the blank condition. Pixels were considered active in response to stimulation if they were significantly darker (t test, $p < 0.001$) in the ICMS condition as compared with the blank condition.

2.4.8.3 Intrinsic Signal Time Course Time courses were measured from several regions of interest (ROIs; circle, ∼15-pixel radius, ∼0.13 mm^2). Pixel values within an ROI were averaged to a single value for each data frame. Values from successive data frames constituted the time course of a trial. Time courses from dozens of trials (same condition) were averaged to obtain the time course for a given ROI.

2.4.8.4 Activation Map Quantification The activation map from each M1 stimulation site was quantified in relation to the motor map. First, the activation map was co-registered with the motor map. Next, the activation map was quantified by assigning every pixel to the spatially coincident zone within the motor map (i.e. arm zone, hand zone, etc). The number of pixels in each zone was then converted to surface area (mm^2). Finally, the spatial range of the activation map was quantified according to the Euclidean distance (mm) between the stimulation site and every pixel activated in response to stimulation.

2.4.8.5 Stimulation Site Identity Blood vessels were used as landmarks to guide placement of the stimulating microelectrode into target sites within the motor map. Stimulation site identity was also confirmed from the activation map. Specifically, the stimulation site was presumed to be in the center of the cluster of pixels that was first to darken; typically after 200 ms from stimulation onset. In most cases, the pertinent cluster of pixels was within 100 μm of the stimulation site location noted during the experiment. The stimulation site was then classified (i.e. arm site, hand site, etc.) according to the motor map zone that contained the cluster of dark pixels (e.g. shoulder site, digit site, etc.). In mixed forelimb sites the cluster of dark pixels overlapped with arm and hand zones.

2.4.8.6 Activation Map Alignment Activation maps from the same hemisphere were aligned to a common reference frame. Alignment was performed by estimating a projective transformation from points that were present in the blood vessel patterns of the ICMS condition, blank condition, and the common reference frame (*estimateGeometricTransform* function in MATLAB). The projective transformation produced a transform matrix that included scaling, rotation, and offset necessary to align each data frame to the common reference frame.

2.4.9 Statistical Analyses

All statistical tests were performed using SPSS or MATLAB. In all instances, parametric tests were used if pertinent assumptions (e.g., normality and homoscedasticity) were not violated. Normality was tested using the Kolmogorov-Smirnov test and homoscedasticity was tested using Levene's test. Non-parametric tests were used if assumptions of parametric tests were not satisfied. For comparisons between two populations, either a 2-sample t test or a Wilcoxon rank sum test was performed. For comparisons across more than two populations a one-way ANOVA was used with a *post hoc* Tukey HSD test. For all tests, a significance level of $\alpha = 0.05$ was used. In all figures, levels of significance are reported as follows: $*p < 0.05$, $**p < 0.01$, $***p < 0.001$.

2.5 Results

We investigated the intrinsic connectivity of the forelimb representation in M1. In three squirrel monkeys, we first mapped the organization of the M1 forelimb representation using ICMS (Figure 2.1A-F). Next, we measured connectivity for 64 sites within the M1 forelimb representation (Figure 2.1D-F red dots; Table 2.1). At every site, the ICMS evoked cortical response was recorded with ISOI (Figure 2.1G). Co-registering the imaging results with the motor maps revealed two consistent features that likely reflect organizational principles of intrinsic M1 connectivity. First, every stimulation site activated several patches within the M1 forelimb representation. Second, patches mostly coincided with forelimb zones of the same functional classification as the stimulation site.

2.5.1 Consistent Organization of the M1 Forelimb Representation

The M1 forelimb representation was organized consistently in the three squirrel monkeys. Digit and wrist zones were near the center of the M1 forelimb representation and were surrounded by elbow and shoulder zones (Figure 2.1A). This topography was particularly apparent once shoulder and elbow zones were classified as arm and digit and wrist zones were classified as hand (Figure 2.1C-F). A similar horseshoe/nested organization has been reported for the M1 forelimb representation in macaques (Kwan et al., 1978; Park et al., 2001; Sessle and Wiesendanger, 1982) and to some extent in New World squirrel monkeys (Dancause et al., 2008). However, a more fractured organization is perhaps more widely recognized for New World monkeys (Donoghue et al., 1992; Gould et al., 1986; Nudo and Milliken, 1996; Strick and Preston, 1982). Current thresholds for evoking forelimb movements (median = 19 μA) were in the range expected for motor mapping under anesthesia (Nudo and Milliken, 1996). Current thresholds were slightly lower for hand sites (median = 15.5 μA) as compared to arm sites (median = 21.0 μA). Rostral and caudal M1 borders were drawn near sites with current thresholds >80 μA (Figure 2.1B).

Motor maps were build up in each animal over several experiments (30-60 ICMS sites per experiment). To assess the stability of ICMS-evoked movements over time, we retested

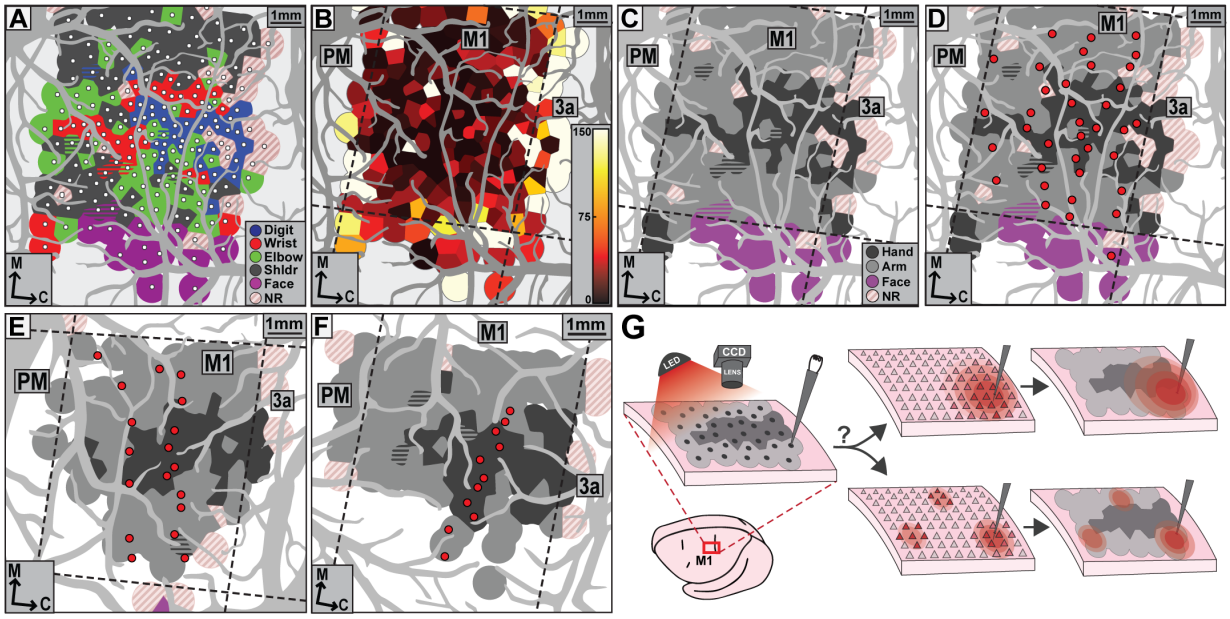

Figure 2.1: Mapping M1 connectivity with microstimulation and imaging. (A) Map of the M1 forelimb representation in the left hemisphere (monkey M). Major blood vessels are masked in gray. White dots depict microelectrode sites ($n = 223$) for ICMS. Motor map was completed over the course of multiple experiments (30-60 ICMS sites/experiment). Voronoi tiles (1.0 mm radius) are color-coded according to the ICMS-evoked movement. Striped tiles (1 color/joint) represent dual movements. Non-responsive sites "NR" failed to evoke movements with current amplitudes up to 150 μA. (B) Same motor map in (A), but color-coded according to current amplitude (μA) for evoking movements. Rostral and caudal M1 borders (dotted lines) are drawn at the transition from low ($\sim$80 μA) to high ($\sim$80 μA) current thresholds. (C) Same motor map as in (A), but wrist and digit sites are classified as hand (dark gray); shoulder and elbow sites are classified as arm (light gray). (D) Connectivity mapping sites (red dots) superimposed on motor map. (E-F) Maps of the M1 forelimb representations from monkey R (131 sites) and monkey D (108 sites), respectively. Red dots are connectivity mapping sites. (G) Schematic for mapping the connectivity of an M1 site using ICMS + ISOI. Bifurcated arrow points to two potential activation patterns. Top, activation (red shading) is most intense near the stimulation site and declines with distance. Bottom, activation is in multiple patches. Right most column, activation maps co-registered with the motor map for quantification.

a subset of forelimb sites months after initial motor mapping (n = 56 sites, 220 ± 152 d apart, mean ± 1 SD). The present analysis only includes sites in which the microelectrode location during retesting was within 250 μm of the original site. In five squirrel monkeys (three cases in Figure 2.1; two cases from a separate study), we found that 47/56 (∼84%) of the retested sites had the same classification at both time points. Results from this sample of retested sites suggests that motor maps were relatively stable over time.

2.5.2 ICMS Activates Patches in the M1 Forelimb Representation

To investigate connectivity, ICMS trains (150 biphasic pulses, 0.2 ms pulse width, 300 Hz, 60 μA) were delivered 1000 μm below the cortical surface. The evoked cortical response was measured with ISOI. The average response for each site was determined from 50 ICMS trials. The rationale here is that ICMS would modulate intrinsic signal levels in M1 zones that are connected to the stimulation site (Figure 2.1G). Indeed, ICMS onset immediately drove a decrease in reflectance (pixel darkening) in well-defined zones (0.25 to 1.0 mm radius) that we refer to as patches. Quantifying the patches from dozens of sites in the M1 forelimb representation (Figure 2.1D-F) was the linchpin for uncovering the principles that govern intrinsic M1 connectivity.

Figure 2.2 shows intrinsic signal time courses from a representative site. The earliest decrease in reflectance change occurred at the stimulation site (Figure 2.2A, upward arrowhead). This patch was evident within 400 ms of ICMS onset and it expanded over time to peak in size (∼1 mm radius) by 1400 ms from ICMS onset. Beyond this main patch, at least four smaller patches were evident within the M1 forelimb representation (Figure 2.2A, downward arrowheads). Activation in distant patches lagged the main patch (Figure 2.2A, 250 ms and 750 ms, respectively). We interpret main and distant patches as zones with connectivity, most likely horizontal connections, to the stimulation site. For each stimulation site, we consider the patches and the connections that link them as an intrinsic network within the M1 forelimb representation.

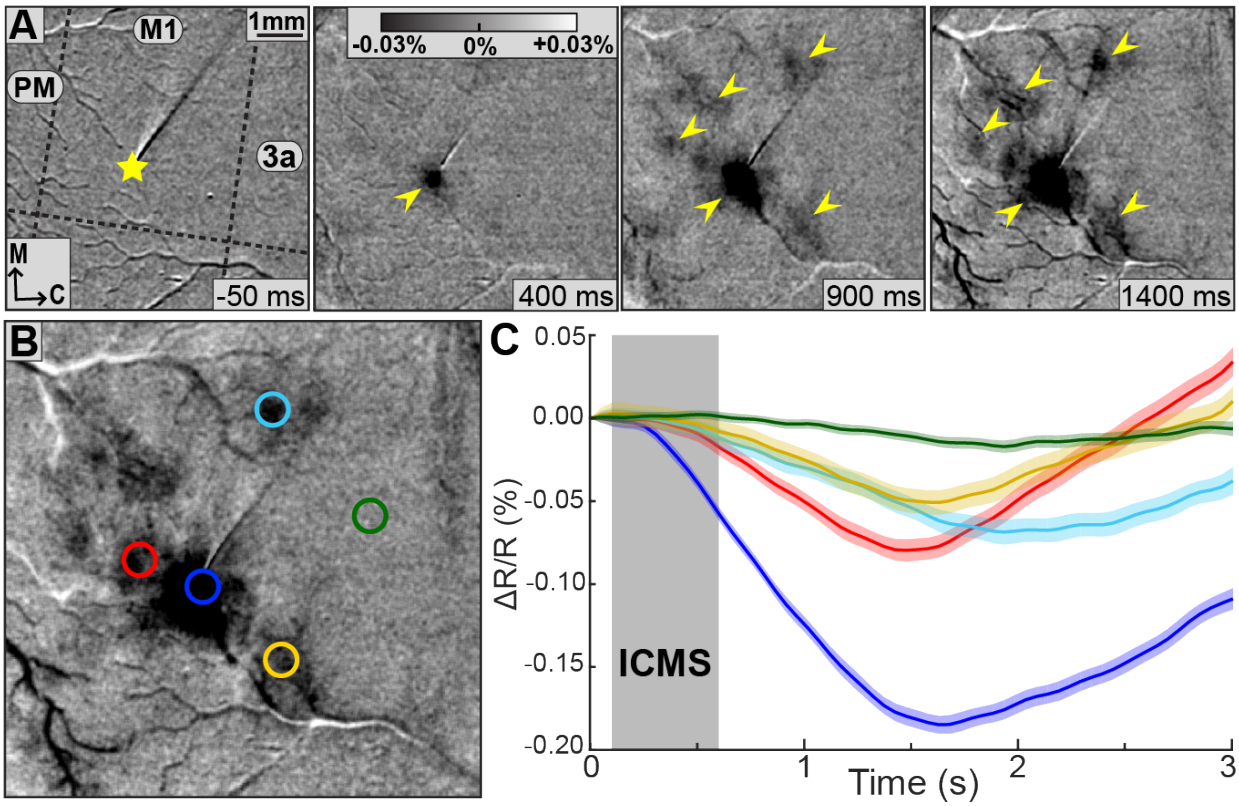

Figure 2.2: ICMS activates patches in the M1 forelimb representation. (A) Optical images: ICMS condition minus Blank condition (50 trials/condition). Each panel is an average optical image after first-frame subtraction, spatial filtering, and clipping (median ± 1.5 SD). Time (ms) in relation to ICMS onset is in the bottom right-hand corner of each frame. ICMS train (500 ms duration) started after two frames (100 ms) of baseline imaging. Yellow star marks the stimulation site, but the tip of the microelectrode was 1000 μm below the cortical surface. The main activation patch (upward arrowhead) had the earliest onset. More distant patches (downward arrowheads) lagged the development of the main patch. Scale bar and reflectance intensity scale apply to all optical images. (B) Average optical image generated from the 10 frames acquired 1050-1550 ms from ICMS onset. Colored circles are ROIs for time course analysis. (C) Line plot shows time course of reflectance change (mean ± SEM). Line colors correspond to ROI colors in (B).

2.5.3 Intrinsic Signal Time Course

To quantify the time course of the evoked cortical response, reflectance change was measured in 5 ROIs (Figure 2.2B, colored circles). In the four ROIs that overlapped patches, reflectance started to decrease within 200-400 ms of ICMS onset. The earliest and most intense reflectance decrease was in the center of the main patch (Figure 2.2B, dark blue). Reflectance change in this ROI peaked ∼1500 ms after ICMS onset (Figure 2.2C, dark blue). At the periphery of the main patch (Figure 2.2B-C, red), reflectance change was ∼50% less intense than in the center of the main patch (∼1 mm away). In distant patches (Figure 2.2B-C, cyan & yellow), reflectance change was slightly less intense than in the periphery of the main patch. Lack of modulation in the control ROI (Figure 2.2B-C, green) supports the spatial specificity of the ICMS evoked cortical response. The present time courses were consistent across dozens of M1 sites and in somatosensory cortex. Time courses for the main patch were also consistent with previous studies using ICMS+ISOI in posterior parietal cortex and in somatosensory cortex (Brock et al., 2013; Stepniewska et al., 2011).

In addition to informing us on M1 connectivity, we investigated intrinsic signal time courses in order to set timing parameters. In 1 experiment, image acquisition was purposely extended to 20 s/trial to ensure the capture of the late phases of intrinsic signal modulation. In addition, alternate trials were imaged with red (625 nm) or with green illumination (528 nm) to ensure that intrinsic signal modulations related to oximetry and to blood volume were both taken into consideration. Observations from this experiment motivated us to set image acquisition to 4 s and to include a least 1 s of data after the largest/slowest signals peaked (Figure 2.3). We set the intertrial interval to 12 s, which is when the same signals approached baseline.

2.5.4 Activation Maps are Stable Over Months

In several stimulation sites, we investigated whether activation maps were reproducible over months. One of those stimulation sites was in the arm zone near the face representation (Figure 2.4). In the average optical map (ICMS minus blank), the main patch (Figure 2.4A, upward arrowhead) was approximately centered on the stimulation site (Figure 2.4A,

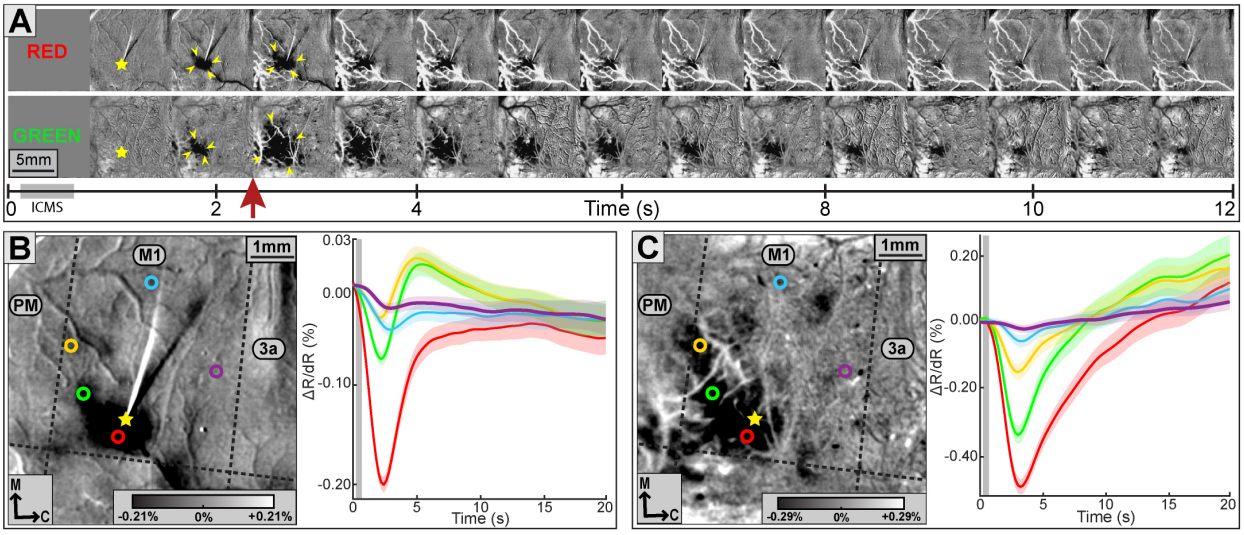

Figure 2.3: Time course of intrinsic signal modulation evoked from ICMS. (A) Optical images: ICMS condition minus Blank condition. Red illumination (620 nm) images and green illumination (540 nm) images were acquired within minutes of each other for direct comparison. Each optical image is an average (50 trials) after first-frame subtraction and spatial filtering. Trial timeline shows the ICMS train (500 ms) in relation to image acquisition. Images were captured every 200 ms for 20 seconds, but are shown here every 800 ms and for the first 12 seconds only. Yellow star depicts stimulation site. Yellow arrowheads approximately outline the main activation patch (dark pixels). In frame 3 (1800 ms from ICMS onset), the main patch is comparable in size under red illumination (top) and green illumination (bottom). In frame 4, marginal increase is observed in the size of the patch under red illumination, but the same patch is considerably larger under green illumination. Red arrow on timeline marks the time point for the optical images shown in (B) and (C). (B) Colored circles are regions-of-interest (ROIs) for the time courses in the adjacent panel. Line plot (mean + SEM) color matches ROI color. (C) Optical image and time course plots for green illumination ISOI. Note, different y-axes in (B) and (C). Line plots in (B) and (C) show that reflectance change (pixel darkening) peaked within 4 seconds of stimulation onset. The slowest return to baseline corresponded to the most intense reflectance change, which was in the main patch located at the stimulation site. In that ROI (red circle), reflectance returned to baseline levels within ∼10 seconds (red illumination) or within ∼13 seconds (green illumination) of ICMS onset.

yellow star). The M1/3a border roughly bisected the main patch. Two smaller patches were rostral to the main patch (Figure 2.4A, downward arrowheads). All patches corresponded closely with pixels that were statistically darker in the ICMS condition as compared to the Blank condition (t-test, $p<0.001$; Figure 2.4B, yellow pixels). Thus, the yellow pixels that comprised the activation map effectively reported the locations of patches with connectivity to the stimulation site. After co-registering the activation map with the motor map (Figure 2.4C), it was evident that parts of the main patch overlapped the M1 arm zone and the M1 face representation. In contrast, distant patches were almost exclusively in the M1 arm zone. Finally, retesting the same stimulation site after 280 d showed that the overall organization of the activation map was conserved (Figure 2.4D). Distant patches were more apparent in the second test, potentially due to differences in site location (inter-site distance = 193±19 μm) or state of animal. Nevertheless, overlap between the two activation maps was 74.3% in this particular example and 80.9 ± 6.8% (mean ± 1 SD) in six retested sites [days between tests = 219 ± 101 d (mean ± 1 SD); intersite distance = 125 ± 50 μm (mean ± 1 SD)]. Results from this sample of retested sites suggest that activation maps were stable over months, possibly longer.

To quantify the spatial organization of the activation maps, every pixel activated (Figure 2.4C-D, yellow) was classified according to the M1 zone that it overlapped. Pixels were then converted to surface area (13 μm^2/pixel). In the first test, the stimulation site activated ∼4 mm^2 in arm zone and ∼1.5 mm^2 in the hand zone (Figure 2.4E). The arm-to-hand ratio was comparable in the activation map of the second test. Only a small fraction of M1 activation (<1.0 mm^2) overlapped the face representation. It is important to note that the stimulation sites in both tests were <1 mm from the forelimb/face border. At such close distance, the near absence of activation in the face representation supports the likelihood that patches were driven by horizontal connections that did not cross from the forelimb representation into the face representation (Huntley and Jones, 1991; Weiss and Keller, 1994). We reached the same conclusion by stimulating a site in the M1 face representation that was no more than a few millimeters from the lateral arm sites (Figure 2.1D). That site activated patches in the face representation that covered more than four times the surface area as the activation patches in the forelimb representation.

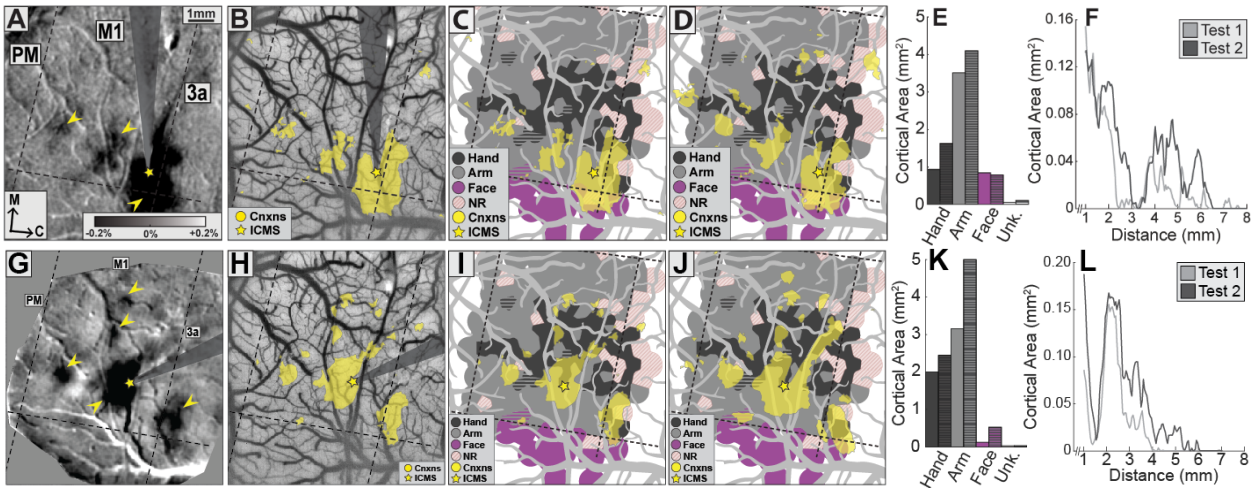

Figure 2.4: Activation maps are stable over months. (A) Average optical image: ICMS condition minus Blank condition (50 trials/condition). Average was generated from 3 frames (200 ms/frame) acquired 1000-1600 ms from ICMS onset. Gray triangle masks the stimulating microelectrode and yellow star depicts the stimulation site. Upward arrowhead points to the main activation patch and downward arrowheads point to distant activation patches. (B) Yellow pixels were significantly darker in the ICMS condition as compared to the Blank condition (t test, df = 98, $p < 0.001$). Yellow pixels constitute the activation map of the stimulation site. (C) Co-registration of the activation map with the motor map shows that most yellow pixels spatially coincided with the arm representation (light gray). (D) Activation map acquired 280 days after the test in (C). Stimulation sites in (C) and (D) were separated by 193+19 μm and there was a 74.3% overlap between their respective activation maps. Note, motor maps in (C) and (D) are reproductions of the same map. (E) Quantification of the activation maps in relation to the motor map. Tests 1 and 2 are from (C) and (D), respectively. Yellow pixels that overlapped zones not mapped with ICMS, or zones that did not respond to ICMS, are classified as Unknown. (F) Spatial distribution of the activation maps as a function of distance from the stimulation site. (G-L) Same as A-F but for a different stimulation site. (I) and (J) are separated by 175±19 μm and were acquired 280 days apart.

To quantify the spatial range of the activation maps, distance was measured between the stimulation site and every activated pixel. Spatial ranges were relatively consistent between the first and second tests. Overall, surface area of activation decayed with distance from the stimulation site (Figure 2.4F). Nevertheless, peaks and valleys in the line plots show that activation patches were punctuated by zones with no evoked activation. The present activation pattern supports the model proposed in Figure 2.1G (bottom) and argues against monotonic decline in connectivity as a function of distance (e.g. Figure 2.1G, top).

2.5.5 Arm and Hand Zones have Distinctive Activation Maps

Our next objective was to address whether arm and hand zones have the same connectivity patterns. If they do, then we would expect activation maps to have the same spatial configuration across stimulation sites regardless of their location within the M1 forelimb representation. In contrast, if connectivity patterns are governed by motor map somatotopy, then we would expect activation maps to have distinctive patterns for stimulation sites in arm and hand zones. To evaluate these competing frameworks, we compared activation maps from stimulation sites in (1) medial arm zones (Figure 2.5A), (2) hand zones (Figure 2.5B), and (3) lateral arm zones (Figure 2.5C). For each zone, we compared one stimulation site/monkey.

A main activation patch ($\sim$1 mm radius) surrounded the nine stimulation sites (Figure 2.5, 1 yellow star/panel). This is consistent with Figure 2.2, Figure 2.4, and the dozens of sites that we tested, which suggests that the main patch reflects a fundamental feature of M1 connectivity. Dense, isotropic, horizontal connections (1 mm), are the most likely driver of the main patch. Beyond the main patch, activation maps varied according to the forelimb zone stimulated. Stimulation in medial arm zones activated several distant patches that overlapped primarily with arm zones (Figure 2.5A, yellow patches). Quantifying the surface area of the patches confirmed a $\sim$3-to-1 arm-hand distribution that was consistent across animals (Figure 2.5A, bar plot). Line plots show the long spatial range (up to 5-6 mm) of these activation maps and their relative consistency across animals (Figure 2.5A). Stimulation in lateral arm zones evoked activation maps (Figure 2.5C) that were akin to

mirror images of the activation maps in Figure 2.5A. Similarities between the two sets of activation maps were also evident in the arm-hand distribution of patches (Figure 2.5A & Figure 2.5C, bar plots).

Stimulation in hand zones evoked activation maps that differed in several ways from those evoked from stimulation in arm zones. First, patches evoked from hand sites were concentrated in the center of the forelimb representation (Figure 2.5B). Second, patches overlapped primarily with hand zones (Figure 2.5B, bar plot). Third, distant patches were much closer to the main patch and in many instances fused with the main patch. This was evident in the limited (∼2-3 mm) spatial range of the activation maps (Figure 2.5B, line plot). Thus, arm and hand sites evoked activation maps with distinctive spatial configurations, which suggests that intrinsic M1 connectivity is closely linked to the somatotopy of the forelimb representation. This observation does not support the possibility of a universal intrinsic M1 network that simply repeats throughout the forelimb representation.

2.5.6 Population of M1 Sites Confirm Differential Connectivity for Arm and Hand Zones

Activation maps from a population of M1 sites (64 total: 33 arm, 16 hand, and 15 mixed) were quantified with the same approach used for the representative sites in Figure 2.5. Mixed sites were in zones that evoked both arm and hand movements. Activation maps differed in size between the 3 site categories (Figure 2.6A; ANOVA, $F_{2,61} = 4.65$, $p = 0.013$). Hand sites activated the smallest maps (mean = 3.45 mm^2) as compared to arm (mean = 4.30 mm^2, Tukey's HSD test, $p = 0.043$) and mixed sites (4.63 mm^2, Tukey's HSD test, $p = 0.015$). Similarly, the spatial range of the activation maps differed between the 3 site categories (Figure 2.6B; ANOVA, $F_{2,61} = 7.63$, p =0.001). Spatial ranges were shorter for hand sites (mean = 1.13 mm) as compared to arm sites (mean = 1.55 mm, Tukey's HSD test, $p = 0.001$) and to mixed sites (mean = 1.45 mm, Tukey's HSD test, p =0.043). Collectively, the results show that activation maps from hand sites were small and spatially restricted as compared to arm and mixed sites. Thus, results from the population of M1 sites support our observations (Figure 2.5) of distinctive connectivity patterns for arm and hand zones.

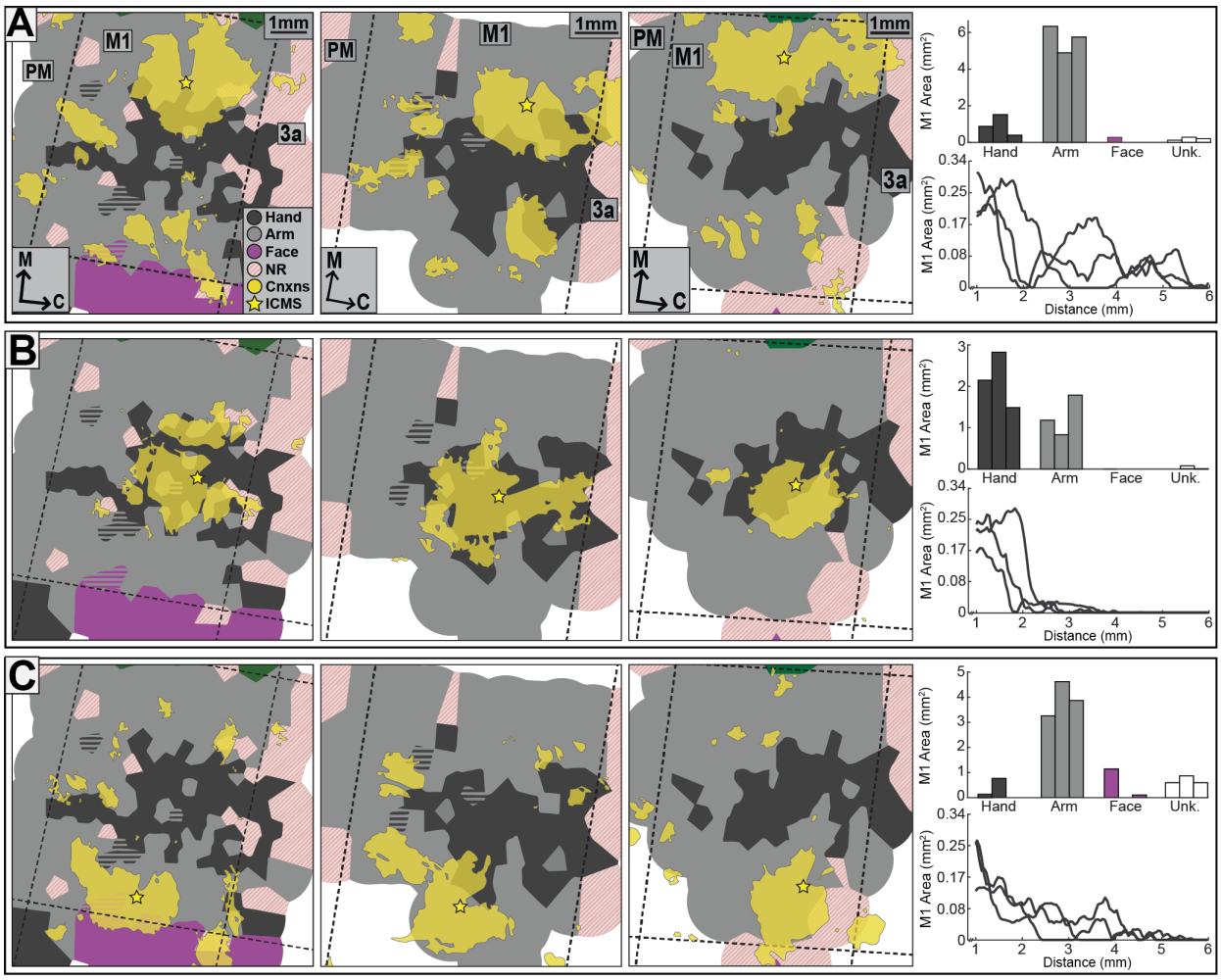

Figure 2.5: Arm and hand zones have distinctive activation maps. Activation maps from nine stimulation sites (three sites/monkey) co-registered with respective motor maps. Yellow stars depict stimulation sites. Yellow pixels were significantly darker in the ICMS condition as compared to the Blank condition (t test; $p < 0.001$). (A) Activation maps (one map/monkey) for stimulation sites in medial aspects of the arm zone. Activation maps have consistent patterns across animals despite small differences in the locations of the stimulation sites. Bar plot shows that activation was primarily in the arm zone. Line plot shows the spatial range of the three activation maps as a function of distance from stimulation sites. (B) Activation maps evoked from stimulation in the hand zone. Bar plot and line plot follow the same format in (A). (C) Activation maps in response to stimulation sites in lateral aspects of the arm zone. Note, that the bar and line plots in (B) were clearly different from those in (A) and (C).

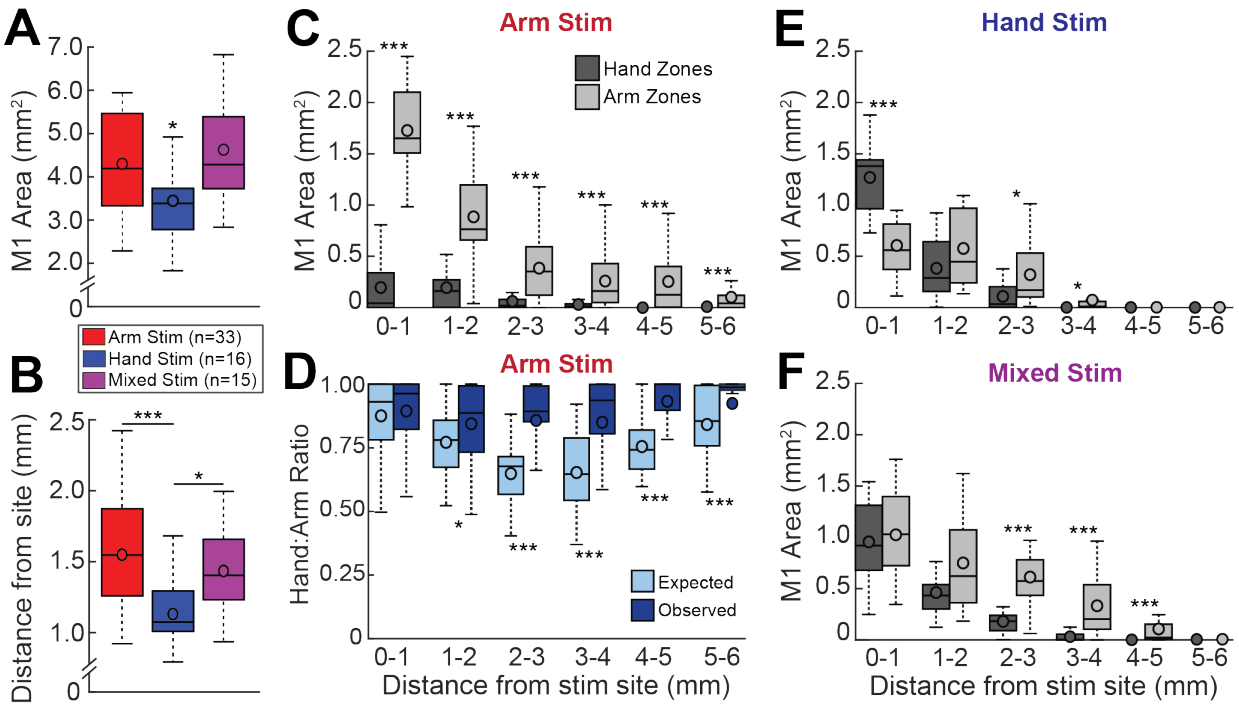

Figure 2.6: Population of M1 sites confirm differential connectivity for arm and hand zones. (A) Size of activation maps evoked from stimulation in arm sites, hand sites, or mixed sites. (B) Spatial range of activation maps computed from the average distance between ICMS sites and pixels that constitute the activation maps. $^{*}p < 0.05$, $^{***}p < 0.001$ (Tukey's HSD test). (C) Contrasting the spatial range of the activation maps evoked from stimulation in arm and hand zones; 1 mm intervals are referenced from the stimulation sites. Independent comparisons were conducted at every interval (Wilcoxon rank sum test, 0–1 mm: Z = -6.90, $p = 5.4 * 10^{-12}$; 1-2 mm: Z = -6.11, $p = 1.0 * 10^{-9}$; 2-3 mm: Z = -4.81, $p = 1.5 * 10^{-6}$; 3-4 mm: Z = -4.87, $p = 1.1 * 10^{-6}$; 4-5 mm: Z = -4.55, $p = 5.4 * 10^{-6}$; 5-6 mm: Z = -5.06, $p = 4.2 * 10^{-7}$). (D) At every interval, the surface area activated (observed) was directly compared to the surface area that could have been expected (expected) from the arm-to-hand ratios (Wilcoxon rank-sum test, 0–1 mm: Z = -0.45, $p = 0.66$; 1-2 mm: Z = -2.20, $p = 0.03$; 2-3 mm: Z = -5.25, $p = 1.5 * 10^{-7}$; 3-4 mm: Z = -4.75, $p = 2.1 * 10^{-6}$; 4-5 mm: Z = -4.91, $p = 9.3 * 10^{-7}$; 5-6 mm: Z = -3.79, $p = 1.5 * 10^{-4}$). (E) Same as (C), but for hand sites (Wilcoxon rank-sum test, 0–1 mm: Z = -3.86, $p = 1.1 * 10^{-4}$; 1-2 mm: Z = -1.64, $p = 0.10$; 2-3 mm: Z = -2.24, $p = 0.03$; 3-4 mm: Z = -2.22, $p = 0.03$). Same as (C), but for mixed sites (Wilcoxon rank-sum test, 0–1 mm: Z = -0.46, $p = 0.65$; 1-2 mm: Z = -1.53, $p = 0.13$; 2-3 mm: Z = -3.57, $p = 3.6 * 10^{-4}$; 3-4 mm: Z = -3.51, $p = 4.5 * 10^{-4}$; 4-5 mm: Z = -4.19, $p = 2.7 * 10^{-5}$).

Our next objective was to quantify the activation maps in relation to the motor maps. To that end, the surface area activated in arm and hand zones was measured using the same approach in Figures 2.4 and 2.5. We then compared the amount of surface area activated in hand and arm zones (Wilcoxon rank sum test) at 1 mm intervals from the stimulation site. In all three site classifications, activation maps decreased in size with distance from the stimulation site (Figure 2.6C, E, F). In addition, the extent to which activation maps overlapped with arm and hand zones depended on the motor output of the stimulation site. These results further support the likelihood that arm and hand zones are endowed with distinctive connectivity patterns and do not conform to one connectivity motif.

2.5.6.1 Arm Sites Only arm sites activated patches as far as 5-6 mm from stimulation site. This was consistent with observations that arm sites had the longest connectivity range (Figure 2.6B). Also, at every distance interval from the stimulation site, more surface area was activated in arm zones as compared to hand zones (Figure 2.6C). We investigated whether this size difference could have simply resulted from the M1 forelimb representation having larger arm zones than hand zones (Figure 2.1). We reasoned that *observed activation* (i.e. actual size of patches) would not be different from *expected activation* (i.e. hypothetical size of patches) in the event that activation maps simply reflect size differences between arm and hand zones in the forelimb representation. Thus, for a given activation map, at every 1-mm interval from the stimulation site, we computed the ratio of surface area activated within the arm zone:

[area activated in arm zone / (area activated in hand zone + area activated in arm zone)]

Similarly, for a given motor map, at every 1-mm interval from the stimulation site, we computed the ratio of surface area of the arm zone:

[area of arm zone / (area of hand zone + area of arm zone)]

Finally, we compared the observed activation to the expected activation at 1-mm intervals (Wilcoxon rank-sum test). With the exception of the first interval, we found that the observed activation was consistently larger than the expected activation (Figure 2.6D). Thus,

more surface area was activated in the arm zone than could be expected from the topography of the forelimb representation. Similarly, less surface area was activated in the hand zone than could be expected from the topography of the forelimb representation. Discrepancy between *observed* and *expected activation* supports the likelihood of spatially selective connectivity for sites in the arm zone.

2.5.6.2 Hand Sites Unlike arm sites, hand sites did not activate patches beyond 3-4 mm from stimulation (Figure 2.6E). In the first 1-mm interval, more area was activated in hand zones as compared to arm zones. Beyond the first interval, activation was distributed evenly between arm and hand zones (1-2 mm), or overlapped more with arm zones (2-3 mm). Nevertheless, the ratio of arm-hand activation (*observed activation*) did not differ from the ratio of arm-hand zones (*expected activation*) in the motor map.

2.5.6.3 Mixed Sites Activation maps here were in between activation maps from arm and hand sites. Patches were present as far as 4-5 mm from stimulation (Figure 2.6F). Within 2 mm of stimulation, the area activated was comparable between arm and hand zones. However, beyond 2 mm, activation was almost entirely in arm zones. Like hand sites, *observed activation* and *expected activation* (not shown) were not different for mixed sites.

2.5.7 Activation Maps Recapitulate the Forelimb Representation

We sought to visualize the activation maps for the populations of arm and hand sites. From the results in Figure 2.6, we reasoned that superimposing activation maps from arm sites would lead to patches overlapping primarily in the arm zone (Figure 2.7A,D,G, light gray). Similarly, we expected activation maps from hand sites to overlap mostly in the hand zone (Figure 2.7A,D,G, dark gray). Indeed, in all 3 monkeys, arm sites activated patches that were concentrated in arm zones and largely avoided the center of the forelimb representation (Figure 2.7B,E,H). This spatial pattern was most evident in Figure 2.7B, which had the largest number of stimulation sites in the arm zone. In contrast, hand sites activated patches that were most densely concentrated in the hand zone and had limited

overlap with the arm zone (Figure 2.7C,F,I). Thus, the activation maps from stimulation in arm sites and hand sites recapitulate the topography of the forelimb representation.

2.5.8 Selective Overlap Between Activation Maps

We investigated the relationship between site classification and spatial coincidence of M1 networks. We compared overlap in activation maps between all *matching pairs* (i.e. pairs of arm sites and pairs of hand sites) and all *non-matching pairs* (i.e. one arm site and one hand site). For *matching pairs* and *non-matching pairs*, overlap between activation maps declined with inter-site distance (Figure 2.8A; 418 total pairs across three animals). This was consistent with our observation that surface area of activation declined with distance from stimulation (Figures 2.5 & 2.6). In addition, at every distance interval, activation maps from *matching pairs* had more overlap than activation maps from *non-matching pairs* (Wilcoxon rank-sum test; Figure 2.8A). For example, several overlapping patches were observed from a *matching pair* of sites on opposite sides of the arm zone (Figure 2.8B, red). In contrast, activation maps from an arm site and a hand site had nearly no overlap (Figure 2.8C) despite closer inter-site distance as compared to the *matching pair* (Figure 2.8B). Thus, the results collectively show that networks that control the same forelimb segment overlap more with each other than with networks that control other segments of the forelimb.

2.5.9 Reciprocal Connectivity Between Patches of an Activation Map

Our next objective was to examine the spatial selectivity of the networks that link activation patches. To that end, we used one activation map as a reference (Figure 2.8D, green) for planning four stimulation sites (Figure 2.8D, yellow stars) that would yield four activation maps (Figure 2.8E-H). Sites E and G targeted patches of the reference map (Figure 2.8D). Both stimulation sites activated at least one distant patch that spatially coincided with the location of the reference stimulation site (Figure 2.8E-G, coincidence of green star with yellow patch). For direct comparison, sites F and H were purposely placed to avoid patches from the reference map (Figure 2.8D). Moreover, sites F and H were matched with sites E and G for distance with respect to the reference site. None of the patches from

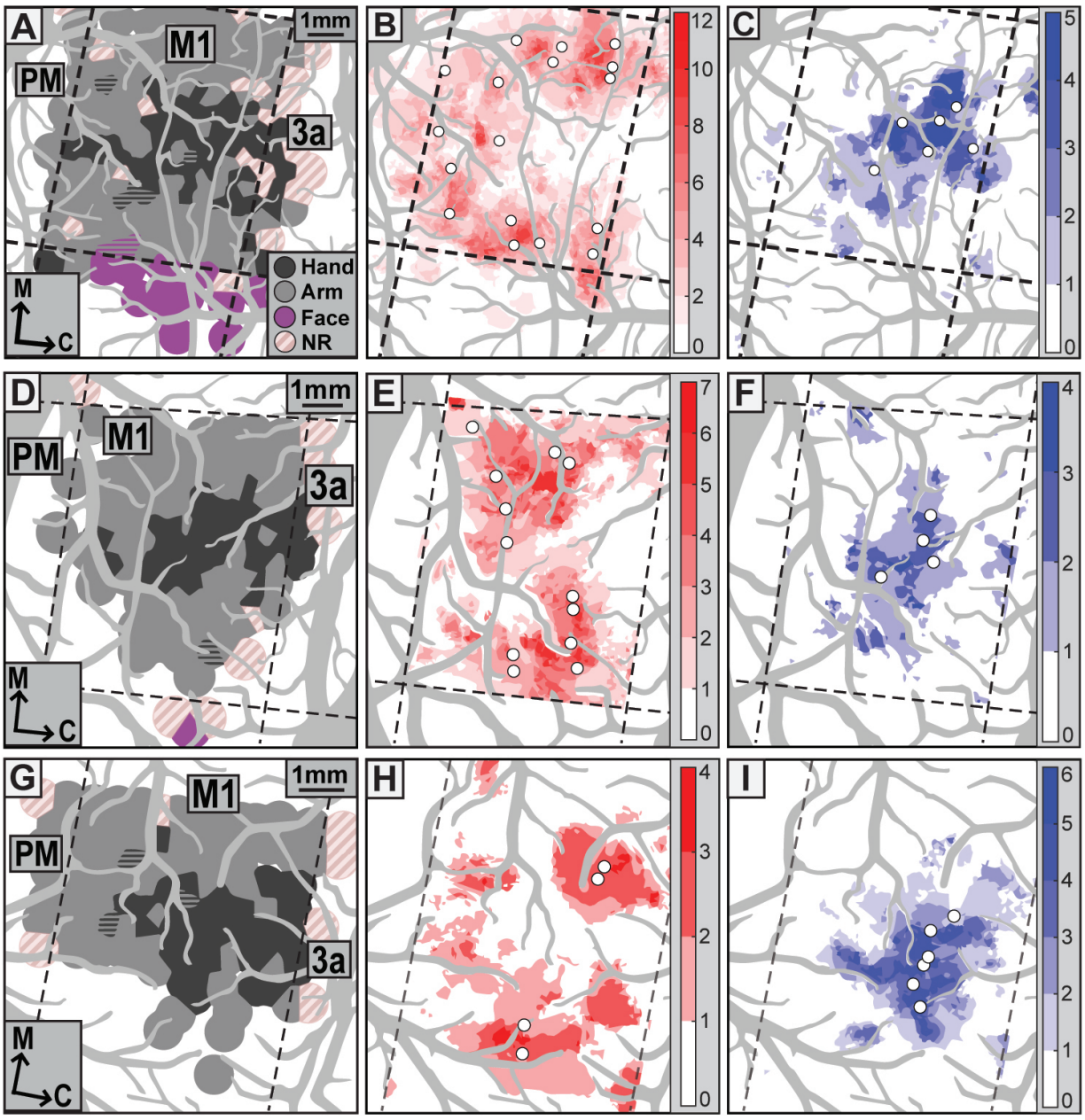

Figure 2.7: Activation maps recapitulate the forelimb representation. Results from 3 squirrel monkeys (M, R, and D) are on successive rows. (A) Motor map shown for reference. (B) Activation maps from 17 ICMS sites throughout the arm zone. Pixel intensity indicates the number of sites that activated a given pixel. (C) Activation maps from six ICMS sites in the hand zone. (D-F) Follow the same format of (A-C), but with 12 sites in the arm zone and four sites in the hand zone. (G-I) Include four sites in the arm zone and six sites in the hand zone.

sites F or H overlapped with the vicinity of the reference site (Figure 2.8F,H). We extended the present analysis to all site pairs with an intersite distance ≥2 mm. The relationship observed between reference and stimulation sites in Figure 2.8E,G was present in 7/10 site pairs (intersite distance = 2820 ± 620 μm, mean ± 1 SD). Similarly, the relationship observed between reference and stimulation sites in Figure 2.8F,H was present in 177/188 site pairs (intersite distance = 2950 ± 740 μm, mean ± 1 SD). Thus, the results collectively indicate that patches that comprise an activation map are reciprocally connected with the reference site.

2.5.10 Validation Experiments

Our results from dozens of stimulation sites confirm the effectiveness of ICMS+ISOI for mapping cortical connectivity. Nevertheless, mapping brain networks with ICMS+imaging (ISOI or fMRI) is relatively new and differs mechanistically from well-established neuroanatomical tracing methods. This motivated us to test ICMS+ISOI in well-defined cortical networks before using the approach to reveal the organization of the understudied M1 networks. Somatosensory cortical areas were an excellent testbed for several reasons. (1) Connections have been studied extensively with tracer injections. (2) Somatosensory maps can be exploited for spatial quantification of the activation maps. (3) Accessibility from the same cranial window used for M1.

2.5.10.1 ICMS+ISOI Connectivity is Consistent With Previous Tracer Injections Our objective was to determine if stimulation in representations of individual digits (areas 3b and 1) would evoke activation maps comparable to connectivity patterns revealed with neuroanatomical tracers (Liao et al., 2013; Négyessy et al., 2013). In two monkeys (M and G in Table 2.1), we used microelectrode recordings to map somatosensory representations of the hand (Figure 2.9A,B). Our maps were consistent with somatotopy long-established for New World monkeys (Kaas et al., 1979; Merzenich et al., 1978). Next, we investigated four somatosensory sites (two sites/monkey) using the same ICMS+ISOI parameters that were applied in M1.

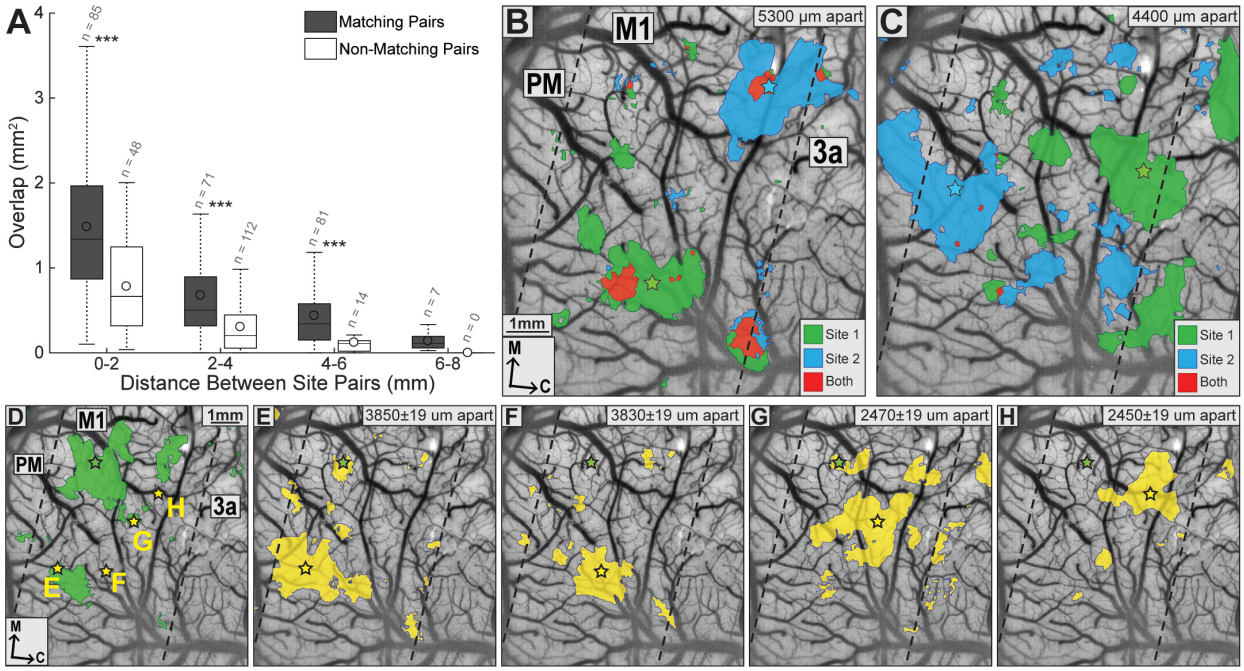

Figure 2.8: Overlap between activation maps is related to site identity and inter-site distance. (A) Spatial overlap between pairs of activation maps (418 comparisons; 3 animals). Comparisons are grouped according to inter-site distance and whether sites are matching (e.g. 2 arm sites) or non-matching (i.e. 1 arm site and 1 hand site). Overlap between activation maps declined with inter-site distance. Overlap was consistently greater for matching sites than for non-matching sites (Wilcoxon rank-sum test, 0-2 mm: Z = 4.51, $p = 6.4 * 10^{-6}$; 2-4 mm: Z = 5.82, $p = 5.9 * 10^{-9}$; 4-6 mm: Z = 3.49, $p = 4.8 * 10^{-4}$). (B) Activation maps from a pair of matching sites. Stimulation sites (green and blue stars) were 5300 μm apart. The 2 activation maps (green and blue patches) overlapped in several locations (red). (C) Activation maps (blue and green) from a pair of non-matching sites (4400 μm apart) had almost no overlap (red). (D) Reference activation map (green patches) in response to stimulation at the green star. Yellow stars mark the locations of four stimulation sites. Sites E and G were placed to overlap green patches. Sites F and H were placed to avoid green patches. (E-H) Activation maps evoked from corresponding stimulation sites in (D). For each activation map, stimulation was delivered in the location of the yellow star. Green stars are included for reference only. Inter-site distance (yellow and green star) is in the top right corner of each activation map. Reciprocal connectivity (overlap between green star and yellow pixels) is evident in (E) and (G), but not in (F) or (H).

For the first stimulation site in area 3b, the microelectrode was in the representation of the distal phalanx of the fourth digit (i.e., distal D4). The activation map was comprised of three patches (Figure 2.9C). The main patch (∼1 mm radius) was approximately centered on the stimulation site (Figure 2.9C, yellow star) and mostly overlapped distal D4 followed by distal D3. This patch also encroached into caudal aspects of area 3a. The other two patches were located in area 1 where they overlapped D4 and D3. Similar activation patterns were obtained from a second stimulation site in area 3b where the microelectrode was in proximal D1 (Figure 2.9D). The main activation patch was located in area 3b and surrounded the stimulation site (yellow star). Distant patches were smaller and confined to a narrow medio-lateral strip within area 1.

Next, we investigated 2 sites in area 1. The first site activated a main patch that was elongated in the rostro-caudal direction and straddled areas 3b and 1 (Figure 2.9E). This patch was largely confined to proximal D4 and D3. Most of the activation in area 3b likely belonged to a distant patch that fused with the main patch in area 1. Smaller patches in areas 3a and 2 were in the same medio-lateral strip as the main patch. The lateral patch in area 1 overlapped the palm. These results were confirmed in a second stimulation site in area 1 (Figure 2.9F) where most of the activation was confined to the matching digit in area 3b.

Activation maps from the 4 somatosensory sites corresponded closely with connection patterns revealed with neuroanatomical tracer injections into somatosensory representations of individual digits (Liao et al. (2013), their Fig. 7; Négyessy et al. (2013), their Figs. 7, 9). The near absence of activation patches in M1 and limited spread of activation patches in the medio-lateral direction ($\leq$ 2 digit representations) was also consistent with the tracer studies. Thus, our somatosensory results confirm the reliability of ICMS+ISOI for mapping cortical networks.

2.5.10.2 Activation Maps are Conserved Across Stimulation Intensities Simulation parameters have caried considerable across studies that investigated connectivity using ICMS+imaging (ISOI or fMRI). It was therefore important here to test how systematic vari-

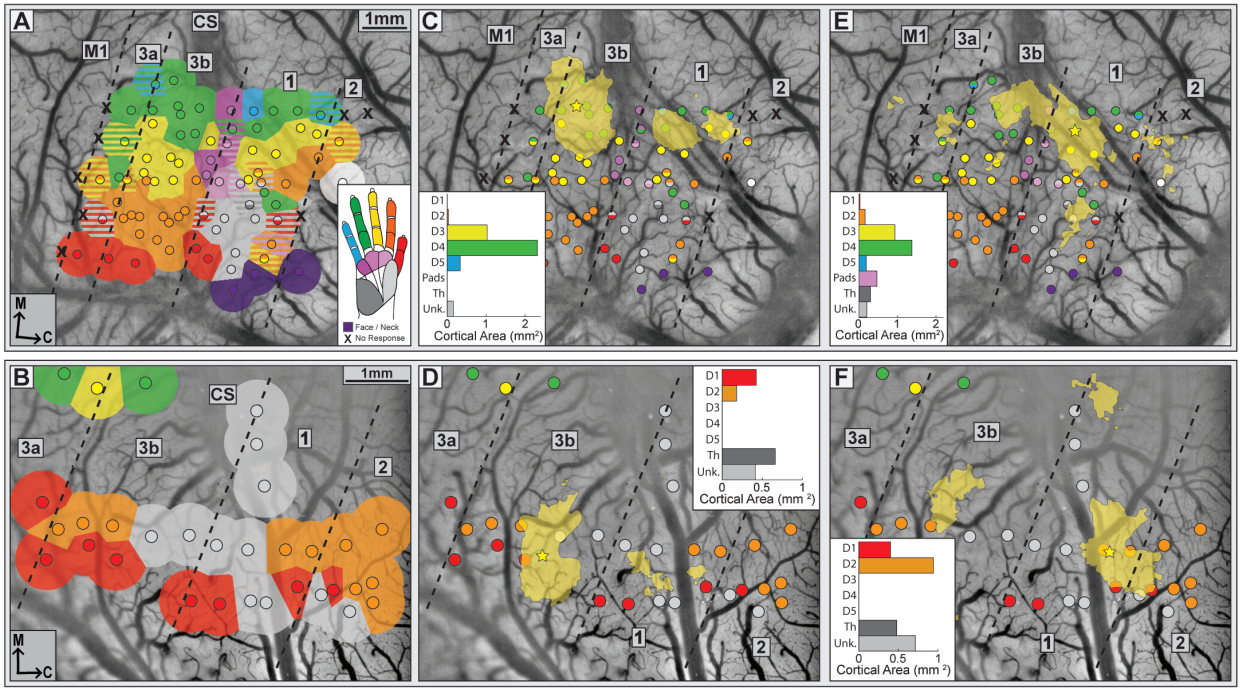

Figure 2.9: Somatosensory cortex connectivity is consistent with previous tracer injections. Top row, monkey M. Bottom row, monkey G. (A) Map of the somatosensory hand representation. Microelectrode recording sites (colored circles, n=87) were classified according to multi-unit responses to receptive field mapping. Voronoi tiles (0.5 mm radius) are color-coded according to the hand illustration. Striped tiles included 2 representations (1 color/representation). Cortical borders (dashed lines) were estimated from receptive field mapping results. D1-D5: digits 1-5; Th: thenar. (B) Partial map of the somatosensory hand representations in monkey G (n=35 sites). (C) Activation map (yellow patches) evoked in response to stimulation in a site (yellow star) within digit 4 in area 3b. Receptive field mapping sites are shown for reference. Bar plot shows the organization of the activation map in relation to the somatosensory map. Activation patches that overlapped unresponsive zones or unmapped zones are classified as "Unknown". (D) A similar activation map was evoked for a stimulation site within digit 2 in area 3b. (E) Activation map for an ICMS site that straddled the representations of digits 3 and 4 in area 1. (F) Activation map for an ICMS site within digit 2 in area 1.

ations in stimulation parameters might affect the evoked cortical response. We focused on microelectrode depth, current amplitude, train duration, and pulse frequency. Only one parameter was tested in each M1 site.

2.5.10.3 Microelectrode Depth We expected the most intense activation from depths in which the microelectrode was far enough from the cortical surface to at least reach layers 2/3 ($\sim$1000 μm from surface). Five stimulation depths were tested (200, 600, 1000, 1400, and 1800 μm) using the same ICMS parameters for M1 connectivity (150 biphasic pulses, 0.2 ms pulse width, 300 Hz, 60 μA). Locations of the main patch (Figure 2.10A, yellow star) and the distant patches (arrowheads) were consistent across depths. However, distant patches grew in size with microelectrode depth. The effect was most evident 4-5 mm from the stimulation site (Figure 2.10C) and could be attributed mostly to size differences in the patch near the border with area 3a (Figure 2.10A). Distant patches in general appear to have been the primary factor in the step-wise increase in the size of the activation maps for stimulation depths 1000 and 1400 μm (Figure 2.10B). This is consistent with previous work showing that the longest horizontal connections originate in layer 5 (Aroniadou and Keller, 1993). That activation maps were comparable in size for stimulation depths 1400 and 1800 μm supports the likelihood that horizontal connections, as opposed to white matter axons, were the main driver of the activation maps.

2.5.10.4 Pulse Amplitude Three pulse amplitudes were tested (20, 40, 60 μA) while other ICMS parameters remained constant (1000 μm depth, 150 biphasic pulses, 0.2 ms pulse width, 300 Hz). For the two lowest pulse amplitudes, the number of trials was set to match the total charge transfer achieved in 50 trials of 60 μA pulses (i.e. 150 trials for 20 μA pulses; 75 trials for 40 μA pulses). The main patch (yellow star) and distant patches (arrowheads) were consistent in location for the 3 current amplitudes (Figure 2.10D). Nevertheless, activation maps increased in size with current amplitude (Figure 2.10E). These size differences were most apparent for distant patches, particularly at 4 mm from the stimulation site (Figure 2.10F).

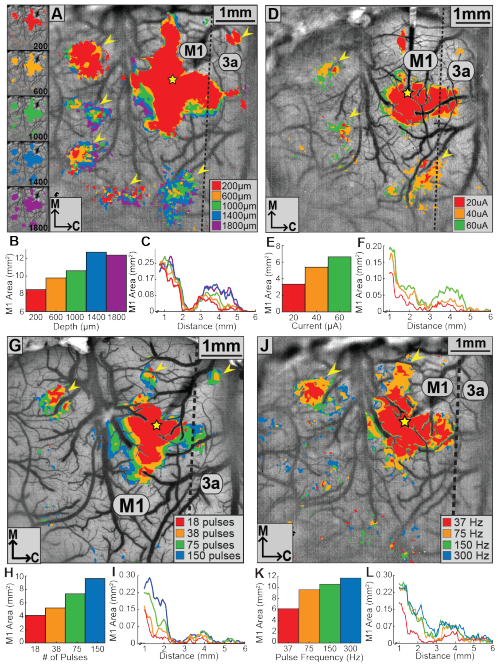

Figure 2.10: Activation maps are conserved across stimulation parameters. (A-C) Microelectrode depth. (A) Left column, activation maps evoked in response to stimulation at 5 cortical depths. Depth (μm) from surface of cortex is in the bottom right corner of each activation map. The five activation maps are superimposed onto each other in the main panel. Yellow arrowheads point to distant patches of activation. (B) Size of activation maps increased with stimulation depth (up to 1400 μm). (C) Line plot colors match bar colors in (B). Activation maps had a spatial range that extended up to 5 mm from the stimulation site. The two deepest stimulation depths activated the most amount of cortex, which was most evident 3-5 mm from the stimulation site. (D-F) Current amplitude. (D) Activation maps evoked in response to the same ICMS train at 3 current amplitudes: 20, 40, and 60 μA. Number of trials was set to match the charge delivered in each condition (50 trials of 60 μA, 75 trials of 40 μA, and 150 trials of 20 μA). (E) Size of activation maps increased with pulse amplitude. (F) Line plot colors match bar colors in (E). Activation maps had comparable spatial ranges, but the 60 μA condition activated larger distant patches (3-5 mm interval). The activation map of the 20 μA condition was relatively small throughout its spatial range. (G-I) Train duration. (G) Activation maps evoked in response to M1 stimulation with varying train durations: 18, 38, 75, 150 pulses/train. The number of trials was set to match the charge delivered in each condition (50 trials of 150 pulses/train, 100 trials of 75 pulses/train, 200 trials of 38 pulses/train, and 400 trials of 18 pulses/train). (H) Size of activation maps increased with train duration. (I) Line plot colors match bar colors in (H). The longest train durations (75 and 150 pulses/train) activated the largest main patches as evident from the surface area differences at 1-2 mm. (J-L) Pulse frequency. (J) Activation maps evoked in response to M1 stimulation with varying pulse frequencies: 37, 75, 150, and 300 Hz. To account for longer activation times associated with the lower pulse frequencies, activation maps include any pixels activated within 6 s of ICMS onset. (K) Size of activation maps increased with pulse frequency. (L) Line plot colors match bar colors in (K). Activation maps had comparable spatial ranges except for the 37 Hz condition, which was smaller throughout its range. Experiments in this figure were conducted in the right hemisphere of monkey D. Panels are reflected for consistency with other figures. Shadow of the stimulating microelectrode is evident in (D) and (G).

2.5.10.5 Train Duration Four train durations (18, 38, 75, 150 pulses/train) were tested while other ICMS parameters were constant (1000 μm depth, 40 μA, 0.2 ms pulse width, 300 Hz). For the three shortest trains, the number of trials was set to match the total charge transfer achieved in 50 trials of 150 pulses/train (i.e. 417 trials for 18 pulses; 198 trials for 38 pulses; 100 trials for 75 pulses). Spatial organization was conserved for the main patch (Figure 2.10G, star) and the distant patches (Figure 2.10G, arrowhead) across train durations. Nevertheless, activation maps increased in size consistently with train duration (Figure 2.10H). The most apparent size difference was within 1-2 mm from the stimulation site and therefore within the main patch (Figure 2.10I).

2.5.10.6 Pulse Frequency Four pulse frequencies (37, 75, 150, 300 Hz) were tested while other stimulation parameters were constant (1000 μm depth, 150 biphasic pulses, 0.2 ms pulse width, 60 μA). Train durations were adjusted to achieve 150 pulses/trial. Number of trials was consistent between conditions. Spatial organization was conserved for the main patch (Figure 2.10J, star) and for distant patches (Figure 2.10K, arrowheads) across the pulse frequencies tested. Activation maps increased in size with pulse frequency (Figure 2.10K). The increase in size of the activation map occurred at all spatial intervals from the stimulation site (Figure 2.10L).

2.6 Discussion

We investigated the intrinsic connectivity of the M1 forelimb representation in an effort to understand organizational principles of intrinsic M1 networks. ICMS+ISOI allowed us to measure connectivity *in vivo* and at high spatial resolution. ICMS+ISOI conferred scale (i.e., number of sites), field-of-view, and spatial resolution needed to identify connectivity rules. These rules converged onto an overarching principle where intrinsic M1 connectivity links functionally matching patches.

2.6.1 Tracing Connectivity with ICMS+ISOI

ICMS+imaging remedies a critical bottleneck that arises in studying cortical connectivity with a limited number of distinguishable tracers. Although ICMS+imaging is a relatively new approach, its reliability has been shown in several cortical networks. For example, ICMS+fMRI has been used successfully in mapping the connectivity of frontal eye fields with visual areas (Ekstrom et al., 2008); the connectivity of primary visual cortex (V1) with extrastriate cortex (Tolias et al., 2005); the intrinsic connectivity of the face-processing and body-processing systems in inferotemporal cortex (Moeller et al., 2008; Premereur et al., 2016). Similarly, ICMS+ISOI has been used to reveal parietal-frontal connectivity (Stepniewska et al., 2011) and connectivity of somatosensory areas (Friedman et al., 2020). Although fMRI and ISOI are no match for the spatial resolution achieved with tracers, the activation patches revealed with ICMS+imaging correspond closely with patches monosynaptically labeled from tracer injections (Stepniewska et al., 2009; Négyessy et al., 2013; Grimaldi et al., 2016). ICMS+imaging is therefore a suitable alternative to tracers that is particularly desirable for investigating large numbers of sites with overlapping connections; precisely what was needed here for the M1 forelimb representation.

We favored ISOI over fMRI for two reasons. First, ISOI provides superior spatial resolution (13 μm/pixel here). Second, ISOI detects hemodynamic responses to microstimulation current amplitudes $\geq$10x smaller than needed for a reliable BOLD response (Tolias et al., 2005; Premereur et al., 2016; Matsui et al., 2011). The connectivity patterns that we identified in four sites within the digit representations of areas 3b and 1 corresponded closely with feedforward and feedback connections of single digit representations (Liao et al., 2013; Négyessy et al., 2013). Moreover, our activation maps showed little/no evidence of activation spreading trans-synaptically or by fibers of passage. Either of these issues would have resulted in activation patches in locations not supported by tracer injections (e.g. inappropriate digit representation). We also showed that systematic manipulation of microstimulation parameters mostly affected patch size (Figure 2.10) without disturbing the spatial organization of activation maps. These observations support the likelihood that our activation maps were primarily driven by monosynaptic connections from the stimulation site. We note that

trans-synaptic effects reported in visual areas in response to lateral geniculate stimulation (Logothetis et al., 2010) may have resulted from relatively high current amplitudes or may reflect genuine differences in signal propagation from thalamic stimulation versus cortical stimulation. It is therefore important in future work to directly compare stimulation evoked activation and tracer injections in the same cortical sites. Perhaps of equal importance is the need to directly compare stimulation evoked activation with other causal methods such as optogenetics and with non-causal methods such as time-series correlations from resting state activity.

2.6.2 Intrinsic M1 Connectivity is Patchy

Stimulation of M1 forelimb sites activated patches within M1. Activation patterns were consistent with previous M1 tracer injections that labeled clusters of cell-bodies and axon-terminals, which appeared as patches in tangential sections or radial columns in cross sections (Huntley and Jones, 1991; Keller, 1993; Lund et al., 1993). The patchy pattern of intrinsic M1 connections has generally been underreported as M1 studies have largely focused on extrinsic connections (e.g. cortical-cortical, thalamocortical, corticospinal). A case-in-point is our own M1 injections that unmistakably labeled patches of cell bodies within M1 (Gharbawie et al., 2010, their Figs. 6, 7), but that pattern was scarcely discussed in favor of focusing on cortical inputs to M1.

We note that others have argued in favor of an alternative organization wherein a point within the M1 forelimb representation is connected widely with the rest of the forelimb representation (Capaday et al., 2009, 2011). This framework was grounded in the distribution of synaptic boutons throughout the lengths of projection axons (Capaday et al., 2009). Our results from dozens of stimulation sites in M1 indicate that activation patterns are patchy. This raises the possibility that ICMS evoked responses in locations where boutons clustered and/or had high synaptic strength. Indeed, close examination of the distribution of boutons in Capaday et al., 2009 (their Figs. 3,4,8) shows that beyond the main tracer update zone

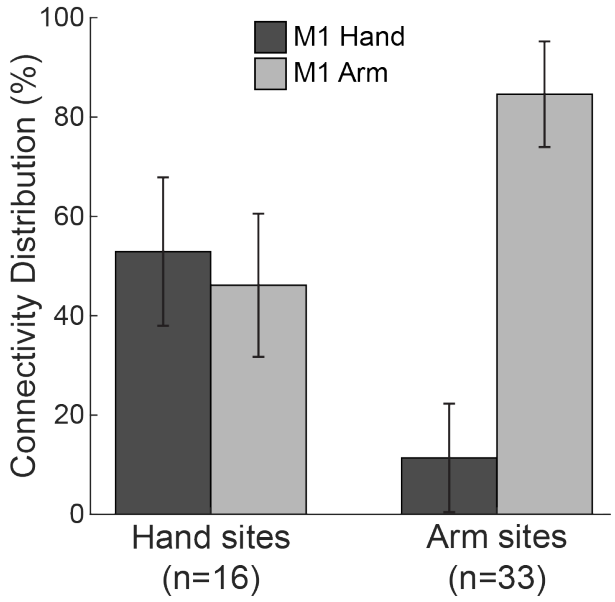

Figure 2.11: Summary of intrinsic M1 connectivity for arm and hand zones. Results (mean ± 1 SD) are based on quantification of activation maps from all arm sites (n = 33) and hand sites (n = 16). Arm sites mostly activated patches in the arm zone indicating preferential connectivity between functionally matching patches. Hand sites showed connectivity between functionally matching patches and non-matching patches.

(∼1.5 mm), zones of labeled synaptic boutons were punctated by label-devoid zones. This pattern of labeling is generally regarded as patchy and likely reflects the spatial organization of the long-range horizontal connections.

The main activation patch that surrounded our ICMS sites extended tangentially for ∼1.0 mm radius. The size of the main patch was consistent with the signal propagation patterns recorded with microelectrode arrays in response to focal stimulation in M1 (Capaday et al., 2011; Hao et al., 2016). The main patch is perhaps equivalent to the "halo" of dense labeling in tracer injections. Consistent organization of the main patch across dozens of M1 sites indicates that any point within M1 is endowed with short-range horizontal connections that are dense and have a high concentration of synaptic boutons (Gatter et al., 1978; Capaday et al., 2009). It is important to note that the main patch extended well-beyond the estimated range of passive current spread (150-500 μm) for our current amplitudes (Stoney et al., 1968). Given the point spread function of intrinsic signals (Grinvald et al., 1994; Johnson and Frostig, 2016), it is possible that the main patch overestimated the range of the horizontal connections that surrounded each stimulation site but perhaps by no more than 175 μm (Vazquez et al., 2014).

Beyond the main patch, intrinsic M1 connectivity was quite distinctive for arm sites and hand sites. Stimulation in arm sites typically drove multiple distant patches that were in some instances as far as 7 mm from the stimulation site. In contrast, hand sites scarcely activated patches 3 mm beyond the stimulation sites. In either case, the long-range projections of pyramidal neurons were likely the substrate for transmission of activity from the ICMS site to distant patches (Hao et al., 2016; Keller and Asanuma, 1993).

2.6.3 Intrinsic M1 Connectivity is Functionally Organized

Intrinsic M1 connectivity is closely tied to the somatotopic organization of the forelimb representation. We observed from dozens of arm sites that activation patches coincided primarily with M1 arm zones. Given that arm sites have the largest footprint within the forelimb representation, we posit that preferential connectivity between functionally matching patches is a prominent organizational principle in M1 (Figure 2.11). This point is particu-

larly evident if we consider that the distant patches of arm sites were overwhelmingly located in M1 arm zones. These patches seem to avoid M1 hand zones even if they were closer to the stimulation site than arm zones. Nevertheless, the connectivity portfolio of hand sites included a larger proportion of functionally non-matching patches as compared with the connectivity portfolio of arm sites. These differences likely reflect functional specializations of the arm and hand. Connectivity between non-matching zones has been reported for the digit representation in macaque monkeys, and the wrist and arm representations in cats (Capaday et al., 2009; Huntley and Jones, 1991; Keller, 1993). However, these studies did not provide the quantification needed for determining the proportion of connectivity between matching patches and between non-matching patches. Based on the quantitative results in our study, we propose that intrinsic networks of the M1 forelimb representation are spatially organized to serve interactions between functionally matching patches and to a lower extent serve interactions between functionally non-matching patches.

The connectivity of arm and hand sites differed in spatial range and in spatial organization. This result is intuitive if we consider (1) the nested somatotopy that we reported for arm and hand zones, and (2) the preferential connectivity between functionally matching patches. Had we found that stimulation sites drove spatially-shifted copies of the same activation map, there would have been comparable likelihood of connectivity between functionally non-matching patches and functionally matching patches. However, our activation maps do not support such organization. Moreover, the four parallel cortico-cortical networks previously described for the M1 hand representation (Dea et al., 2016; Hamadjida et al., 2016) are commensurate with the existence of multiple intrinsic connectivity patterns in M1. An important next step is to determine relationships between intrinsic M1 networks and the networks that M1 forms with other cortical areas. The advantages of the ICMS+ISOI connectivity mapping paradigm are bound to be valuable in such investigations.

2.7 Conclusion

The intrinsic networks of the M1 forelimb representation appear to be governed by a general principle: connectivity is patchy and primarily links functionally matching patches. Thus, the intrinsic connectivity of M1 is intimately linked to the somatotopic organization of the M1 forelimb representation. The relationship between connectivity and other defining features such as functional architecture is a well-established organizational principle in sensory cortex. For example, intrinsic connections of V1 preferentially link matching columns as defined with cytoarchitecture (e.g. cytochrome oxidase blobs) or with neurophysiology (e.g. orientation domains; Livingstone and Hubel, 1984; Gilbert and Wiesel, 1989; Malach et al., 1993; Bosking et al., 1997). The spatial periodicity of the connections in relation to the cytoarchitectonic and functional maps is considered part-in-parcel of the modular organization of sensory cortex. Accordingly, some of the fingerprints of modularity are inherent to the intrinsic M1 organization described here.

3.0 Cortical Connectivity is Embedded in Resting State at Columnar Resolution

Text and figures from this chapter are from Card and Gharbawie (2022), reformatted for this dissertation.

3.1 Summary

Resting state (RS) fMRI is now widely used for gaining insight into the organization of brain networks. Functional connectivity (FC) inferred from RS-fMRI is typically at macroscale, which is too coarse for much of the detail in cortical architecture. Here, we examined whether imaging RS at higher contrast and resolution could reveal cortical connectivity with columnar granularity. In longitudinal experiments ($\sim$1.5 years) in squirrel monkeys, we partitioned sensorimotor cortex using dense microelectrode mapping and then recorded RS with intrinsic signal optical imaging (RS-ISOI, 20 μm/pixel). FC maps were benchmarked against microstimulation-evoked activation and traced anatomical connections. These direct comparisons showed high correspondence in connectivity patterns across methods. The fidelity of FC maps to cortical connections indicates that granular details of network organization are embedded in RS. Thus, for recording RS, the field-of-view and effective resolution achieved with ISOI fills a wide gap between fMRI and invasive approaches (2-photon imaging, electrophysiology). RS-ISOI opens exciting opportunities for high resolution mapping of cortical networks in living animals.

3.2 Introduction

Spontaneous brain activity, or resting state (RS), provides a window into the organization of brain networks (Bullmore and Sporns, 2009). RS is sampled from minutes-long recordings

of electrophysiological or hemodynamic signals that are typically acquired from the whole brain. Statistical dependencies in the recorded time series are then used to generate inferences about functional connectivity (FC) and more broadly about network organization. The capacity for imaging the entire brain non-invasively has propelled fMRI to the forefront of tools used in the acquisition of RS in both humans and animals (Fox and Raichle, 2007; Hutchison and Everling, 2012; Buckner et al., 2013). Resting state fMRI (RS-fMRI) now serves a range of interests from basic research (e.g., cross-species comparisons of brain networks) to fingerprinting brain pathophysiology (e.g., dementia and autism).

RS-fMRI generally operates on a macroscale (e.g., cortical region). With the exception of some recent work (Huber et al., 2017; Shi et al., 2017), the contrast and spatial specificity achieved in RS-fMRI obscure granular details of cortical architecture. This is notably different from the finer scale (e.g., cortical columns and layers) reported in fMRI of stimulus-evoked activity (Kim et al., 2000; Chen et al., 2013). Discrepancy between the effective resolution in the two fMRI paradigms could be related to differences in imaging protocols. Alternatively, it could reflect inherent limitations on the level of detail that can be extracted from correlating RS time series. These points can be adjudicated with optical imaging methods as they provide the signal-to-noise ratio and spatial resolution needed to map distributed cortical networks in fine detail.

Intrinsic signal optical imaging (ISOI) is an attractive candidate for optical recording of RS. ISOI measures hemodynamic response and is therefore operationally similar to fMRI (Grinvald et al., 2000). Findings from resting state ISOI (RS-ISOI) would therefore translate well to the much more widely used RS-fMRI. Even though information on cortical layers cannot be retrieved from ISOI, the method is sensitive to the columnar architecture of cortex. This feature is evident for stimulus-evoked activity in sensory cortex. For example, the columnar organization of visual cortex is captured with outstanding fidelity in ocular dominance and orientation preference maps obtained with ISOI (Bonhoeffer and Grinvald, 1991; Lu and Roe, 2007). The spatial precision of these two-dimensional maps suggests that ISOI has the potential to report FC at high resolution, which would serve many needs. For example, high resolution FC maps would improve site targeting for electrophysiological recordings and perturbations, refine interrogation of cortical rewiring, and create opportuni-

ties for addressing long-standing questions about correspondence between FC and anatomical connectivity (Hagmann et al., 2008; Greicius et al., 2009; van den Heuvel et al., 2009; Honey et al., 2009; Adachi et al., 2012).

Our objective here was to evaluate whether RS-ISOI can report cortical connectivity at columnar granularity. To that end, we benchmarked RS-ISOI against methods that are well-established for revealing cortical connectivity at the desired columnar resolution or better. Specifically, we compared FC maps from RS-ISOI to anatomically traced cortical connections and to microstimulation-evoked activation as measured with ISOI. We conducted our study in sensorimotor cortex of squirrel monkeys where we could use microelectrode mapping to identify cortical areas (i.e., cytoarchitecture) and somatotopy. We then leveraged the cortical parcellation in guiding seed placement and in quantifying connectivity maps. Near-perfect correspondence between FC maps and the benchmark connectivity maps showed that granular details of network organization are embedded in RS.

3.3 Methods

3.3.1 Animals

Experiments were performed on 2 adult male squirrel monkeys (*Saimiri boliviensis*). Animals were 4 years old and weighed between 800-1200 g. All procedures were approved by the University of Pittsburgh Institutional Animal Care and Use Committee and followed the guidelines of the National Institutes of Health guide for the care and use of laboratory animals.

3.3.2 Surgical Procedures

All procedures and data acquisition were conducted under anesthesia (Table 3.1). Thirty minutes before sedation, animals were treated with an antiemetic (Zofran, 0.3 mg/kg, IM) and Atropine (0.03 mg/kg, IM) to reduce secretions. Ketamine induction (10-15 mg/kg, IM) was followed with isoflurane (0.5-2.5%) in O2 (2-3 L/min). Once sedated, Dexamethasone (1

mg/kg, IM), Ketofen (2 mg/kg, IM), and Gentamicin (2 mg/kg, IM) were administered to prevent brain swelling, pain, and infection, respectively. Animals were intubated, artificially ventilated, wrapped in a heating blanket, and secured in a stereotaxic frame. Fluids (5% dextrose in Lactated Ringer's solution, 2-3 mL/kg/hr, IV) were provided continuously. Heart rate, arterial oxygen saturation, expired CO_2, blood glucose, and body temperature were monitored.

A scalp incision was performed for each procedure. All steps from this point were conducted with the aid of a surgical microscope. In the first procedure for each animal, a rectangular window was opened in the skull over frontal and parietal cortex ($\sim$25 x 20 mm, Fig. 3.1G). That window was accessed in multiple subsequent procedures. After a durotomy, cortical pulsations were stabilized with 3% agarose (Invitrogen, Carlsbad, CA) solution in physiological saline. Data acquisition proceeded from this point and lasted for several hours. The agar was removed at the conclusion of data acquisition and an artificial dura (Tecoflex EG-85 resin, Sakas et al., 1990) was secured into the cranial opening to protect the exposed cortex. The craniotomy was then sealed with dental cement and the scalp was sutured closed. The animal was recovered from anesthesia and another dose of the pre-procedure drugs was administered in addition to Vitamin B12 (0.5 mg/kg, IM). Analgesics and corticosteroids were administered every 12 hours for the following 72 hours. Survival procedures lasted $\sim$14 hours from sedation to alertness and terminal procedures lasted $\sim$24 hours.

3.3.3 Monitoring Animal State with EEG

Electroencephalogram (EEG) signals were recorded for monitoring animal state. Stainless steel wires (3 strand, 102 μm diameter, AM systems, Sequim, WA) were inserted into bilateral burr holes near the frontal pole and then secured with dental cement. Wires were removed at the conclusion of each procedure. The voltage differential between the two leads was amplified (10,000x), bandpass filtered (1-500 Hz), and notch filtered (60 Hz) using an AC Amplifier (Model 2800, AM Systems, Sequim, WA). The filtered signal was visualized on an oscilloscope, digitized (1000 Hz, NI USB-6008, National Instruments, Austin, TX), and recorded in MATLAB. Spectrograms and power spectra of the EEG were examined in

Table 3.1: Procedures and data collected from each animal[a]

Monkey	Procedures	Motor Map Sites	Receptive Field Sites	Resting State Recordings	Effective Connectivity Sites	Tracer Injections
B	14	264	169	13	27	2
R	13	231	251	15	21	3
Total	27	465	420	28	48	5

a. Numbers are limited to data included in the present study.

MATLAB (*spectrogram* and *FFT* functions).

Three animal states were classified from temporal and spectral qualities of the EEG. (1) *Light sedation* (0.5-1.5% isoflurane) consisted of slow waveforms; suppression was present in 0-2.0% of the recording. (2) *Semi-deep sedation* (1.75-2.0% isoflurane) consisted of slow waveforms with periodic suppression in 2.0-95.0% of the recording. (3) *Deep sedation* (2.0-2.25% isoflurane) consisted of suppression in >95.0% of the recording. Most ISOI recordings were in the light state.

3.3.4 Motor Mapping

We used intracortical microsimulation (ICMS) to map the somatotopic organization of primary motor cortex (M1) and premotor cortex (Fig. 3.1A-B). A hydraulic microdrive (Narishige MO-10, Amityville, NY) connected to a Kopf micromanipulator (Tajunga, CA) was used for positioning a platinum/iridium microelectrode (125 μm shaft, 300 kΩ median impedance, MicroProbes, Gaithersburg, MD). Each penetration targeted layer V (1800 μm deep) to deliver microstimulation trains (18 cathodal pulses, 0.2 ms pulse width, 300 Hz pulse frequency, 1 Hz train frequency) from an 8-channel stimulator (model 3800, AM Systems, Sequim, WA). Current amplitude was adjusted with a stimulus isolation unit (model BSI-

2A, BAK Electronics, Umatilla, FL) until a movement was evoked and up to a maximum of 150 μA. Threshold for a site was the minimum current amplitude that evoked movement on $\sim$50% of microstimulation trains. Combining ketamine infusion (3-6 mg/kg/hr) with low doses of isoflurane (<0.5%) was central to maintaining a state in which ICMS reliably evoked movements.

Two to three experimenters evaluated the evoked movements. Only one experimenter was not blind to the microelectrode location. Each ICMS site was classified according to joint (digit, elbow, etc.) and movement type (e.g., flexion, extension, etc.) that showed the most robust effect at the lowest current amplitude. Mapping was completed over several procedures (30-60 ICMS sites/procedure). Distance between ICMS sites was typically $\leq$1 mm. Sites were recorded on a high-resolution photo of cortex. Color coded maps were generated in MATLAB using a Voronoi diagram (*voronoi* function) constrained to 1.0 mm radius per site. Rostral and caudal M1 borders were estimated from current thresholds ($\geq$80 μA), distance from central sulcus, and in relation to area 3a (described next).

3.3.5 Somatosensory Mapping

We recorded multi-unit activity to map the somatotopic organization of somatosensory cortex (Fig. 3.1C-D). A tungsten or a platinum/iridium microelectrode (125 μm shaft, 420 kΩ median impedance) was lowered to layer IV (700-800 μm deep). Distance between sites was typically <1 mm. Signal was amplified (10,000x) and filtered (bandpass 300-5000 Hz, notch 60 Hz) using an AC amplifier (Model 2800, AM Systems, Sequim, WA). The signal was then passed through a 50/60 Hz noise eliminator (HumBug, Quest Scientific Instruments Inc., Vancouver, BC) and monitored with an oscilloscope and a loudspeaker. Receptive fields were determined from neural responses to stimulation of the contralateral body. Responses were classified as cutaneous or proprioceptive. Units in areas 3b and 1 responded to cutaneous stimulation and had relatively small receptive fields (e.g., single digit phalanx). In contrast, units in area 3a were unresponsive to skin contact and responded only weakly to the manipulation of multiple joints (e.g., entire digit or multiple digits). Area 2 contained a mixture of units that responded to joint manipulation or cutaneous

stimulation. Cortical borders were estimated from transitions in receptive field properties along the rostro-caudal dimension (Sur et al., 1982). Somatosensory maps were generated with Voronoi diagrams as described above.

3.3.6 Intrinsic Signal Optical Imaging

We used intrinsic signal optical imaging (ISOI) to measure resting state (RS) and ICMS-evoked activation. Images of cortex were acquired with a camera (Photon Focus, Lachen, Switzerland) based on a 12-bit CMOS sensor (1312 x 1082 pixels). An optical imaging system (Imager 3001, Optical Imaging Ltd, Rehovot, Israel) controlled image acquisition. The tandem lens combination provided a field-of-view ($\sim$26 x 22 mm; $\sim$19 μm/pixel) that included the microelectrode mapping territory as well as 2-3 mm of skull around the perimeter. Camera angles were adjusted with a 3-axis geared head (410 Junior Geared Tripod Head, Manfrotto, Cassola, Italy). Camera position (x, y, and z directions) was translated with independent linear stages. For spatial reference, blood vessel patterns were imaged (528 nm illumination) at the start of each ISOI recording. Three independently controlled LEDs (620 nm) provided illumination during ISOI.

3.3.7 Resting State

3.3.7.1 Image Acquisition and Processing. Spontaneous cortical activity was recorded with ISOI for 15 minutes. Frames were temporally binned to 10 Hz. The raw time course and power spectrum for the entire field-of-view (FOV) was examined for initial assessment of image quality. Segments of data were excluded if there was evidence of artifact, which was typically due to illumination instability, animal state fluctuations, or setup vibrations. The remaining frames were spatially binned by a factor of 3 (from $\sim$19 μm/pixel to $\sim$58 μm/pixel).

Image processing was conducted in both the temporal and spatial domains using MATLAB scripts. (1) Frames were temporally binned from 10 Hz to 2 Hz for de-noising and to speed up computation in subsequent steps. (2) A moving median filter (2 s window) smoothed the time course of each pixel to minimize noise. (3) First-frame subtraction con-

verted pixel values to reflectance change (ΔR/R%) from baseline. (4) A high-pass filter (Butterworth, 3^{rd} order, cutoff 0.005 Hz) was applied to each pixel to minimize the effects of illumination drift. (5) Multiple linear regression was used to remove nuisance signals from the time course of each pixel. This step minimized the effects of global signals, blood vessel activity, and residual artifact. The most effective regressors were groups of pixels that overlapped the skull or major blood vessels. To identify those pixels, principal component analysis (PCA) and k-means clustering were iteratively applied until we accounted for 85-90% of the variance in pixel values overlapping skull and blood vessels. This was achieved with 5-6 clusters of pixels over the skull and 5-6 clusters of pixels over major blood vessels. For each cluster, the average time course of all pixels was used as a regressor in the multiple linear regression. The average time course for all visible cortex was used as an additional regressor, which is similar to global signal regression in RS-fMRI (Murphy and Fox, 2017). (6) Frames were then spatially filtered for smoothing (gaussian kernel = 2 pixels or 120 μm radius). (7) Each time course was bandpass filtered (Butterworth, 3^{rd} order, 0.01-0.1 Hz) to hone in on infra-slow signals (Cordes et al., 2001). The effects of each processing step are shown for representative sites (Fig. 3.8).

3.3.7.2 Functional Connectivity Maps. Functional connectivity (FC) was measured from seeds in individual ISOI recordings. A seed (radius = 4 pixels, $\sim$232 μm) was defined as a cluster of pixels. The time courses of those pixels were averaged with weighting towards the center (Gaussian, sigma = 0.5) to generate one time course for the seed. The seed time course was correlated (Pearson) with time courses of all other pixels. Coefficients were then regressed as a function of distance from the seed to correct for the effect of distance on correlation strength. Pixels were color coded according to coefficient values to generate an FC map. This process was repeated for every seed available in the FOV and for every ISOI recording (Table 3.1). FC maps from the same hemisphere and seed were co-registered (details in common reference registration) and then averaged for de-noising. Pixels were flagged if their coefficients had a distribution ¿zero (unpaired t-test, $p<0.001$). The statistical analysis was applied only to pixels that were present in $\geq$10 recordings. Average FC maps were thresholded by excluding non-flagged pixels.

3.3.7.3 ICMS-Evoked Activation

3.3.7.4 Image Acquisition and Processing. ISOI was used to measure ICMS-evoked activation from select cortical sites. Procedure details were previously described (Card and Gharbawie, 2020). A microelectrode (platinum/iridium, 125 μm shaft) was lowered 1000 μm below the cortical surface. Each site was tested on >50 blocks; one ICMS trial and one Blank trial (i.e., no ICMS) per block. Image acquisition was 4 seconds/trial followed by 12-second inter-trial interval. Frames were temporally binned to 5 Hz. The stimulation train consisted of 150 biphasic pulses, 0.2 ms phase width, 300 Hz pulse frequency, and 60 μA current amplitude. Microelectrode impedance was comparable at the start (median = 240 kΩ) and end of each experiment (median = 320 kΩ). Microstimulation parameters were based on a systematic investigation of the effects of train duration, frequency, pulse amplitude, and electrode depth on ICMS-evoked activation (figure 9 in Card and Gharbawie (2020)). With the exception of the relatively low current amplitude used here, the present microstimulation parameters were consistent with other studies that measured the ICMS response with ISOI (Stepniewska et al., 2011; Friedman et al., 2020), or with fMRI (Tolias et al., 2005; Ekstrom et al., 2008; Moeller et al., 2008; Klink et al., 2021), or from movement classification (Graziano et al., 2002; Stepniewska et al., 2005; Baldwin et al., 2017).

ISOI data was processed and analyzed using custom MATLAB scripts. Two image subtractions were applied to minimize global signals. (1) In every trial, the first data frame was subtracted from subsequent frames. (2) In every block of trials, frames of the Blank condition were subtracted from frames of the ICMS condition. Next, 2-3 data frames from ICMS minus Blank (1000-1600 ms from stimulation onset) were averaged for every trial. Those mean frames were then used for generating average subtraction maps. Maps were spatially filtered to correct uneven illumination (high-pass median filter, kernel = 250-350 pixels or 5-7 mm) and for smoothing (low-pass Gaussian filter, kernel = 10 pixels or 190 μm). To enhance contrast, the distribution of pixel values was clipped (median $\pm$1.5 SD). In the final subtraction maps, dark pixels indicated reflectance change due to oximetry modulations from local increases in neural activity. Dark pixels therefore reported ICMS-evoked activation.

3.3.7.5 Effective Connectivity Maps. Mean frames from ICMS trials were compared on a pixel-by-pixel basis to mean frames from Blank trials (paired t-test). Pixels that darkened (left tail, $p<0.001$) in response to ICMS were included in EC maps.

3.3.8 Anatomical Connectivity

3.3.8.1 Tracer Injections. Retrograde and anterograde tracers were injected in cortical sites to examine their anatomical connectivity (AC). Injections were in a subset of sites in M1, PMd, and PMv that had been investigated with ICMS+ISOI. Tracers were pressure injected using Hamilton syringes fitted with a beveled glass pipette. For each site, tracer was injected 700 μm and 1400 μm below the cortical surface. Four tracers were used: (1) Cholera toxin B subunit (CTB, SigmaMillipore). (2) Biotinylated dextran amine 1:1 mixture of 3,000 MW and 10,000 MW (BDA, ThermoFisher Scientific). (3) Dextran tetramethylrhodamine 3,000 MW, commonly known as fluoro ruby (FR, ThermoFisher Scientific). (4) Fast blue (FB, Polysciences). Total volumes were 0.4 μL for FB (2% in dH2O), 0.8 μL for FR (10% in dH2O), 0.6 μL for CTB (1% in dH2O), and 0.8-1.5 μL for BDA (10% in dH2O). After 12-13 days of tracer transport, a terminal experiment was conducted for additional ISOI recordings and microelectrode mapping. Also, microlesions were made (5 μA DC) to create salient landmarks for co-registering histological sections, ISOI maps, and microelectrode maps.

3.3.8.2 Histology. After a lethal dose of sodium pentobarbital (Fatal Plus, Vortech), intracardial perfusion proceeded with PBS (pH 7.4), followed by 2% paraformaldehyde in PBS, and then 2% paraformaldehyde in PBS with 10% sucrose solution. Cortex was separated, flattened, and blocked >5 mm beyond the imaging FOV. Two glass slides held the cortex flat during fixation (4% paraformaldehyde, ∼24 hours) and cryoprotection (30% sucrose, ∼48 hours). Cortex was then cut parallel to the surface and sections (50 μm) were stored in series. One series was reacted in a nickel-intensified DAB (diaminobenzidine dihydrochloride) to visualize BDA labelling. A separate series was reacted for CTB immunohistochemistry and labeled cells were visualized with a nickel-intensified DAB reaction (Bruce and Grofova,

1992). A DAB and alkaline phosphate reaction was carried out in the same series to visualize BDA labelling. A third series was mounted onto slides without processing for examination of fluorescent labelling.

3.3.8.3 Section Plotting. Sections were examined with a microscope (Eclipse E600, Nikon, Minato City, Tokyo, Japan) outfitted with a motorized stage and x,y encoder (MAC5000 PS-SYSTEM 73005020, Ludl Electronic Products, Hawthorne, NY). FR-labelled cells were visualized with fluorescence illumination passed through a TRITC HYQ filter (excitation: 530-560 nm, emission: 590-650 nm) and FB-labelled cells with a UV-2E/C filter (excitation: 340-380 nm, emission: 435-485 nm). BDA-labelled and CTB-labelled cells were visualized with bright-field illumination. Cells and landmarks (microlesions, injection sites, sulci, blood vessels, tissue artifacts) were plotted using Neurolucida software (version 6.0, MBF Bioscience). For each injection, cells were plotted from 4-8 sections (¿200 μm between sections).

3.3.8.4 Anatomical Connectivity Maps. Neurolucida files were converted into DXF format (AutoCAD version 23.1, Autodesk, San Rafael, CA) with x,y coordinates for plotted cells and landmarks. DXF files were loaded into Adobe Illustrator (Version 25.3, Adobe, San Jose, CA) and then copied into Adobe Photoshop (Version 21.1.0, Adobe, San Jose, CA). Sections from the same injection were co-registered then labelled cells were counted in circular bins (diameter 10-20 pixels, 190-380 μm). Bin diameter increased with distance from the injection site ($\sim$8 μm/mm) as a correction step that approximates the distance regression applied in FC maps. Cell counts were summed across corresponding bins and collated into a single section. The value at each bin was expressed as a percentage of the total number of labeled cells to generate an anatomical connectivity (AC) map.

3.3.9 Common Reference Registration

The common reference for each hemisphere was a high-resolution, high-contrast image of the cortical blood vessels. Microelectrode penetrations, microlesions, and tracer injections

were marked on that image. ISOI frames were co-registered to the common reference using non-linear bicubic transformation for 300-600 points. Co-registration was conducted with a custom MATLAB script and a script from the MATLAB file exchange [B-spline Grid, Image and Point based Registration, Dirk-Jan Kroon, 2021]. Histological sections were co-registered to the common reference using the same approach and the Puppet Warp feature in Adobe Photoshop (Version 21.1.0, Adobe, San Jose, CA).

3.3.10 Statistical Analyses

Statistical tests were performed using SPSS and MATLAB. Parametric tests were used wherever assumptions about the distribution were satisfied (e.g., normality and homoscedasticity). Normality was tested using the Kolmogorov–Smirnov test and homoscedasticity was tested using Levene's test. Non-parametric tests were used if assumptions were not satisfied. For one- or two-sample comparisons, either a t-test or a Wilcoxon rank-sum test was performed. For comparisons across >2 parametric populations, a one-way ANOVA was used with a post hoc Tukey's HSD test. For comparisons across >2 non-parametric populations, a Kruskal-Wallis test was performed with a post hoc Dunn's test. For all tests, a significance level of $\alpha = 0.05$ was used. Bonferroni correction was applied where appropriate. Significance conventions in figures: *p<0.05, **p<0.01, ***p<0.001.

3.4 Results

We recorded resting state with intrinsic signal optical imaging (RS-ISOI) and compared the functional connectivity (FC) against well-established benchmarks of cortical architecture. RS-ISOI was recorded in monthly experiments conducted over ∼1.5 years (e.g., **video 1**). Our testbed was the squirrel monkey sensorimotor cortex where we could rely on microelectrode mapping for comprehensive cortical parcellation. We generated functional connectivity (FC) maps for seeds throughout the FOV. In the same sites, we also mapped (1) effective

connectivity (EC) using intracortical microstimulation + ISOI and (2) anatomical connectivity (AC) using tracer injections. Quantitative comparisons showed excellent correspondence between FC maps, EC maps, and AC maps.

3.4.1 Consistent Cortical Parcellation with Microelectrode Mapping

We used high density microelectrode mapping (<1 mm between sites) to define cortical borders and somatotopy in motor and somatosensory cortex. The somatotopy of motor (Fig. 3.1A-B) and somatosensory (Fig. 3.1C-D) maps was consistent between monkeys and followed a medial-lateral organization (leg to face) that is well-established for New World monkeys (Welker et al., 1957; Merzenich et al., 1978; Gould et al., 1986; Padberg et al., 2005; Mayer et al., 2019). Criteria for estimating cortical borders included current thresholds, receptive field properties, and distance to central sulcus.

The forelimb representation occupied most of the motor territory. Within the M1 forelimb representation, hand zones (digit and wrist) were surrounded by arm zones (elbow and shoulder), which is consistent with previous work (Dancause et al., 2008; Card and Gharbawie, 2020). PMv and PMd contained independent hand zones (Fig. 3.1A-B) and the PMd hand zone was surrounded by an arm zone. Motor and somatosensory maps were merged into a single map (Fig. 3.1E-F). We used the amalgamated maps to parcellate cortex, place seeds, and quantify connectivity maps. The size of the responsive cortical territory was similar between animals (monkey R = 236.7 mm^2 & monkey B = 221.4 mm^2). Zones in the middle of the map (i.e., hand, arm, and trunk zones) were consistent in size between animals, whereas zones on the perimeter (i.e., leg, tail, face) were more variable (Fig. 3.1H). Discrepancy between middle and perimeter was likely related to the extent of microelectrode mapping as opposed to differences between animals.

To assess map stability, a subset of sites was retested months after initial classification. Each retest occurred <250 μm from the original site. Most of the retested motor sites (32/37 sites, 86.5%) had the same classification at both time points (267 $\pm$ 151 days apart, 193 $\pm$ 55 μm apart, mean $\pm$ SD). Similarly, most of the retested somatosensory sites (12/14 sites,

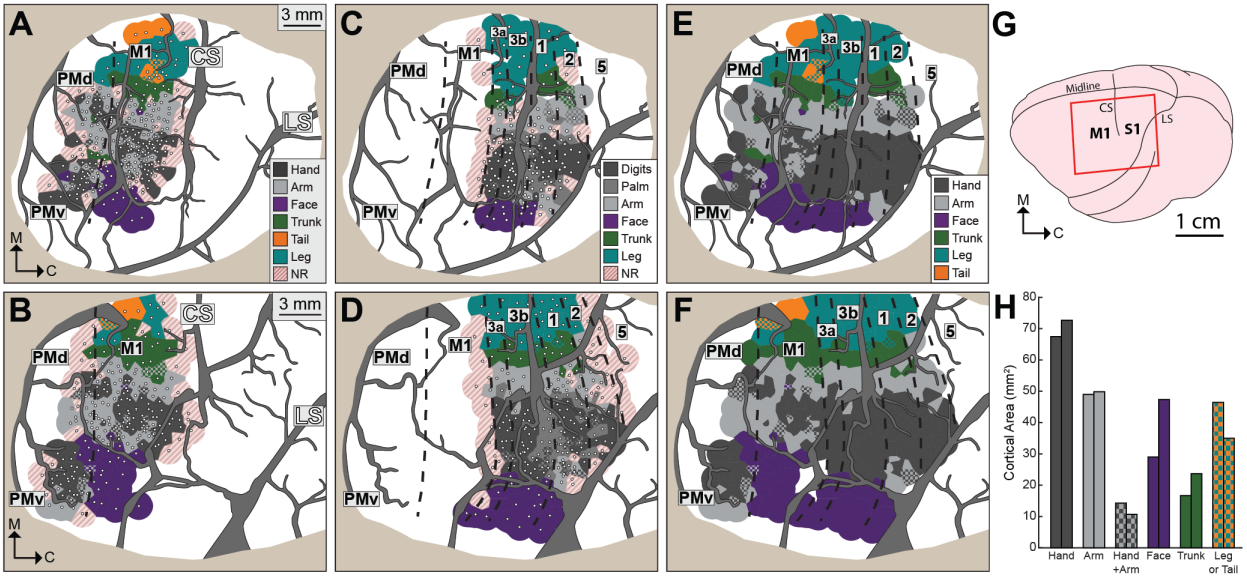

Figure 3.1: Motor and somatosensory maps are consistent between animals. (A) Motor maps for M1, PMd, and PMv from the left hemisphere (monkey B). White dots are intracortical microstimulation sites (ICMS, n = 264). Voronoi tiles (1.0 mm radius) are color-coded according to ICMS-evoked movement. Checkered tiles depict multiple movements (1 color/body part). Non-responsive sites (NR) failed to evoke movements at 150 μA. The forelimb representation (gray tones) was mapped up to its borders. Face, leg, and tail representations were mapped less extensively. The rostral M1 border (dashed line) was estimated from current thresholds and distance to central sulcus (CS). Major vessels are masked in gray. LS: lateral sulcus. Tan color in the perimeter masks resected dura and skull. Scale bar applies to panels in top row. (B) Motor map (n = 231 sites) from monkey R. Scale bar applies to panels in bottom row. (C) Somatosensory maps for areas 3a, 3b, 1, and 2, from the same hemisphere in (A). White dots are microelectrode recording sites (n = 169). Voronoi tiles (1.0 mm radius) are color-coded according to body part that drove unit activity most effectively. Sites were classified as NR if stimulation and joint manipulation failed to drive unit activity. Cortical borders (dashed lines) were estimated from receptive fields and distance to CS. (D) Somatosensory maps (n = 251 sites) from the same hemisphere in (B). (E) Combined maps from (A) and (C). NR sites were removed. Somatosensory sites with palm and digit responses are classified here as hand. (F) Combined maps from (B) and (D). (G) Schematic of squirrel monkey brain. Red rectangle approximates the field of view in (A-F). (H) Cortical surface areas measured from (E) and (F).

85.7%) had the same classification at both time points (189 ± 118 days apart, 195 ± 53 μm apart, mean ± SD). This sample of retested sites (5.7% of total sites) confirmed that maps were stable enough for reliable cortical parcellation.

3.4.2 Measuring Functional Connectivity from RS-ISOI

In a representative RS-ISOI recording (Video 1), we placed the seed in the PMv hand zone (Fig. 3.2A, blue circle, 232 μm radius). We targeted this zone because its connections include nearby, tightly spaced patches in M1 and PMd, as well as 1 or more distant patches in area 2. We considered this constellation of patches a high benchmark for evaluating RS-ISOI in mapping connectivity. For initial inspection of the site, signals were processed in the spatial and temporal domains (Fig. 3.2B top vs bottom; Fig. 3.8). Then we flagged frames in which reflectance change at the seed darkened >1.5 SD beyond the mean value of the time course (Fig. 3.2B bottom, red line). Averaging flagged frames revealed dark patches in M1, PMd, 3a, 2, and at the seed in PMv (Fig. 3.2C arrowheads). The locations and sizes of the patches were consistent with cortical connections from tracer studies (Dum and Strick, 2005; Stepniewska et al., 2006; Gharbawie et al., 2011; Hamadjida et al., 2016). Thus, credible reports on cortical connectivity can be extracted from RS-ISOI time series.

To quantify co-fluctuations in the time series, we conducted pairwise correlations (Pearson) between the seed time course and the time courses of all other pixels. The map of correlation coefficients had hot spots (Fig. 3.2D) that were in the same locations as the dark patches in Fig. 3.2C. We compared time courses from 3 regions-of-interest (ROI) with the seed time course (Fig. 3.2D, colored circles). (1) Coupling between the time courses from the red ROI and the seed was confirmed with tight positive correlation (ρ = 0.67, Figs. 3.2E-F top). (2) Time courses from the orange ROI and the seed had no discernible relationship (Figs. 3.2E-F middle). (3) Time courses from the green ROI and the seed were consistently out of phase, which was confirmed with strong negative correlation (ρ = -0.53, Figs. 3.2E-F bottom). Similar observations are in Video 2.

Next, we investigated the optimal duration for recording RS-ISOI. FC quality and stability improves with imaging duration (Birn et al., 2013), but the gain is at the expense

of processing time due to computational overhead. This motivated us to find the point at which gains from imaging duration begin to diminish. To that end, we acquired RS-ISOI for 30 min in 4 separate recordings (2 recordings/animal). Each recording was segmented according to 16 different durations. For example, 30 x 1-min segments, 15 x 2-min segments, 10 x 3-min segments, etc. Seeds were then systematically placed throughout the FOV (Fig. 3.3A) to generate FC maps from each segment. Maps from equal segments were directly compared to one another (Pearson correlation). For example, a map from a 1-min segment would have been compared to 29 maps from the remaining 1-min segments. Fig. 3.2G shows representative comparisons (top vs. bottom). Correspondence between FC maps improved with segment duration, which was confirmed with higher correlation coefficients. Comparisons from all seeds and imaging runs indicated that FC maps from the 15-min segments were robust ($\rho = 0.80$, Fig. 3.2H). Correspondence between FC maps decreased ($\rho = 0.73$) in the 10-min segments, but the drop was more substantial for shorter segments ($\rho = 0.59$ at 5 min; $\rho = 0.38$ at 2 min; $\rho = 0.15$ at 0.5 min). We therefore considered 15-min the optimal duration and used it as the standard in all subsequent RS-ISOI recordings, which was consistent with previous RS-ISOI recordings (White et al., 2011; Vasireddi et al., 2016).

3.4.3 Functional Connectivity is Consistent Across Months

Our next objective was to evaluate FC map consistency across ISOI recordings (14-16 months apart). We generated FC maps for each recording from a grid of seeds (Fig. 3.3A; 1 map/seed/recording) and then conducted 3 sets of pairwise correlations (Pearson) between maps. (1) Comparisons (n = 68,062) in matched sites indicated variation in FC maps across recordings ($\rho = 0.49 \pm 0.21$). Nevertheless, after thresholding each map to coefficients $\geq$0.25 and redoing the comparisons, it was evident that FC maps were in fact consistent across recordings ($\rho = 0.80 \pm 0.13$). For reference, we found no correspondence ($\rho = 0.02 \pm 0.32$) between FC maps from non-matched sites (n = 1,483,451 comparisons). Thus, thresholded FC maps were spatially specific and consistent across months of recordings.

We reasoned from these results that averaging FC maps from the same seed could be an effective denoising step. Indeed, the effect of averaging was evident in a side-by-side

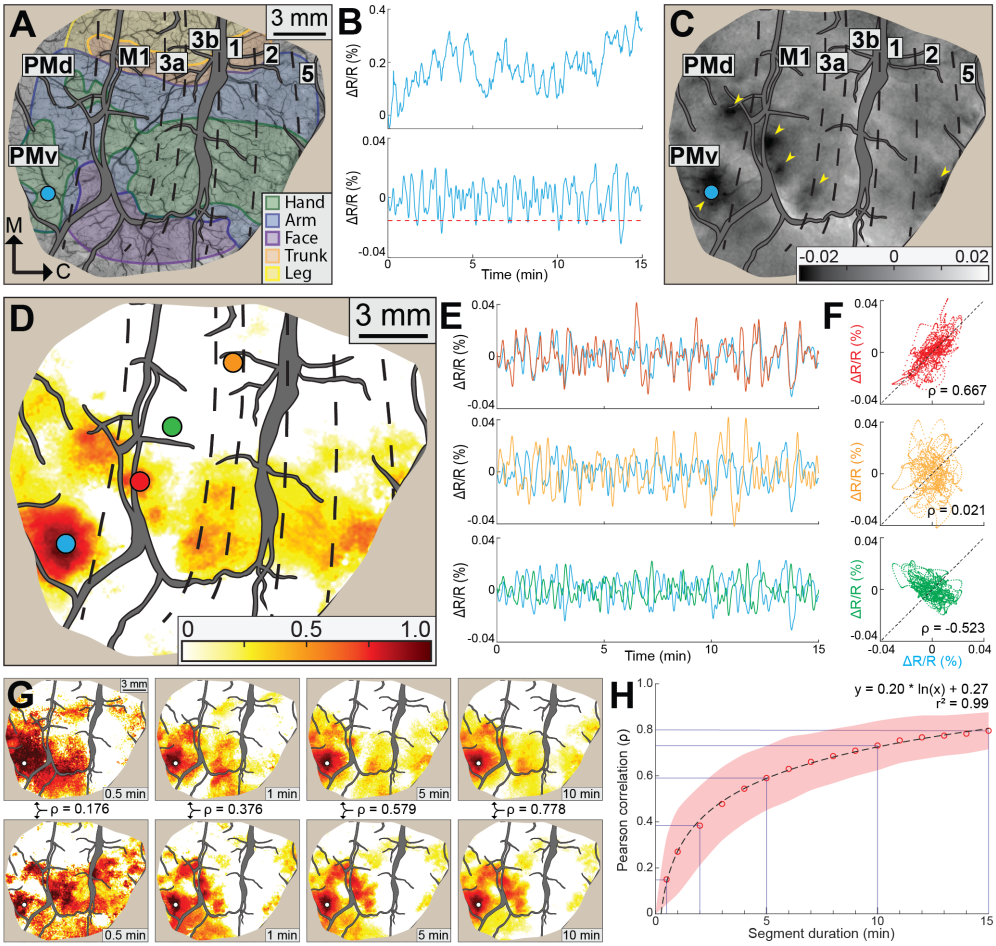

Figure 3.2: Time course correlations and optimal imaging duration. (A) Optical image of cortex (528 nm illumination) with cortical borders and zones from microelectrode maps. Large blood vessels are masked in gray. Tan color around the perimeter masks resected dura and skull. Scale bar is same for (C). Seed (blue circle) is in the PMv hand zone. (B) *Top.* Raw time course of reflectance change (ΔR/R%) measured from the seed in 1 RS-ISOI recording. *Bottom.* Same time course after spatial and temporal processing. Dashed line is threshold for flagging frames where the seed darkened. (C) Average optical image from frames flagged in (B). Dark patches (arrowheads) are evident at the seed and in PMd, M1, 3a, and area 2. (D) Functional connectivity (FC) map from same seed in (C). Color scale reflects the correlation coefficient (ρ) between the time course at a given pixel and the time course of the seed. Colored circles are representative regions-of-interest (ROIs). (E) Each plot shows time courses from the seed and 1 ROI from (D). Line color matches ROI color in (D). (F) Scatter plots show reflectance change in the seed (x-axis) against reflectance change in the ROIs (y-axis). Each plot relates to the adjacent line plot in (E). Only the red scatter plot showed positive correlation. (G) Representative FC maps generated from variable segments of a 30-min RS-ISOI recording. Segment duration is in the bottom right corner. Seed (white dot) is in the same location as (D). Coefficients (ρ) are from pairwise comparisons (Pearson correlation) between map in the top row and map directly below it. (H) Pairwise comparisons (n = 250,245 between both monkeys) of maps and coefficients from 4 RS-ISOI recordings. Red circles are average coefficients for each segment duration. Red shading is $\pm$SD. Equation and r^2 describe line of best fit.

comparison of an FC map from 1 recording and an FC map averaged from 13 recordings (Fig. 3.3B-C). Seed (white dot) location in PMv matched Fig. 3.2. Pixels with high coefficients (orange-red) were consistent in the individual and average FC maps. In contrast, pixels with low coefficients (white-yellow) occupied more territory in the individual FC map. These observations confirmed that the relatively strong features of an FC map were stable over time.

Observations from Figs. 3.3A-C motivated us to average and threshold FC maps. For thresholding, we included only pixels with coefficient distributions >zero (one-tailed t-test, $p<0.001$) in order to exclude noisy pixels and low-coefficient pixels. As expected, averaging and thresholding the map in Fig. 3.3B resulted in a cleaner iteration (Fig. 3.3D) that was also consistent between animals (Fig. 3.3E). For context, we superimposed cortical borders and shaded in the hand (green) and arm (blue) zones. In both animals, significant pixels were concentrated in hand zones and to a much lesser extent in arm zones. Only a small fraction of significant pixels was outside of the forelimb zones. Beyond the seed location in PMv, significant pixels were most concentrated in M1, 3a, and area 2. Pixels were sparse and had weaker coefficients in PMd, area 3b, and area 1. Fig. 3.3F summarizes the connectivity profiles in Figs. 3.3D-E. To simplify the plots, cortical areas were grouped by modality: (1) motor (M1, PMd, PMv), (2) somatosensory (areas 3a, 3b, 1, and 2), and (3) area 5. FC quantification relative to functional zone (e.g., motor hand) was based on the number of significant pixels and their coefficients. As expected from Figs. 3.3D-E, the polar plot showed that FC was stronger with hand zones than with arm zones. FC was also stronger with motor fields than with somatosensory fields. Finally, cosine similarity (CS, detailed below) confirmed that the FC profile for this site was consistent between animals ($CS = 0.94$).

We also tested the effects of averaging and thresholding on an FC map of a completely different profile. Seeds were placed in the representation of digit 2 in area 3b (Fig. 3.3G-H). Most significant pixels were in hand zones, which was apparent in the polar plot. Those pixels were concentrated in somatosensory areas 3b, 1, and to a lesser extent in areas 3a and 2. Beyond somatosensory cortex, significant pixels were present in M1 hand and PMv hand, but to different extents between animals. The overall distribution of significant pixels

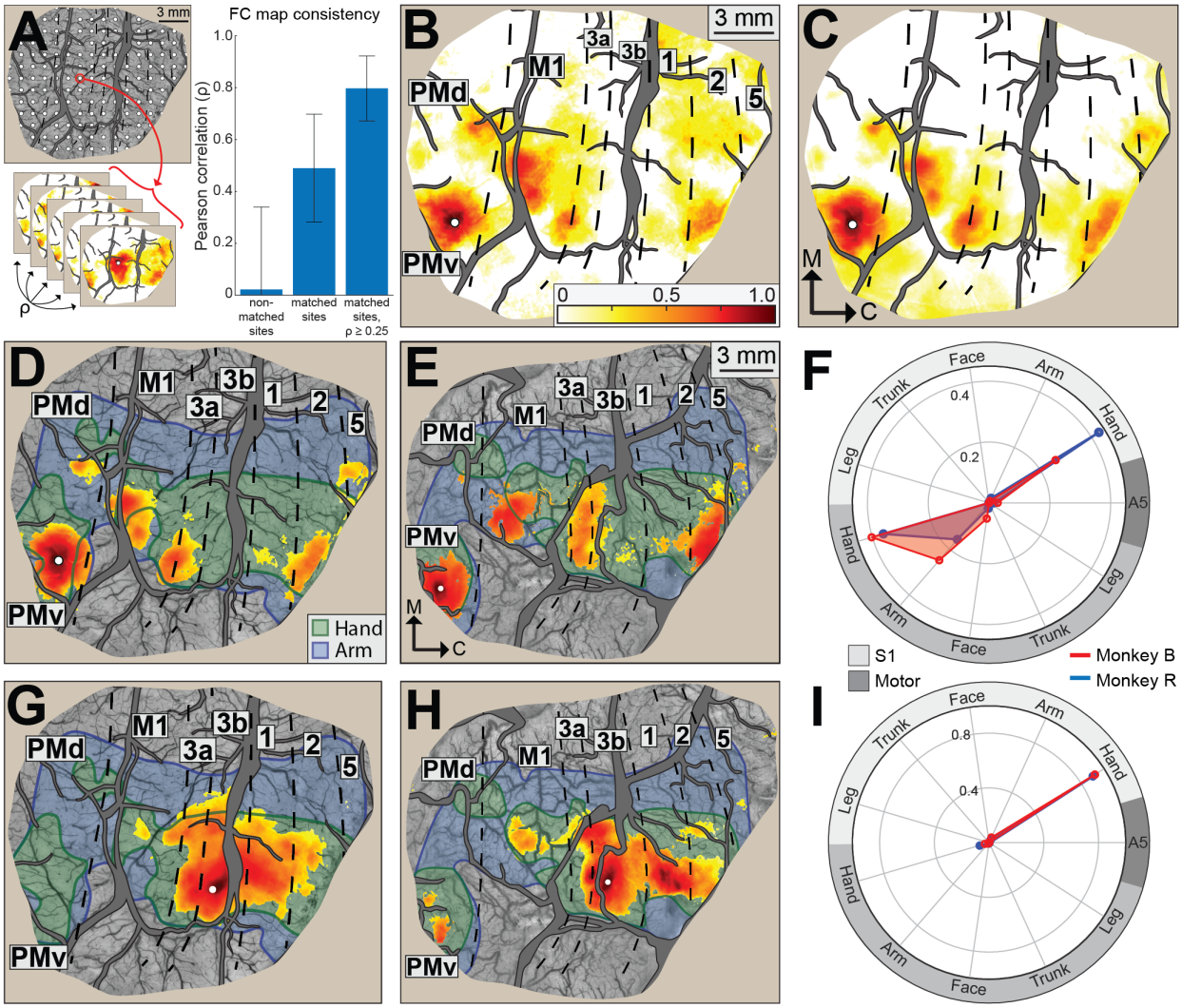

Figure 3.3: Functional connectivity maps are stable over months and consistent between monkeys. (A) Grid of seeds (n = 66-71 per hemisphere, 1 mm spacing). For every seed, FC maps were generated from imaging runs up to 16 months apart. *Bar plot.* Pairwise comparisons (Pearson correlation) of maps from each animal. Correspondence was highest for matched sites after maps were thresholded for coefficients $\geq$0.25. Correspondence declined in the absence of thresholding. There was no correspondence for comparisons between non-matched sites. (B) Functional connectivity (FC) map from a representative RS-ISOI recording (15 min) in monkey B. Seed (white dot) is in the PMv hand zone. Color bar is correlation coefficients (ρ) and applies to all panels. (C) Average FC map from 13 RS-ISOI recordings. Seed location is same as (B). Patches of hot colors are in similar locations in (B) and (C). (D) FC map is same as (C) but limited to pixels with significant coefficients (one-tailed t-test, p<0.001). (E) Average FC map for a matching seed location in monkey R. Map is based on 15 RS-ISOI recordings. (F) FC profiled in relation to motor and somatosensory maps. Quantification is based on number of pixels and coefficients for maps in (D, red plot) and (E, blue plot). Sum of radial coordinates = 1. Functional zones are grouped according to modality. Motor includes M1, PMd, and PMv. S1 includes areas 3a, 3b, 1, and 2. Area 5 is independent (darkest gray). (G-I) Same as (D-F), but for a site in area 3b digit zone.

was consistent between animals (CS = 0.99) and with previous tracer injections into digit representations in areas 3b and 1 (Liao et al., 2013; Négyessy et al., 2013). Thus, our FC maps for PMv and area 3b indicate that averaging and thresholding reveals connectivity patterns that are consistent between animals and with known anatomical connections. Averaging and thresholding were therefore implemented in all subsequent analyses.

3.4.4 Functional Connectivity Corresponds with Effective Connectivity

Our next objective was to benchmark FC against ICMS-evoked activation [i.e., effective connectivity (EC)], which was a surrogate here for stimulus-driven activity and for anatomical connectivity. ICMS afforded us control over stimulus parameters and the capacity to test many sites. We evaluated correspondence between FC and EC maps on three metrics: (1) Cosine similarity (CS) measures the extent to which both maps overlap the same functional zones. CS ranges from 0 to 1 (no similarity to perfect similarity). (2) Mean separation (MS) measures the average distance between pixels in both map. Low MS indicates high spatial coincidence between maps. (3) Goodness of fit (GOF) combines CS and MS (Eq. 3.1 & 3.2). MS is first normalized by the *maximum* separation recorded (i.e., worst) between any pair of maps i. GOF ranges from 0-1 (perfect similarity to no similarity).

$$MS_{norm,i} = \frac{MS_i}{MS_{max}} \tag{3.1}$$

$$GOF_i = \frac{1 - CS_i + MS_{norm,i}}{2} \tag{3.2}$$

We compared FC and EC maps in two representative sites (Fig. 3.4A-H). In one site (Fig. 3.4A, white dot), the stimulating microelectrode was in the same PMv location as Figs. 3.2 & 3.3. The average optical image showed that ICMS activated a main patch around the microelectrode and smaller patches in M1, PMd, and areas 3a and 2 (Fig. 3.4A, arrowheads). To generate an EC map, we flagged pixels that darkened significantly in the ICMS condition as compared to the blank condition (t-test, $p < 0.001$). Significant pixels were then ranked according to their $\Delta R/R$ values (Fig. 3.4B). The same scale was applied

to the average FC map from the same site (Fig. 3.4C). The FC map was also thresholded at several cutoffs (min p < 10-1, max p < 10-7) and we selected the one that achieved the best GOF with the EC map. Correspondence between FC and EC maps was apparent in the side-by-side comparison (Figs. 3.4B-C) and in the polar plot (Fig. 3.4D). The three metrics of overlap (CS = 0.99; MS = 0.04 mm; GOF = 0.01) showed a near-perfect fit between FC and EC maps for this site. In another site, the microelectrode was in area 1 arm zone (Fig. 3.4E, white dot). Correspondence between FC and EC was apparent in the maps (Fig. 3.4F-G) and polar plot (Fig. 3.4H). The three metrics of overlap (CS = 0.97; MS = 0.06 mm; GOF = 0.03) confirmed the fit between FC and EC maps. Thus, observations from two sites indicated that FC maps overlapped exceptionally well with EC maps.

We expanded comparisons between FC and EC maps to 48 sites across monkeys (Fig. 3.4I-J). We compared FC and EC maps from matched sites and from non-matched sites. CS values were highest (i.e., best) for matched sites and decreased with differences in site identity (Fig. 3.4K). Site pair category had an effect on CS values (Fig. 3.4K, Kruskal-Wallis test, $H(3) = 484.43$, $p < 0.001$) and pair categories differed from one another (Dunn's test, $p < 0.001$). Similarly, MS values were lowest (i.e., best) for matched pairs and increased with differences in site identity (Fig. 3.4L). Pair category had an effect on MS values (Fig. 3.4L, Kruskal-Wallis test, $H(3) = 375.38$, $p < 0.001$) and pair categories differed from one another (Dunn's test, $p < 0.001$). The effects in CS and MS were also evident in the GOF (Fig. 3.4M, Kruskal-Wallis test, $H(3) = 512.55$, $p < 0.001$). Our observations indicate that correspondence was high between FC and EC maps. Moreover, lack of overlap between maps from non-matching sites suggests that somatotopy was a governing factor of the connectivity, which is consistent with previous reports on the FC of the "somatomotor network" (Yeo et al., 2011; Thomas et al., 2021).

The main patch that surrounded each site accounted for ∼50% of significant pixels in FC and EC maps (Fig. 3.4N). This motivated us to examine whether correspondence between FC and EC maps was skewed by overlap in the main patch in both maps. We therefore excluded pixels within 2 mm of each site, which effectively removed the main patch in most sites. We then repeated the comparisons between FC and EC maps (Fig. 3.4O). Excluding the main patch had no effect on the statistical relationships observed in Fig. 3.4M, which

points to universal overlap between FC and EC maps as opposed to heavy weighting in the main patch. The results in Fig. 3.4 showed that FC maps reliably reported the spatial organization and strength of site connectivity.

3.4.5 Mapping Anatomical Connectivity with Tracer Injections

Our next objective was to benchmark FC against AC revealed with tracers. We also compared EC to AC to calibrate our assumptions about using EC as a surrogate for AC. First we review results from the tracer injections (n=5; Fig. 3.5A & 3.5G) and affiliate AC maps. M1 (n = 2) and PMd (n = 2) injections were in arm zones and were in similar locations in both animals. The PMv injection was in the hand zone. After tracer transport, cortex was flattened and cut tangentially to facilitate co-registration with the common reference. Injection sites were apparent from tissue artifact and tracer uptake (e.g., Fig. 3.5B). For every section, the locations of labelled cells (e.g., Fig. 3.5C) and landmarks were plotted. Sections were collated (e.g., Fig. 3.5D, n = 8 sections) then converted into a heat map (Fig. 3.5E), which is considered the AC map. For a BDA injection in caudal M1, the AC map showed that most labeled cells were concentrated in M1 followed by areas 3a, 1, 2, and PMd (Fig. 3.5E). Most labeled cells were in arm zones (blue shade). Cells in hand zones were primarily in M1. Quantification of the heat map indicated that >60% of labeled cells were in arm zones and only ∼20% of labeled cells were in hand zones (Fig. 3.5F). This connectivity profile was confirmed in the second animal with a FR injection into the M1 arm zone (Fig. 3.5H-I). The higher proportion of cells labeled in trunk zones was likely due to the relatively medial location of the present injection as compared to the first M1 injection (Fig. 3.5A).

Connectivity profiles for PMd and PMv were distinct from those of M1. For example, CTB injection in PMd (Fig. 3.5G) labeled cells in PMd, M1, and PMv (Fig. 3.5J). Somatosensory areas 3a and 3b were almost devoid of labeled cells, but areas 1 and 2 contained small patches of labeled cells. More labeled cells were in area 5 than in anterior parietal cortex. Cells in motor areas were distributed equally between arm and hand zones (Fig. 3.5K). In contrast, cells in parietal cortex were in arm zones only. This connectivity profile was confirmed in the second animal (Fig. 3.5A, FB). The main difference was that

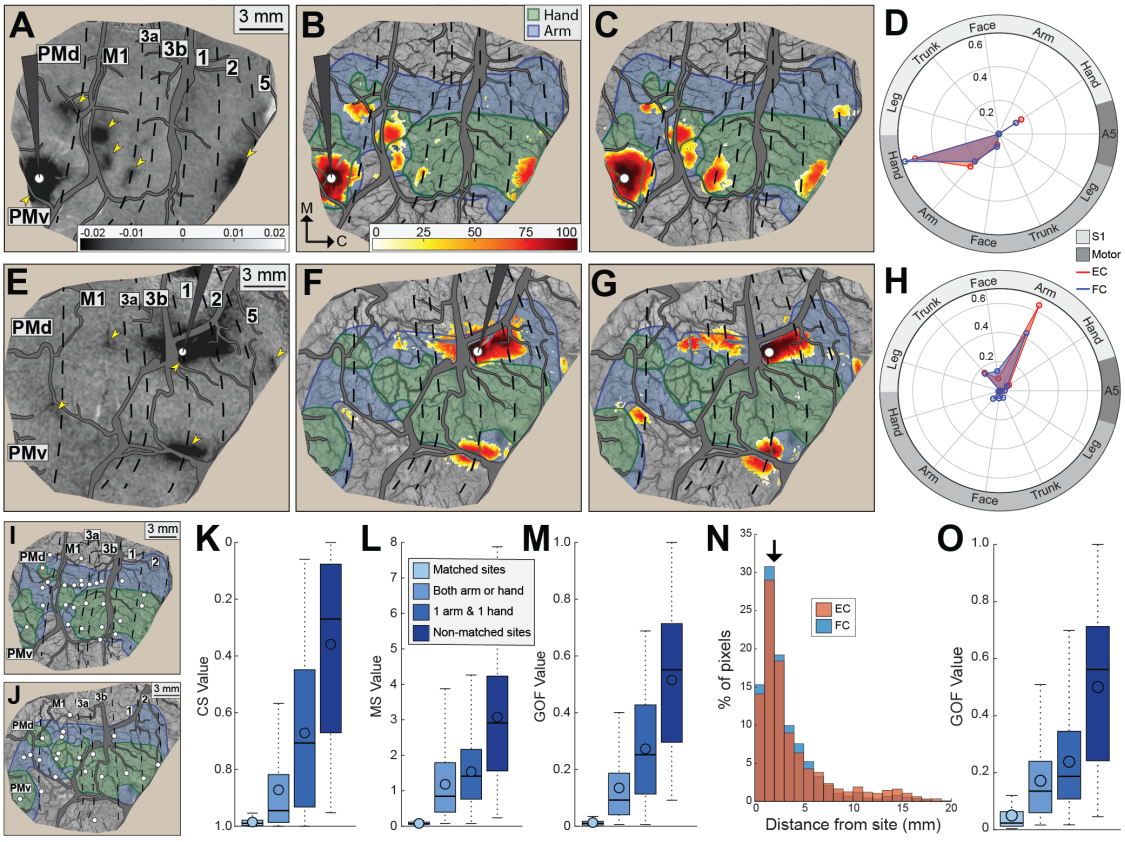

Figure 3.4: Functional connectivity maps correspond with effective connectivity maps. (A-D) Direct comparison of FC and EC maps from a site in the PMv hand zone (monkey B). (A) Average optical image: ICMS condition minus blank condition (50 trials/condition). Arrowheads point to dark patches evoked from ICMS. Stimulating microelectrode and major vessels are masked in gray. Microelectrode tip (white circle) was 1000 μm deep. (B) EC map: pixels that darkened (t-test, $p<0.001$) in response to ICMS were ranked from lowest (white = zero percentile) to highest (dark red = 100th percentile). (C) FC map for the same site in (A-B). Pixels with significant coefficients were percentile ranked as in (B). (D) Quantitative profile of FC (blue plot) and EC (red plot) maps in relation to motor and somatosensory maps. Near perfect overlap between maps was confirmed with cosine similarity (0.99). (E-H) Same as (A-D), but for a site in area 1 arm zone. Correspondence between maps was confirmed with cosine similarity (0.97). (I) Sites (n = 27) for direct comparison of FC and EC maps (monkey B). (J) Same as (I), but in monkey R (n = 21 sites). (K) Cosine similarity for pairwise comparisons between FC and EC maps. Comparisons were grouped according to site identity. (1) *Matched sites.* FC and EC maps were generated from identical locations. (2) *Both arm or hand.* FC and EC were generated from sites within the same forelimb zone (e.g., hand), but from different locations. (3) *1 arm & 1 hand.* FC and EC maps were generated from non-matched forelimb zones. (4) *Non-matched sites.* FC and EC maps were generated from non-matched representations of the body (e.g., 1 site in a forelimb zone and other site in face). (L) Mean separation between pixels for the same comparisons in (K). (M) Goodness of fit (GOF) for the same comparisons in (K). (N) Distribution of significant pixels in FC and EC maps as a function of distance from the 48 sites in (I-J). In FC and EC maps, ~50% of significant pixels were within 2 mm of the test site. (O) Same as (M) but after excluding significant pixels within 2 mm of each test site.

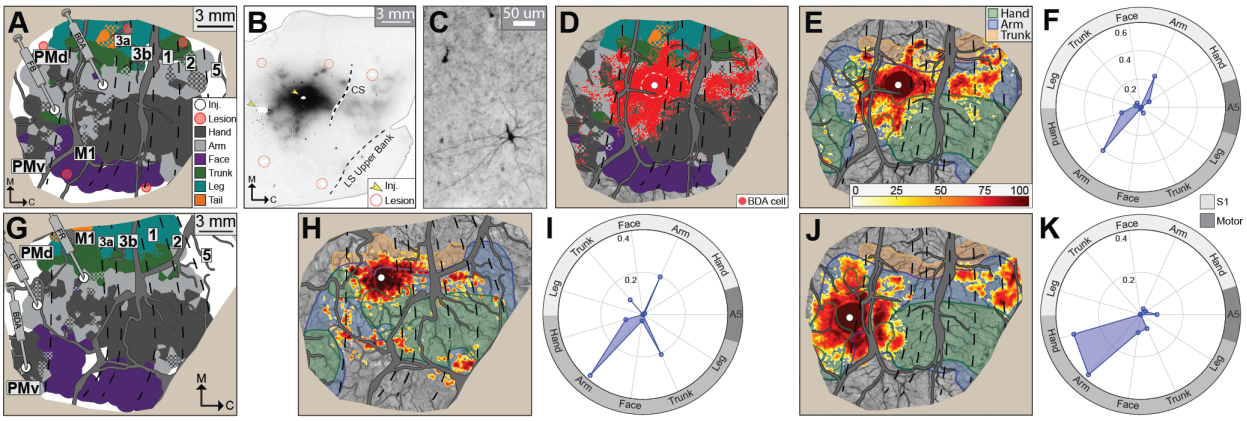

Figure 3.5: Anatomical connectivity maps from tracer injections. (A) Tracer injections (white dots) in M1 arm and PMd arm zones in monkey B. Red circles are microlesion sites. (B) Representative cortical section processed for BDA (horizontal plane, 50 μm thickness). Dark patches are labeled cells and axons. Section was cropped to the approximate field-of-view in (A). Arrowheads mark injection sites. CS: central sulcus; LS: lateral sulcus. (C) Representative BDA-labelled cell. (D) BDA-labelled cells (red circles, n=12,136) collated from 8 horizontal sections. White dot marks BDA injection site. Dashed circle marks zone of dense tracer uptake that has been filled with red. (E) Anatomical connectivity (AC) map based on the BDA-labelled cells in (D). Cells were counted from circular bins (80 μm radius) that increased by 10 μm with every millimeter from the injection site. Bins with fewer than 2 cells were omitted for de-noising. Colors indicate rank percentile from lowest (white = zero percentile) to highest (dark red = 100th percentile). Zone of dense tracer uptake is filled with the 90th percentile color. (F) Quantitative profile of (E) in relation to motor and somatosensory maps. (G) Tracer injections in M1 arm, PMd arm, and PMv hand in monkey R. (H) AC map from injection into the M1 arm zone in monkey R (6 sections, 2,832 FR-labelled cells). (I) Quantitative profile of (H). (J) AC map from injection into the PMd arm zone in monkey B (4 sections, 32,296 FB-labelled cells). (K) Quantitative profile of (J).

the second injection (Fig. 3.6A-B) labeled more cells in area 3a and fewer cells in areas 1 and 2. Finally, BDA injection in PMv (Fig. 3.5G) labeled cells in PMv, M1, and PMd (Fig. 3.6G-H). Cells in parietal cortex were in areas 3a, 2, and 5. Overall, most cells were in hand zones. M1 contained the smaller proportion of cells that were in arm zones. The connectivity profiles observed here for M1, PMd and PMv were consistent with previous observations in New World monkeys (Dum and Strick, 2005; Dancause et al., 2006a,b; Stepniewska et al., 2006; Gharbawie et al., 2011). The present AC maps are therefore reliable benchmarks for comparing FC and EC maps.

3.4.6 Functional and Effective Connectivity Correspond with Anatomical Connectivity

For each tracer injection site, we compared FC and EC maps with AC maps. In two representative sites (Fig. 3.6A-L), correspondence was evident between the three maps and polar plots. The three overlap metrics indicated high correspondence between FC and AC maps from matched sites (Fig. 3.6M). For reference, the same metrics indicated poor overlap between FC maps and AC maps from non-matched sites (Fig. 3.6M). A two-sample t-test confirmed that overlap values were better for matched pairs than for non-matched pairs; CS: $t(11) = -4.62$, $p < 0.001$; MS: $t(11) = 3.92$, $p < 0.001$; GOF: $t(11) = 4.52$, $p < 0.001$. Similarly, overlap metrics for EC and AC maps were better for matched sites than for non-matched sites (Fig. 6N; CS: $t(11) = -5.04$, $p<0.001$; MS: $t(11) = 4.98$, $p<0.001$; GOF: $t(11) = 5.37$, $p<0.001$). Thus, Fig. 3.6 shows that RS-ISOI and ICMS+ISOI both reveal cortical connectivity with the same reliability and accuracy as tracer injections.

3.4.7 Animal State Affects Functional Connectivity

FC is successfully mapped under anesthesia (Vincent et al., 2007; Mohajerani et al., 2010; Wang et al., 2013; Hutchison et al., 2014; Hori et al., 2020a). However, FC quality is susceptible to sedation depth (Liu et al., 2013c,a,b; Hutchison et al., 2014; Hori et al., 2020b). This motivated us to investigate the relationship between animal state as determined from intracranial EEG patterns and FC quality. To that end, we adjusted the isoflurane dosage

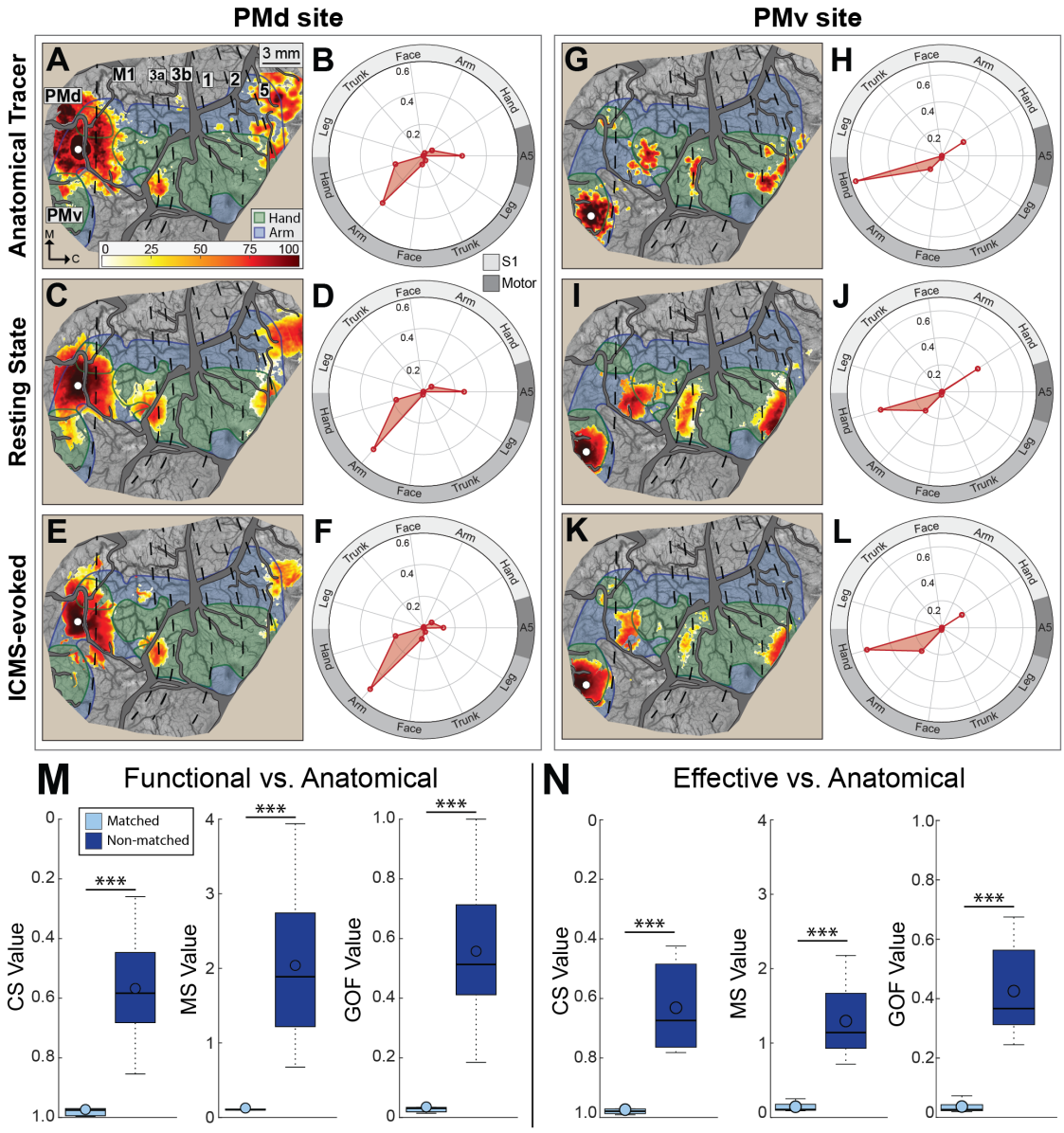

Figure 3.6: Functional and effective connectivity maps correspond with anatomical connectivity maps. (A-F) Comparison of FC, EC, and AC maps for a site in the PMd arm zone (monkey R). Conventions are consistent with Figs. 3.4 & 3.5. Color bar applies to all maps. Note similarities between the 3 maps and the 3 polar plots. (A-B) AC map and corresponding quantitative profile (5 sections, 50,020 CTB-labelled cells). (C-D) FC map and quantitative profile. (E-F) EC map and quantitative profile. (G-L) Same as (A-F), but for a site in the PMv hand zone. Note similarities between the 3 maps and the 3 polar plots. AC map in (G) was based on 6 sections, 1878 BDA-labelled cells. (M) Cosine similarity (CS), mean separation (MS), and goodness of fit (GOF) for pairwise comparisons of FC maps and AC maps from matched (light blue) and non-matched (dark blue) sites. Matched comparisons showed more correspondence between FC and AC maps than non-matched comparisons. (N) Matched comparisons showed more correspondence between EC and AC maps than non-matched comparisons.

to achieve 3 distinct states for RS-ISOI recordings. Each state was examined in >3 RS-ISOI recordings (Table 3.2). The average power spectrum from EEG recordings under deep sedation indicated that power was attenuated across frequencies (Fig. 3.7B). In contrast, the power spectrum from semi-deep sedation was shifted just below the power spectrum from light sedation. Examination of the time series showed that the burst phase in semi-deep sedation had a comparable power spectrum to light sedation. Thus, periodic suppression drove the downward shift observed in the power spectrum from semi-deep sedation (Fig. 3.7B).

The relationship between sedation depth and FC is illustrated for two representative sites (Fig. 3.7C-H). Sedation depths were tested in successive recordings in the same experiment. In *light sedation*, FC maps had well-defined patches of high correlations (Fig. 3.7C & 3.7F). Seed placement in the M1 arm zone (Fig. 3.7C) revealed an FC map that was consistent with the AC map that we reported in Fig. 3.5E and with previous work (Stepniewska et al., 1993). Similarly, the FC map that we generated for the area 3b digit zone was consistent with the connection patterns of single digit representations (Liao et al., 2013; Négyessy et al., 2013). FC map quality degraded in the other states. In *semi-deep sedation*, patches were less intense and some disappeared altogether (Fig. 3.7D & 3.7G). Nevertheless, the overall patterns were recognizable as weaker versions of Figs. 3.7C & 3.7F. In *deep sedation*, distant patches disappeared completely and FC maps were unrecognizable (Fig. 3.7E & 3.7H). Decay in map quality was transient as the original FC patterns were restored once EEG readings indicated return to light sedation. To formalize the relationship between animal state and FC map quality, we quantified correspondence between FC and AC maps at the 5 tracer sites (Fig. 3.7I). For the light sedation, low GOF values and a tight distribution confirmed that those FC maps corresponded well with AC maps. Larger GOF values and wider distributions in the other two states indicated lower correspondence between FC maps and AC maps. These observations motivated us to record RS-ISOI under light sedation, defined by the absence of EEG suppression, throughout the study. We note that light sedation was achieved with 0.9-1.5% isoflurane in the 9 recordings in this experiment (Table 3.2). But isoflurane doseing needed to be as low as 0.5% if we consider all 28 recordings from the same state (Table 3.1).

This experiment also shed light on parameters for monitoring sedation depth. For example, we found no relationship between isoflurane dose and heart rate ($r^2 = 0.09$, Fig. 7J left) and no relationship between heart rate and map quality ($r^2 = 0.01$, Fig. 3.7K left). In contrast we found a strong relationship between isoflurane dose and EEG suppression ($r^2 = 0.68$, Fig. 3.7J right) and between EEG suppression and map quality ($r^2 = 0.58$, Fig. 3.7K right).

Table 3.2: Animal state monitoring[a]

Animal state	Resting State Recordings	EEG % Suppression	% Isoflurane	Heart Rate (BPM)
Light	9	0.37 ± 0.51	1.13 ± 0.21	227.11 ± 43.68
Semi-deep	4	35.78 ± 28.87	1.91 ± 0.12	221.30 ± 33.07
Deep	3	98.73 ± 2.12	2.08 ± 0.14	220.80 ± 44.18

a. All values are mean ± SD. EEG recorded continuously, isoflurane and heart rate (HR) logged at regular intervals.

3.5 Discussion

We investigated whether resting state (RS) can reveal granular details of cortical architecture. To that end, we recorded RS with intrinsic signal optical imaging (RS-ISOI) in anesthetized squirrel monkeys. Then we correlated the infra slow signals (0.01-0.1 Hz) to infer functional connectivity (FC) for seeds throughout motor and somatosensory cortex. FC was benchmarked against (1) effective connectivity and (2) anatomical connectivity. High correspondence between the three connectivity modalities showed that spatio-temporal patterns embedded in RS time series, faithfully report cortical connectivity at columnar resolution.

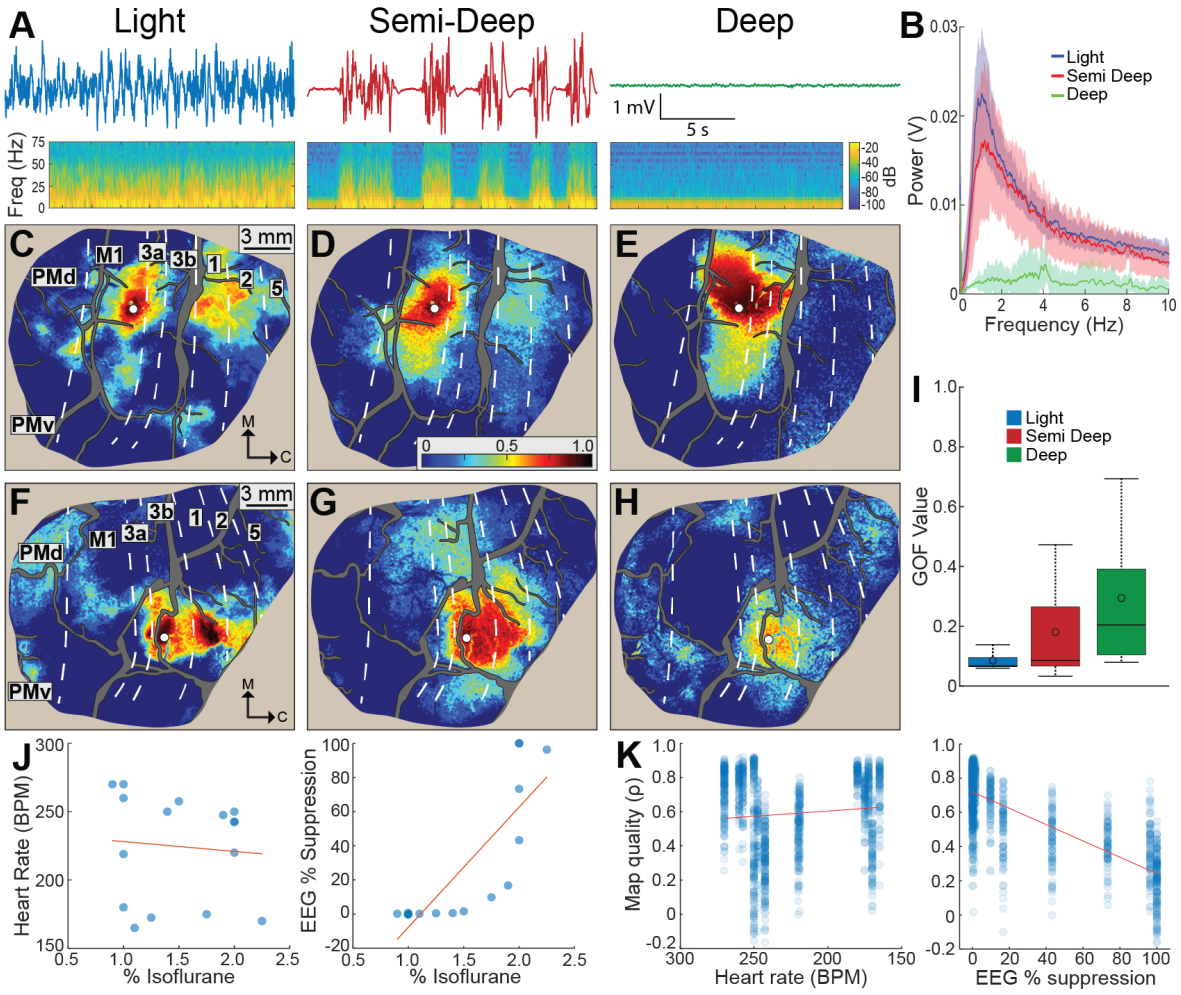

Figure 3.7: Relationship between animal state and FC map quality. (A) Representative EEG traces (top) and corresponding spectrograms (bottom) for 3 animal states. The *light state* consisted of slow waveforms and no suppression (0.9-1.5% isoflurane). The *semi-deep state* had periodic suppression (1.75-2.0% isoflurane). The *deep state* had suppression only (2.0-2.25% isoflurane). (B) Power spectrum (mean±SD) of EEG acquired during 16 RS-ISOI recordings (light n=9, semi-deep n=4, deep n=3). (C-E) FC maps from one seed (white circle) in the M1 arm zone (monkey B). FC maps match the animal state directly above in (A). Note the deterioration in spatial patterns from light to deep. (F-H) Same as (C-E), but for a seed in area 3b digit zone (monkey R). (I) Goodness of fit (GOF) between FC and AC maps at the 5 tracer sites. GOF was lowest (best) in the light state. (J) Heart rate (left) and EEG suppression (right) as a function of isoflurane dose. Each point is an average from a 15-min recording. Red line is linear fit. (K) FC map quality as a function of heart rate (left) and EEG suppression (right). Map quality is the correlation coefficient (Pearson) from comparing individual FC maps with average FC maps from the same seeds. Comparisons were conducted in seeds throughout the field-of-view (n=83-85 seeds per hemisphere).

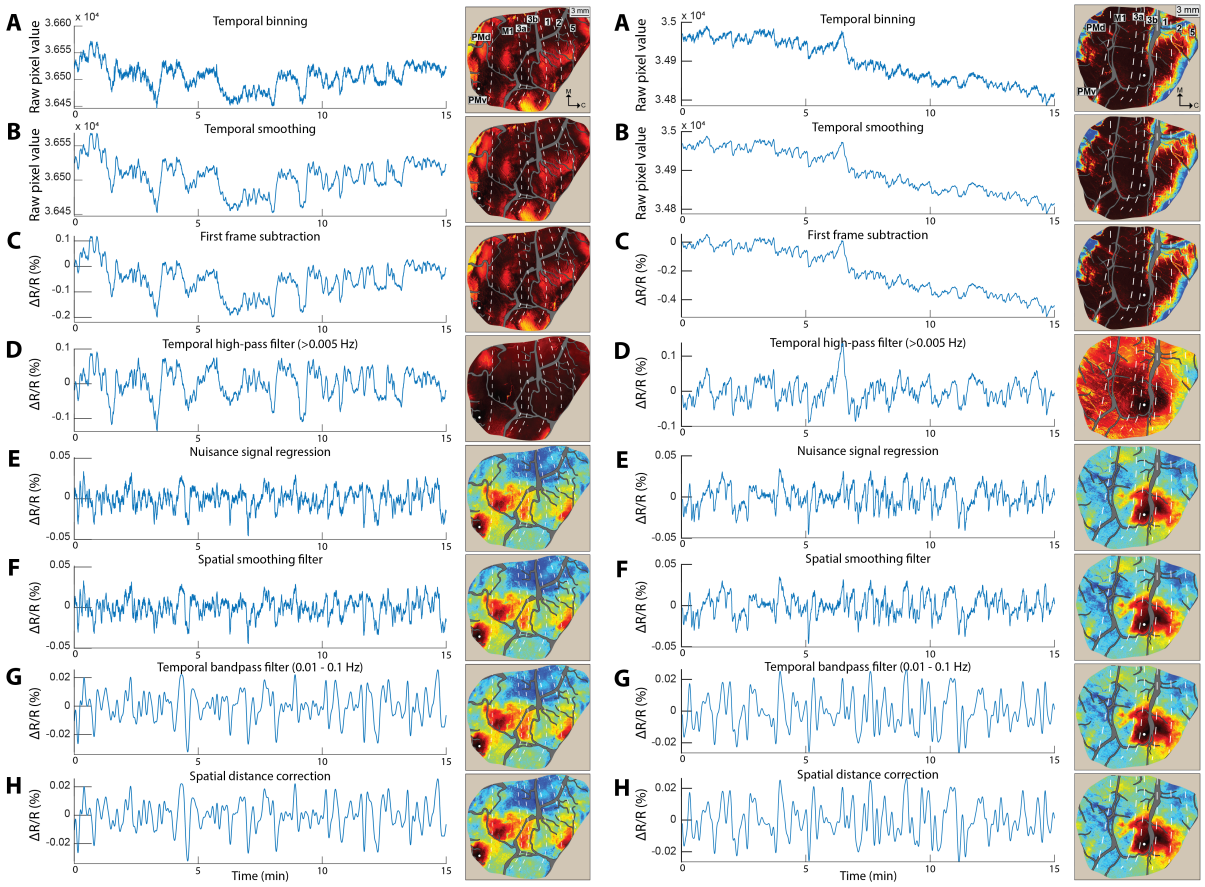

Figure 3.8: Impact of image processing steps on FC. (A-H) Seed time course (left) and corresponding FC map (right) at each image processing step (see methods) applied to an RS-ISOI recording. Seed (white dot) is in the PMv hand zone (monkey R, left) or 3b hand zone (monkey B, right). (A) Raw data after frame binning from 10 Hz to 2 Hz. (B) Time course after filtering with a moving median (2 s window). (C) First-frame subtraction converted raw pixel values to reflectance change (ΔR/R%). (D) High pass filter (Butterworth, 3rd order, cutoff 0.005 Hz) in the temporal domain removed slow drifts. (E) Multiple linear regression of nuisance and global signals attenuated the magnitude of the slowest signals and led a visible improvement in the spatial specificity of the FC map. (F) Low-pass filter (gaussian kernel = 2 pixels or 120 μm radius) applied in the spatial domain for smoothing the FC map. (G) Band-pass filter (Butterworth, 3rd order, 0.01-0.1 Hz) applied in the temporal domain to extract infra-slow signals. (H) Coefficient values in the FC map were regressed as a function of distance. The effect of this step was limited in the present example.

3.5.1 High Resolution FC

RS is typically recorded with fMRI (RS-fMRI, Biswal et al. (1995)). The approach is invaluable for insight about the macro-organization of brain networks (Fox and Raichle, 2007; Bullmore and Sporns, 2009). However, it lacks the contrast and spatial resolution needed for revealing fine network features. ISOI shares many of the operational principles of fMRI, but provides higher effective resolution. For example, ISOI typically reports stimulus-evoked activity at columnar scale (Bonhoeffer and Grinvald, 1991; Sheth et al., 2004; Lu and Roe, 2008). Here, we showed that this high effective resolution is conserved in the cortical architecture extracted from RS-ISOI. Even after down sampling, our RS-ISOI data (60 μm/pixel) still had considerably higher spatial resolution (>10x) and higher contrast than available in most RS-fMRI paradigms. Our findings extend previous RS-ISOI reports (White et al., 2011; Vazquez et al., 2014; Vasireddi et al., 2016; Bauer et al., 2018; Kura et al., 2018) by showing that the approach is effective in monkeys and reveals cortical connectivity at columnar resolution.

Among the strengths of ISOI is that it does not require extrinsic indicators. This feature is particularly useful for imaging large brains (e.g., monkeys). Indicators such as voltage sensitive dyes and GCaMP are used in RS recordings and provide better fidelity to neural activity than ISOI (Arieli et al., 1995; Mohajerani et al., 2013; Chan et al., 2015). But the temporal resolution gain does not necessarily improve the quality of FC for two reasons. First, FC quality is most robust in infra-slow signals <0.1 Hz (Mayhew et al., 1996; Cordes et al., 2001; Chan et al., 2015; Vanni et al., 2017), which are sufficiently sampled in ISOI and in fMRI. Second, signals recorded in ISOI and fMRI are lagging indicators of the electrophysiological and calcium signals measured in other methods (Logothetis et al., 2001; Devor et al., 2003; Shmuel and Leopold, 2008; Schölvinck et al., 2010; Ma et al., 2016; Shi et al., 2017). Thus, ISOI is perhaps the most versatile and least invasive optical method for recording RS in wild type animals.

3.5.2 High Resolution Cortical Parcellation

Cortical parcellation was achieved from dense microelectrode mapping that would not have been feasible without the longitudinal approach adopted. By generating an atlas for each hemisphere, we minimized the effects of inter-subject variability. We also eliminated distortions that could be expected from co-registering results across our animals or with curated squirrel monkey brains (Schilling et al., 2019). We justified our labor-intensive approach to cortical parcellation with the accuracy afforded for co-registering connectivity maps with anatomical and functional divisions. These provisions ensured that connectivity quantification was both accurate and objective. Moreover, they enabled us to use relatively small seeds ($\sim$230 μm diameter), which was in itself important for evaluating the granularity of FC maps.

3.5.3 FC Corresponds with Evoked Cortical Activation

FC patterns are consistent with cortical activation patterns driven by peripheral stimulation or behavioral demand (e.g., Vincent et al. (2007); Mohajerani et al. (2013); Vasireddi et al. (2016)). Those observations motivated us to benchmark our FC maps against stimulus driven activation. We compared FC maps from 48 seeds with ICMS-evoked activation maps (ICMS+ISOI) of the same cortical sites in the same subjects. We favored ICMS because it provides control over stimulus location, intensity, and is more effective than peripheral stimulation at driving motor cortical areas. High correspondence between FC and ICMS-evoked activation confirmed the effectiveness of RS-ISOI at revealing fine details of cortical networks.

3.5.4 FC Corresponds with Anatomical Connectivity

The relationship between FC and anatomical connectivity (AC) has been intensely investigated with several approaches. The general consensus is that strong AC is predictive of FC (Buckner et al., 2013). This principle is instructive for generating hypotheses about

functional networks, but it also underscores the limited utility of FC for interrogating AC. Our direct comparisons showed strong correspondence between FC and AC both in terms of spatial organization and connectivity strength. The FC map that we generated for each seed was in effect a faithful projection of monosynaptic, ipsilateral, connections for that site. This observation supports a tight relationship between FC and intra-hemispheric AC, which we would also expect for other cortical networks.

We leveraged ICMS+ISOI to expand comparisons between FC and AC. An inherent assumption here is that ICMS-evoked activation [i.e., effective connectivity (EC)] accurately reports AC (Ferezou et al., 2007; Matsui et al., 2011; Grimaldi et al., 2016; Card and Gharbawie, 2020; Friedman et al., 2020). Indeed, that assumption was confirmed in the fit that we reported between AC maps and EC maps. In using EC as a surrogate for AC, we increased the number of comparisons between FC and AC by ∼10x (5 tracer sites vs 48 ICMS sites). High correspondence in those comparisons confirmed a tight relationship between FC and AC throughout the sensorimotor network. Similarly, the poor fit observed between FC and EC for non-matching sites points to the spatial specificity in both methods, which was likely conferred from monosynaptic connections.

Several features of our experimental design likely contributed to the detection of high correspondence between FC and AC. (1) FC and AC were compared at identical locations. (2) FC and AC were measured at columnar and cellular resolution, respectively. (3) Seed diameters were small and matched the size of tracer injection cores. (4) FC maps were thresholded to only retain pixels that reported connectivity across recordings. (5) Histological sectioning matched the planar view of the optical images, which facilitated accurate co-registration of FC and AC. (6) Our testbed was motor and somatosensory cortical areas, which form relatively strong network(s). (7) We compared FC to AC in the ipsilateral hemisphere only. Although discrepancies between FC and AC have been reported within hemisphere (Howells et al., 2020), they are more widely reported for interhemispheric connectivity (Greicius et al., 2009; Matsui et al., 2011; Adachi et al., 2012; Bauer et al., 2018; Thomas et al., 2021; Shen et al., 2015). For example, FC linking homotopic cortex has been reported for foci that lack interhemispheric connections (Vincent et al., 2007) and even in cases of corpus callosum agenesis (Tyszka et al., 2011). Thus, had we examined the opposite

hemisphere in our preparation, then we may have found less fidelity between FC and AC and between FC and EC as compared to our observations in the ipsilateral hemisphere.

3.5.5 Previous Comparisons of FC and AC

Previous efforts to understand the relationship between FC and AC have spanned various methods and species. For example, many human studies have compared FC patterns from RS-fMRI to fiber tract patterns from diffusion weighted imaging (dMRI) (Hagmann et al., 2008; Greicius et al., 2009; van den Heuvel et al., 2009; Honey et al., 2009; Adachi et al., 2012). Within subject comparisons are a major strength in those studies, but the acquisition tools themselves lack the effective resolution for fine network architecture. In fMRI for example, signal-to-noise ratio and voxel size ($\geq$1 mm isotropic) can blend nearby patches. Similarly, *in vivo* protocols of dMRI are limited in their sensitivity to detecting large, myelinated, fibers and have yet to match the level of detail achieved in *ex vivo* scans (Liu et al., 2020). In contrast, tracer injections, like in the present study, reveal site connections at cellular resolution. Several studies in monkeys have shown strong correspondence between FC from RS-fMRI and AC from tracer injections (Shen et al., 2012; Wang et al., 2013; Hori et al., 2020a). Those comparisons offer considerably higher spatial resolution than is feasible in the human studies, but they are still limited by the effective resolution of fMRI and the potential blurring that occurs from co-registering FC and AC from separate animals. Some rodent studies have compared FC from optical imaging to AC from tracer injections (Mohajerani et al., 2013; Bauer et al., 2018). Such comparisons ensure that FC and AC were both acquired at high spatial resolution, but the effective resolution in those comparisons is still limited by the impact of co-registering FC and AC from separate animals. Our experimental design remedied most of the issues discussed here, but of course our approach is not without its own limitations. For example, ISOI cannot measure activity in subcortical structures or cortical sulci. Also, deploying three connectivity methods in the same hemisphere limits the number of sites that can be practically investigated with ICMS or with tracers. In contrast, retrieving anatomical connectivity form curated reposi-

tories (e.g., CoCoMac, Marmoset Brain Connectivity Atlas, and Allen Brain Atlas) removes those constraints. Finally, the cranial window needed for ISOI limits its use in humans to subpopulations undergoing cranial surgery.

3.5.6 EEG Indicates Animal State and FC Quality

Correspondence was highest between FC and AC during *light sedation*. FC quality deteriorated in *semi-deep sedation* (EEG burst-suppression) and deteriorated further in *deep sedation* (EEG suppression). The relationship between FC quality and animal state was consistent with previous reports (Liu et al., 2013c; Hutchison et al., 2014; Areshenkoff et al., 2021). Also, the *light* state was maintained here with isoflurane dose 0.5-1.5%, which is consistent with concentrations previously recommended for high quality maps in monkey RS-fMRI (Hutchison et al., 2014). Nevertheless, we also accrued extensive observations in the same monkeys where the same isoflurane dose induced periodic EEG suppression, or even complete EEG suppression. We concluded from those observations that a pre-set isoflurane concentration does not guarantee that the desired *light* state will be maintained, or even achieved. Our mitigation strategy was to confirm from EEG patterns that an animal was in the *light* state for several minutes before resting sate recording commenced. Our results confirmed that intracranial EEG patterns are reliable indicators of animal state and by extension FC quality.

3.5.7 Conclusion

We showed that FC maps from RS-ISOI report cortical connectivity with remarkable fidelity and in granular detail. RS-ISOI combines strengths from fMRI and optical methods that make it an attractive solution for mapping cortical architecture. RS-ISOI has the potential to serve many questions in systems neuroscience particularly where RS-fMRI is not feasible or high-resolution FC maps are desired.

4.0 Principles of Sensorimotor Cortex Connectivity

Text and figures from this chapter are for a publication that will be submitted for review in July 2022.

4.1 Summary

Skilled movements require the coordination of neural activity throughout sensorimotor cortex. This most direct route of connectivity to achieve this coordination is corticocortical connections within and between the somatotopic representations of sensorimotor cortical areas including premotor cortex (PM), primary motor cortex (M1), and primary somatosensory cortex (S1). Although many such connections have been identified in previous work, the architecture of the functional network that they form is not clear due to limitations in the number of sites studied per animal or spatial resolution. Consequently, how neural activity in sensorimotor cortex is coordinated in service of skilled movements is not known. To address this knowledge gap, we investigated the connectivity of thousands of sites spanning squirrel monkey sensorimotor cortex to reveal network organization. In longitudinal experiments (∼1.5 years), we partitioned sensorimotor cortex using dense microelectrode mapping and measured functional connectivity at high spatial resolution with resting state intrinsic signal optical imaging (RS-ISOI). Next, we used supervised and unsupervised analyses to identify key organizational features of the sensorimotor network. Functional connectivity for thousands of cortical columns collectively formed networks that preferentially bound somatotopic representations across particular cortical areas. Connectivity between non-matched functional zones was dependent on cortical area. Connections between motor and sensory areas mostly targeted proprioceptive sensory zones. These organizational features collectively grant insight into how the sensorimotor network contributes to the generation of skilled movements.

4.2 Introduction

Sensorimotor cortex is central to the production of voluntary movements, and is functionally organized according to cytoarchitecture (i.e., cortical areas) and somatotopy. Dense intra- and inter-areal corticocortical connections offer direct routes of communication within and between premotor cortex (PM), primary motor cortex (M1), and primary somatosensory cortex (S1; Dancause et al. (2006a,b); Davare et al. (2008); Dum and Strick (2005); Gharbawie et al. (2010); Hamadjida et al. (2016); Dea et al. (2016); Liao et al. (2013); Stepniewska et al. (1993, 2006)). The functional network formed by these connections is likely to contribute to the sensorimotor integration necessary for the production of skilled movements (Flesher et al., 2021; Monzée et al., 2003; Rothwell et al., 1982). However, limitations in spatial resolution (e.g., with fMRI) or in the number of cortical sites per animal that connectivity can be measured for (e.g., with neuroanatomical tracers) have precluded previous connectivity tracing approaches from identifying organizational features of the sensorimotor functional network. Consequently, we have an incomplete understanding of cortical basis of skilled movement generation. Mapping sensorimotor cortex connectivity and the networks formed by that connectivity would provide a clearer understanding of how skilled movements are generated.

The base functional unit of cortical architecture is the cortical column (Hubel and Wiesel, 1963; Mountcastle, 1997). Therefore, a clear understanding of cortical network architecture requires information concerning (1) the functional identity of every column in the network and (2) the strength of connectivity between every pair of columns. Within sensorimotor cortex, the functional identity of columns can be measured using microelectrode mapping approaches including intracortical microstimulation (ICMS) and multi-unit recordings. In chapter 3 (Card and Gharbawie, 2022), we demonstrated that resting state intrinsic signal optical imaging (RS-ISOI) can be used to identify high-resolution ($\sim$13 μm/pixel) FC that is faithful to underlying monosynaptic connectivity. Here, we utilize RS-ISOI to measure FC for each column spanning sensorimotor cortex, which is necessary to identify organizational features of the connectivity that forms the sensorimotor network.

The present study was motivated by a need to understand the principles that govern

the network architecture of sensorimotor cortex. Within sensorimotor cortex, our main objectives were to (1) parcellate cortical areas and somatotopy, (2) measure functional connectivity of thousands of sites, (3) identify architecture of networks and subnetworks, and (4) quantify relationships between connectivity, somatotopy, and cortical areas. To accomplish these objectives, we first used microelectrode mapping at hundreds of sites to identify the cytoarchitecture and somatotopy of sensorimotor cortex in three squirrel monkeys. In the same animals, we used RS-ISOI to identify FC for thousands of sites throughout the sensorimotor cortex. Next, we applied an unsupervised, modularity-based community detection approach to identify key networks and subnetworks that reflected somatotopic organization and were consistent across animals. Finally, we quantified the connectivity of thousands of sites in relation to cytoarchitecture and somatotopy to identify key principles that govern sensorimotor network architecture. Our observations grant insight into how corticocortical connectivity may contribute to sensorimotor coordination.

4.3 Methods

4.3.1 Animals

Experiments were performed on 2 adult male squirrel monkeys (*Saimiri boliviensis*). Animals were 4 years old and weighed between 800-1200 g. All procedures were approved by the University of Pittsburgh Institutional Animal Care and Use Committee and followed the guidelines of the National Institutes of Health guide for the care and use of laboratory animals.

4.3.2 Surgical Procedures

All procedures and data acquisition were conducted under anesthesia (Table 1). Thirty minutes before sedation, animals were treated with an antiemetic (Zofran, 0.3 mg/kg, IM) and Atropine (0.03 mg/kg, IM) to reduce secretions. Ketamine induction (10-15 mg/kg, IM) was followed with isoflurane (0.5-2.5%) in O2 (2-3 L/min). Once sedated, Dexamethasone (1

mg/kg, IM), Ketofen (2 mg/kg, IM), and Gentamicin (2 mg/kg, IM) were administered to prevent brain swelling, pain, and infection, respectively. Animals were intubated, artificially ventilated, wrapped in a heating blanket, and secured in a stereotaxic frame. Fluids (5% dextrose in Lactated Ringer's solution, 2-3 ml/kg/hr, IV) were provided continuously. Heart rate, arterial oxygen saturation, expired CO2, blood glucose, and body temperature were monitored.

A scalp incision was performed for each procedure. All steps from this point were conducted with the aid of a surgical microscope. In the first procedure for each animal, a rectangular window was opened in the skull over frontal and parietal cortex (∼25 x 20 mm, Fig. 4.1A). That window was accessed in multiple subsequent procedures. After a durotomy, cortical pulsations were stabilized with 3% agarose (Invitrogen, Carlsbad, CA) solution in physiological saline. Data acquisition proceeded from this point and lasted for several hours. The agar was removed at the conclusion of data acquisition and an artificial dura (Tecoflex EG-85 resin, Sakas et al. (1990)) was secured into the cranial opening to protect the exposed cortex. The craniotomy was sealed with dental cement and the scalp was sutured closed. The animal was recovered from anesthesia and another dose of the pre-procedure drugs was administered in addition to Vitamin B12 (0.5 mg/kg, IM). Analgesics and corticosteroids were administered every 12 hours for the following 72 hours. Procedures lasted ∼14 hours from sedation to alertness.

Table 4.1: Procedures and data collected from each animal[a]

Monkey	Procedures	Motor Map Sites	Receptive Field Sites	Resting State Runs
B	14	264	169	13
R	13	231	251	15
C	8	130	166	12
Total	35	625	586	40

a. Numbers are limited to data included in the present study.

4.3.3 Monitoring Animal State with EEG

Electroencephalogram (EEG) signals were recorded for monitoring animal state. Stainless steel wires (3 strand, 102 μm diameter, AM systems, Sequim, WA) were inserted into bilateral burr holes near the frontal pole and then secured with dental cement. Wires were removed at the conclusion of each procedure and burr holes were resealed with dental cement. The voltage differential between the two leads was amplified (10,000x), bandpass filtered (1-500 Hz), and notch filtered (60 Hz) using an AC Amplifier (Model 2800, AM Systems, Sequim, WA). The filtered signal was visualized on an oscilloscope, digitized (1000 Hz, NI USB-6008, National Instruments, Austin, TX), and recorded in MATLAB. During data collection, respiration rate and percent isoflurane were adjusted while EEG signals were monitored to achieve a state of light sedation wherein slow waveforms were punctuated by suppression in <2.0% of the recording. This animal state is conducive to high-quality resting state intrinsic signal optical imaging (RS-ISOI) recordings (Card and Gharbawie, 2022).

4.3.4 Motor Mapping

We used intracortical microstimulation (ICMS) to map the somatotopic organization of primary motor cortex (M1) and premotor cortex (Fig. 4.1B). A hydraulic microdrive (Narishige MO-10, Amityville, NY) connected to a Kopf micromanipulator (Tajunga, CA) was used for positioning a platinum/iridium microelectrode (125 μm shaft, 300 kΩ median impedance, MicroProbes, Gaithersburg, MD). Each penetration targeted layer V (1800 μm deep) to deliver microstimulation trains (18 cathodal pulses, 0.2 ms pulse width, 300 Hz pulse frequency, 1 Hz train frequency) from an 8-channel stimulator (model 3800, AM Systems, Sequim, WA). Current amplitude was adjusted with a stimulus isolation unit (model BSI-2A, BAK Electronics, Umatilla, FL) until a movement was evoked and up to a maximum of 150 μA. Threshold for a site was the minimum current amplitude that evoked movement on $\sim$50% of microstimulation trains. Combining ketamine infusion (3–6 mg/kg/hr) with low doses of isoflurane (<0.5%) was central to maintaining a state in which ICMS reliably evoked movements.

Two to three experimenters evaluated the evoked movements. Only one experimenter was not blind to the microelectrode location. Each ICMS site was classified according to joint (digit, elbow, etc.) and movement type (e.g., flexion, extension, etc.) that showed the most robust effect at the lowest current amplitude. Mapping was completed over several procedures (30–60 ICMS sites/procedure). Distance between ICMS sites was typically <1 mm. Sites were recorded on a high-resolution photo of cortex. Color coded maps were generated in MATLAB using a Voronoi diagram (*voronoi* function) constrained to 1.0 mm radius per site. Rostral and caudal M1 borders were estimated from current thresholds ($\geq$80 μA), distance from central sulcus, and in relation to area 3a (described next).

4.3.5 Somatosensory Mapping

We recorded multi-unit activity to map the somatotopic organization of somatosensory cortex (Fig. 4.1C). A tungsten or platinum/iridium microelectrode (125 μm shaft, 420 kΩ median impedance) was lowered to layer IV (700–800 μm deep). Distance between sites was typically <1 mm. Signal was amplified (10,000x) and filtered (bandpass 300–5000 Hz, notch 60 Hz) using an AC amplifier (Model 2800, AM Systems, Sequim, WA). The signal was then passed through a 50/60 Hz noise eliminator (HumBug, Quest Scientific Instruments Inc., Vancouver, BC) and monitored with an oscilloscope and a loudspeaker. Receptive fields were determined from neural responses to stimulation of the contralateral body. Responses were classified as cutaneous or proprioceptive. Units in areas 3b and 1 responded to cutaneous stimulation and had relatively small receptive fields (e.g., single digit phalanx). In contrast, units in area 3a were unresponsive to skin contact and responded only weakly to the manipulation of multiple joints (e.g., entire digit or multiple digits). Area 2 contained a mixture of units that responded to joint manipulation or cutaneous stimulation. Cortical borders were estimated from transitions in receptive field properties along the rostro-caudal dimension (Sur et al., 1982). Somatosensory maps were generated with Voronoi diagrams as described above.

4.3.6 Intrinsic Signal Optical Imaging

We used intrinsic signal optical imaging (ISOI) to measure spontaneous hemodynamic fluctuations in the resting state (RS). Images of cortex were acquired with a camera (Photon Focus, Lachen, Switzerland) based on a 12-bit CMOS sensor (1312 x 1082 pixels). An optical imaging system (Imager 3001, Optical Imaging Ltd, Rehovot, Israel) controlled image acquisition. A tandem lens combination (20 mm / 50 mm) provided a field-of-view (FOV; ∼26 x 22 mm; ∼19 μm/pixel) that included the microelectrode mapping territory as well as 2-3 mm of skull around the perimeter. Camera angles were adjusted with a 3-axis geared head (410 Junior Geared Tripod Head, Manfrotto, Cassola, Italy). Camera position (x, y, and z directions) was translated with independent linear stages. For spatial reference, blood vessel patterns were imaged (528 nm illumination) at the start of each ISOI recording. Three independently controlled LEDs (620 nm) provided illumination during ISOI.

4.3.7 Common Reference Registration

The common reference for each hemisphere was a high-resolution, high-contrast image of the cortical blood vessels. Microelectrode penetrations were marked on that image. ISOI frames were co-registered to the common reference using non-linear bicubic transformation for 300–600 points. Co-registration was conducted with a custom MATLAB script and a script from the MATLAB file exchange [B-spline Grid, Image and Point based Registration, Dirk- Jan Kroon, 2021].

4.3.8 Resting State ISOI

For each imaging session, spontaneous cortical activity was recorded with ISOI for 15 min (Fig. 4.2A). Frames were temporally binned to 10 Hz. The raw time course and power spectrum for the entire FOV was examined for initial assessment of image quality. Segments of data were excluded if there was evidence of artifact, which was typically due to illumination instability, animal state fluctuations, or setup vibrations. The remaining frames were spatially binned by a factor of 3 (from ∼19 μm/pixel to ∼58 μm/pixel). Multiple

imaging sessions were collected across multiple procedures for each animal (Table 4.1).

Image processing was conducted in both the temporal and spatial domains using MATLAB scripts. Processing steps are identical to those performed in chapter 3 (Card and Gharbawie, 2022). (1) Frames were temporally binned from 10 Hz to 2 Hz for de-noising and to speed up computation. (2) A moving median filter (2 s window) smoothed the time course of each pixel to minimize noise. (3) First-frame subtraction converted pixel values to reflectance change (ΔR/R%) from baseline. (4) A high-pass filter (Butterworth, 3rd order, cutoff 0.005 Hz) was applied to each pixel to minimize the effects of illumination drift. (5) Multiple linear regression was used to minimize the effects of global signals, blood vessel activity, and residual artifact. Principal component analysis (PCA) and k-means clustering were iteratively applied to pixels overlapping the skull and blood vessels until we accounted for 85–90% of the variance in pixel values. This was achieved with 5–6 clusters of pixels over the skull and 5–6 clusters of pixels over major blood vessels. For each cluster, the average time course of all pixels was used as a regressor in the multiple linear regression. The average time course for all visible cortex was used as an additional regressor, which is similar to global signal regression in RS-fMRI (Murphy and Fox, 2017). (6) Frames were then spatially filtered for smoothing (gaussian kernel = 2 pixels or 120 μm radius). (7) Each time course was bandpass filtered (Butterworth, 3rd order, 0.01–0.10 Hz) to hone in on infra-slow signals (Cordes et al., 2001).

4.3.9 Functional Connectivity Maps

Individual imaging runs were processed and registered to a common FOV on a frame-by-frame basis. Imaging data was spatially down-sampled further (from $\sim$58 μm/pixel to $\sim$270 μm/pixel) to reduce computation time in subsequent steps. We considered the minimum acceptable resolution to be $\sim$300 μm/pixel to match the approximate size of a cortical column. For each imaging run, functional connectivity (FC) was measured for each pixel that overlapped cortex (i.e., not vessels or skull). The pixel that functional connectivity was being measured at was the seed pixel. The seed time course (Fig. 4.2B, inset) was correlated (Pearson) with the time courses of all other cortex-overlapping pixels. Pixels were color

coded according to coefficient values to generate an FC map. FC maps from the same seed were averaged across individual imaging runs for de-noising. Pixels were excluded if their distribution of coefficients across imaging runs was significantly less than zero (unpaired t-test, $p < 0.001$, Fig. 4.2C). The connectivity motif of an FC map was quantified according to the distribution of thresholded coefficients in relation to the underlying microelectrode map and cortical area borders (Fig. 4.2D-E). The connectivity strength for an FC map with each somatotopic representation was calculated using the following equation:

$$ConnectivityStrength = \sum_{j=1}^{J} \sum_{n=1}^{N} p_i * M_{ji} \tag{4.1}$$

Where J was the number of somatotopic representations in the microelectrode map, N was the number of significantly positive coefficients in the map, ρ was the coefficient value at each pixel, and M was the classification percentage at each pixel for a given somatotopic representation. A similar calculation was done to quantify the cortical areas than an FC map overlapped. Thus, connectivity strength was a weighted measure of the somatotopic representations or cortical areas that each FC map overlapped. Connectivity strength was normalized and converted to a percentage in all cases.

4.3.10 Functional Connectivity Matrices

Averaged and thresholded FC maps were calculated for every pixel that overlapped cortex in the FOV. Maps were organized into a matrix of size n x n, where n was the number of pixels overlapping microelectrode-mapped cortex (Fig. 4.3A-B). The resulting FC matrix represents the average correlation between every pair of pixels in the FOV that overlapped cortex. If the distribution of individual correlation values between a pair of pixels was not significantly greater than 0 (unpaired t-test, $p < 0.001$), the correlation value was set to 0 in the FC matrix. Rearrangement of FC maps into an FC matrix was essential for network-wide analyses, described next.

4.3.11 Multi-Resolution Hierarchical Consensus Clustering

We implemented an unsupervised community detection approach to investigate sensorimotor network architecture. Louvain community detection (Blondel et al., 2008) and multiresolution hierarchical consensus clustering (Jeub et al., 2018) were used to identify a hierarchy of communities from RS-ISOI data. First, Louvain community detection was applied to the FC matrix to optimally subdivide the network into nonoverlapping communities of pixels wherein the modularity of the network was maximized. Networks with high modularity have dense connections within communities, but sparse connections between communities. Louvain community detection was applied in two sweeps. In each sweep, the resolution parameter (γ) was iteratively changed, resulting in the detection of communities at different scales (fewer, larger communities at $0 < \gamma < 1$; additional, smaller communities at $\gamma > 1$). The first sweep sparsely iterated γ (200 iterations) to identify the γ range that resulted in partitions with 2-N communities, where N was a specified maximum number of communities (1,000 in the present case). The second sweep finely iterated γ (2,000 iterations) within that range. The 2,000 community partitions identified in the second sweep were then aggregated into a co-classification matrix (C), whose elements indicated the probability that any two pixels were assigned to the same community (Fig. 4.3C).

Lasty, the hierarchical consensus (HC; https://github.com/LJeub/HierarchicalConsensus) procedure was applied to the community partitions. The HC procedure started by assuming all pixels were part of the same community, and then applied modularity-based consensus clustering at a given significance level ($\alpha = 0.01$) to split that community into subcommunities. The significance threshold ensured that communities were not split into subcommunities that could emerge by chance. We also restricted the size of subcommunities to > 0.5 mm^2 to reduce noisy subdivisions. If any subcommunities were smaller than the specified size, the split was not performed. This procedure was repeated for each newly generated community until they could no longer be split into subcommunities of a sufficient size and at the given significance threshold. The final result of the HC procedure was the hierarchical community structure of the network, or hierarchy tree (Fig. 4.3D).

Altogether, this community detection approach allowed us to identify an unspecified number of communities within a network, across a large range of scales, and with a hierarchical structure wherein large communities contain smaller, statistically significant subcommunities. When this community detection approach was applied to our RS-ISOI data, these key features served our goal of parcellating sensorimotor cortex into distinct, meaningful subnetworks.

4.3.12 Statistical Analyses

Statistical tests were performed using SPSS and MATLAB. Parametric tests were used wherever assumptions about the distribution were satisfied (e.g., normality and homoscedasticity). Normality was tested using the Kolmogorov–Smirnov test and homoscedasticity was tested using Levene's test. Non-parametric tests were used if assumptions were not satisfied. For one- or two-sample comparisons, either a t-test or a Wilcoxon rank-sum test was performed. For comparisons across >2 parametric populations, a one-way ANOVA was used with a post hoc Tukey's HSD test. For comparisons across >2 non-parametric populations, a Kruskal-Wallis test was performed with a post hoc Dunn's test. For all tests, a significance level of $\alpha = 0.05$ was used. Bonferroni correction was applied where appropriate. Significance conventions in figures: $*p < 0.05$, $**p < 0.01$, $***p < 0.001$.

4.4 Results

In three squirrel monkeys, we investigated the network architecture of the forelimb and surrounding representations in sensorimotor cortex. We parcellated sensorimotor cortex using microelectrode mapping and recorded resting state intrinsic signal optical imaging (RS-ISOI) in monthly experiments conducted over ∼1.5 years. We measured the functional connectivity (FC) at thousands of sites throughout sensorimotor cortex and investigated network architecture using an unsupervised community detection approach and a supervised seed-based approach. In the unsupervised approach, we used modularity-based community

detection to identify a hierarchy of strongly connected communities. Spatial correspondence between communities and microelectrode maps revealed organizational features of the sensorimotor network that were consistent between monkeys. In the seed-based approach, we quantified the connectivity strength of individual network nodes to reveal relationships between connectivity, cytoarchitecture, and somatotopy that provided further insight into the functional network architecture of sensorimotor cortex.

4.4.1 Consistent Cortical Parcellation with Microelectrode Mapping

We used high-density microelectrode mapping (¡1 mm between sites) to define cytoarchitecture (i.e., cortical borders) and somatotopy in motor and somatosensory cortex. Cortical borders were estimated from current thresholds, receptive field properties, and distance to central sulcus. Motor maps (e.g., Fig 4.1B) and somatosensory maps (e.g., Fig 4.1C) were merged into combined maps for each animal (Fig 4.1D-F). Combined maps were consistent between monkeys and followed a medial-lateral organization (leg to face) that is well-established for New World monkeys (Gould et al., 1986; Mayer et al., 2019; Merzenich et al., 1978; Padberg et al., 2005; Welker et al., 1957). Within M1, hand zones (digit and wrist) were surrounded by arm zones (elbow and shoulder), which is consistent with previous work (Card and Gharbawie, 2020; Dancause et al., 2008). PMv and PMd contained independent hand zones (Fig. 4.1D-F) that were bordered or surrounded by arm zones. The size of responsive cortical territory was similar between animals (monkey B = 220.9 mm^2, monkey R = 237.6 mm^2, monkey C = 261.6 mm^2). Map stability was confirmed by retesting a subset sites months after initial classification. Most retested sites (44/51, 82.3%) had the same classification at both time points (238 $\pm$ 127 days apart, 194 $\pm$ 54 μm apart, mean $\pm$ SD). This sample of retested sites confirms that microelectrode maps were sufficiently stable over time for reliable cortical parcellation.

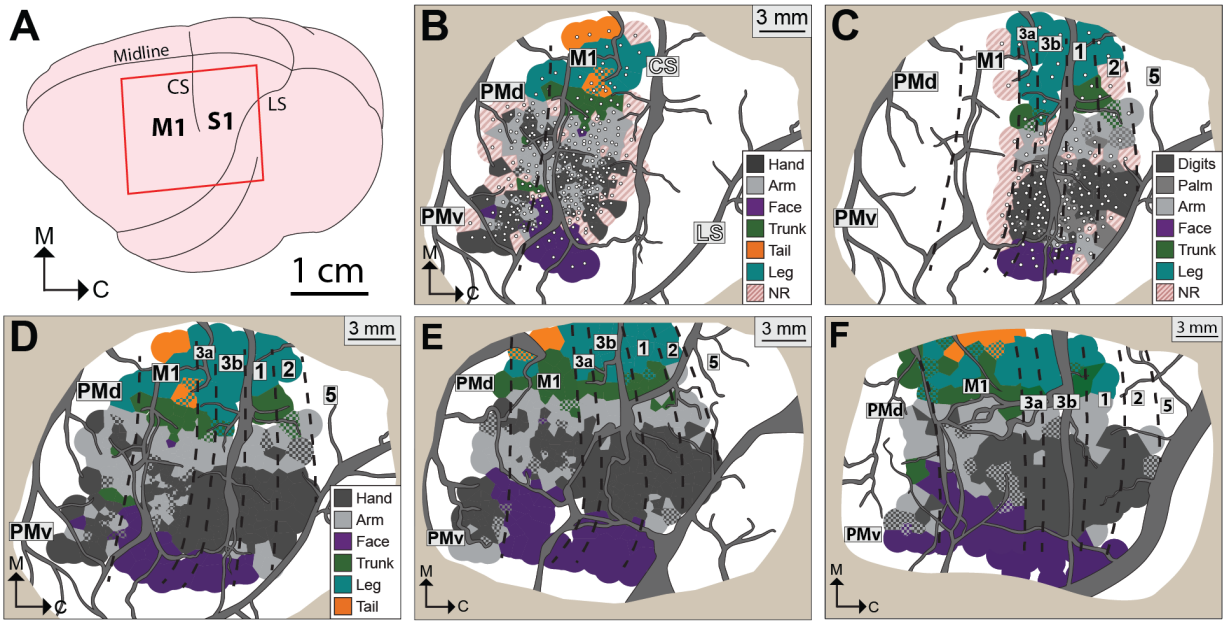

Figure 4.1: Microelectrode maps parcellate sensorimotor cortex. (A) Schematic of squirrel monkey brain showing the locations of cortical areas in the left hemisphere that we targeted for microelectrode mapping. Red rectangle approximates the field of view in (B-F) (B) Motor maps for PMd, PMv, and M1 from the left hemisphere (monkey B). White dots are intracortical microstimulation sites (ICMS, n = 264). Voronoi tiles (1.0 mm radius) are color coded according to ICMS-evoked movement evoked at lowest current amplitude. Checkered tiles depict multiple movements (1 color/body part). Non-responsive sites (NR) failed to evoke movements at 150 μA. The rostral M1 border (dashed line) was estimated from current thresholds and distance to central sulcus (CS). Major vessels are masked in gray. LS: lateral sulcus. Tan color in the perimeter masks resected dura and skull. Scale bar applies to (B-D). (C) Somatosensory maps for areas 3a, 3b, 1, and 2 from the same monkey and hemisphere as (A). White dots are microelectrode recording sites (n = 169). Voronoi tiles (1.0 mm radius) are color-coded according to body part that drove unit activity most effectively. Sites were classified as NR if stimulation and joint manipulation failed to evoke a response. Cortical borders (dashed lines) were estimated from receptive fields and distance from CS. (D) Combined maps from (B) and (C). NR sites were removed. Somatosensory sites with palm and digit responses are classified here as hand. (E-F) Combined maps for monkeys R and C, respectively.

4.4.2 Measuring Functional Connectivity with RS-ISOI

We used high-resolution RS-ISOI to measure spontaneous hemodynamic fluctuations throughout sensorimotor cortex. We placed the seed in the PMv hand zone (Fig. 4.2B, blue circle, 232 μm radius) to demonstrate the calculation, visualization, and quantification of a functional connectivity (FC) map. We chose this seed location because its connections are well-characterized and span long distances within the FOV. The processed time course of hemodynamic fluctuations for the seed during a representative 15-minute-long imaging run is shown in the inset. For each imaging run, we used Pearson correlation to quantify co-fluctuations in the seed time course and the time course at every other pixel. To remove noisy pixels, we averaged the coefficient map across imaging runs and thresholded the average coefficient map to exclude pixels whose distribution of coefficients was not significantly greater than zero (Fig. 4.2C, t-test, $p<0.001$). All FC maps from this point on are averaged and statistically thresholded unless otherwise noted.

The connectivity profile of the FC map for the PMv hand site was quantified based on the number and intensity of significant pixels overlapping each cortical area (Fig 4.2D) and somatotopic representation (Fig 4.2E). The connectivity profile indicates that this seed was mostly connected to the hand and arm representations spanning areas PMv, PMd, M1, 3a, and 2. FC maps for this seed and other benchmark seeds were consistent with stimulus-evoked connectivity (ICMS+ISOI) and tracer injections at identical sites in the same animals (Card and Gharbawie, 2022). We are therefore confident that FC maps measured with RS-ISOI are consistent with monosynaptic corticocortical connections.

We computed FC maps for thousands of seeds that spanned the microelectrode-mapped territory in each animal. We arranged FC maps into a matrix representing the FC between any two pixels (Fig. 4.3A-B). This matrix was therefore representative of all FC throughout the sensorimotor network. We applied an unsupervised community detection approach and a supervised seed-based approach to the FC matrix in order to identify key principles of connectivity within the sensorimotor network. The community detection approach segmented the network into a hierarchy of subnetworks in an unsupervised manner, whereas the seed-based

approach quantified connectivity strength for discrete nodes of the network. Combined, the two approaches provided a window into the network architecture of sensorimotor cortex.

4.4.3 Community Detection

In the community detection approach, we used multiresolution consensus clustering (MRCC) and hierarchical consensus (HC) clustering (Jeub et al., 2018) to identify communities of strongly connected pixels in the sensorimotor network. We chose this community detection approach for the following reasons: (1) the "multi-resolution" component of MRCC enables detection of communities across a large range of scales, (2) the number of communities is not specified by the user, and (3) HC statistically subdivides communities into subcommunities. These properties should enable the approach to effectively segment sensorimotor cortex into meaningful communities.

We applied MRCC to the FC matrix of each animal. The probability that any two pixels were grouped in the same community is shown in the co-classification matrix (Fig. 4.3C), which was visually similar to the FC matrix (Fig. 4.3B). White lines drawn over the co-classification matrix delineate the five starting communities (Fig. 4.3C). Finally, HC recursively subdivided these communities in a statistically significant manner ($\alpha = 0.01$) until no more subdivisions could be made. A hierarchy tree of community divisions is illustrated in Fig. 4.3D, where each column is a hierarchy level, and divisions within each column are individual communities. Subcommunities are colored as shades of their parent community. The height of a community in the tree is proportional to its size. This tree is vertically aligned with the FC matrix and co-classification matrix in the previous panels. We refer to the earlier levels of the hierarchy tree, which have fewer communities (Fig. 4.3D, leftmost columns), as superficial. Likewise, we refer to later hierarchy levels as deep. A map of the five communities at the most superficial level of hierarchy is shown in Fig. 4.3E. Colors are consistent between this community map and the community hierarchy tree.

4.4.4 Community Detection is Stable

Before examining the community maps any closer, we sought to ensure that the community detection algorithm yielded stable results. Toward this objective, we applied community detection on the same FC matrix several times for each animal. Similarity between communities across iterations was quantified by calculating their normalized mutual information (MIn, higher is better) and normalized variance of information (VIn, lower is better, Meilă (2007)). We observed high MIn (0.97 ± 0.02, mean ± STD) and low VIn (0.02 ± 0.02) between community detection iterations in all three animals (Fig. 4.3F). To put context to these values, we compared community partitions to partially randomized versions of themselves (Fig. 4.3G). Identical community partitions had a MIn value of 1.00 ± 0.00 (mean ± SD), which decreased as the partition was increasingly randomized until a value of 0.03 ± 0.03 at 100% partition randomization. Identical community partitions had a VIn value of 0.00 ± 0.00 (mean ± SD), which increased to a value of 0.66 ± 0.22 at 100% partition randomization. From this contextual information, we calculated that the MIn and VIn values obtained across community detection iterations (Fig. 4.3F) were equivalent to ∼2% randomization of the community partition across iterations. Therefore, detected communities had 98% spatial stability across iterations, which we determined to be sufficiently stable.

Next, we compared the number of communities detected as a function of hierarchy level for each animal (Fig. 4.3H). Of course, deeper levels had more communities than superficial levels. From levels 1-4, the number of communities increased slowly as there were few communities to split. The rate of community subdivision was maximized from levels 4-8. Beyond level 8, the rate of community subdivision slowed as communities weren't able to be significantly subdivided. At the deepest levels, it was evident that the most communities were present for monkey C (blue), followed by monkey R (green) and monkey B (red). However, we found that communities at the deepest level in each animal were similar sizes (monkey B: 0.87 ± 1.03 mm^2 (mean ± SD); monkey R: 0.98 ± 0.95 mm^2; monkey C: 0.86 ± 0.93 mm^2). The difference in number of communities between animals, coupled with the similar average size of communities in each animal, could be reconciled by the fact that animals have slightly differing total area of mapped cortical territory (Fig. 4.3H, inset).

Finally, we examined the relationship between the number of communities and different HC α thresholds. We compared community detection results at three α thresholds (0.05, 0.01, and 0.001). We found that at superficial hierarchy levels there was little-to-no difference in the number of communities (Fig. 4.3I). However, at deeper hierarchy levels, more lenient (larger) α thresholds returned more communities. This result was intuitive given that a more lenient α threshold lowers the bar for statistically subdividing communities. This analysis was useful for visualizing the effect of the α parameter, but from this point on all community detection results used $\alpha = 0.01$.

4.4.5 Sensorimotor Cortex Networks Parcellated with Community Detection

Communities were generally spatially consistent across animals and appeared to follow some somatotopic and cytoarchitectonic (i.e., cortical area) boundaries. In each animal, 4-5 communities were detected at the most superficial hierarchy level (Fig. 4.4B,E,H). Communities were color-coded to emphasize similarities between animals. These communities spanned multiple cortical areas, but showed noticeable correspondence with somatotopy (Fig. 4.4A,D,G). Purple communities, along the lateral edge of the FOV, overlapped the face representation nearly exclusively. Similarly, red communities, bisecting the FOV along the rostral-caudal axis, included nearly all hand zones, in addition to some arm zones. The border between purple and red communities was aligned to the forelimb-face border in the microelectrode maps. This result is consistent with the near absence of connectivity between forelimb and face representations in sensorimotor cortex (Card and Gharbawie, 2020; Huntley and Jones, 1991; Liao et al., 2013; Stepniewska et al., 1993; Weiss and Keller, 1994). Finally, green communities, along the medial edge of the FOV, included all trunk, leg, and tail zones, in addition to some arm zones.

Communities varied between animals at this level of hierarchy. For example, the face representation encompassed two communities in monkey R (Fig. 4.4E, purple communities), but only one community in monkeys B and C (Fig. 4.4B, H, purple). Similar observations were present for the hand- and leg-overlapping communities (red and green, respectively). Furthermore, arm and hand zones in premotor cortex were included in a single community

in monkey B (Fig. 4.4B, dark red) and monkey R (Fig. 4.4E, red), but are split between two communities in monkey C (Fig. 4.4H, red and dark green). All of these differences may be attributed to the fact that communities in superficial hierarchy levels were formed based on all connectivity, including weaker connections. At deeper hierarchy levels, community partitions were increasingly weighted toward only the strongest connectivity. Thus, we may expect communities at deeper levels of hierarchy to be more spatially consistent between animals.

Deeper in the community hierarchy, larger communities had subdivided several times into statistically independent smaller communities (Fig. 4.4C, F, I). Communities here were colored as shades of the color of their parent community. For example, purple-shaded communities in level 5 (e.g., Fig. 4.4C) were subcommunities of the purple community(s) from level 2 (e.g., Fig. 4.4B). At this deeper hierarchy level, we continued to make visual observations of similarities and differences between the community maps of each animal. For example, the PMv hand representation was mostly grouped into a single community in all three animals (Fig. 4.4C, F, I, dark red, labeled by yellow arrowheads). Additionally, the somatosensory hand representation was mostly grouped into a single community (labeled by cyan arrowheads) spanning area 3a, 3b, 1, and 2 in all three animals. The rostral edge of these somatosensory hand communities was close to the M1/3a border. Similar divisions near the M1/3a border were seen in purple communities in all animals. Thus, it appears that community borders aligned to certain cytoarchitectonic boundaries in addition to somatotopic boundaries.

Despite key similarities, community partitions at level 5 of the hierarchical tree were not identical across animals. For example, the M1 forelimb representation was subdivided into multiple communities in monkey B (Fig. 4.4C) and monkey C (Fig. 4.4I), but was grouped into a single community in monkey R (Fig. 4.4F, light red). Differences of this nature may be attributed to the fact that the forelimb community in monkey R started out quite large in level 2 (Fig. 4.4E), and may therefore take additional iterations of subdivision to break down into smaller subcommunities. In spite of these differences, communities appeared to reflect the structure of the microelectrode map.

The above community detection results were based only on significantly positive FC. However, because of the global signal regression applied to RS-ISOI data during processing, correlation values below 0 also exist in our dataset. Interpretation of negative correlations after global regression is unclear (Murphy and Fox, 2017), so we chose to exclude them from our main community detection results. However, in a separate analysis, we applied community detection to a FC matrix where positive correlation values were set to 0 so that only negative correlation relationships remained (Fig. 4.5). At the most superficial hierarchy level, 2-3 communities were detected in each animal, one of which was almost entirely bound to the arm and hand representations across cortical areas. Communities did not subdivide into meaningful subcommunities. This finding demonstrates that limited somatotopic structure still exists in anticorrelated FC values.

4.4.6 Communities Respect Topographical Borders

We next aimed to quantify the extent to which communities followed boundaries in somatotopy and cortical areas. To accomplish this, we calculated the representation isolation and area isolation for each community at hierarchy levels 2-5. To calculate representation isolation for a given community, we first calculated the extent to which it overlapped each somatotopic representation, and then took the maximum percentage overlap. For example, a community that overlapped 50% arm, 30% hand, and 20% face would have a representation isolation value of 50%. Area isolation was calculated in a similar manner, but for cortical areas instead of representations. Together, these metrics enabled us to quantify how bound each community was to a single representation or cortical area.

As a comparison to chance, we repeated this calculation with randomized contiguous community maps. Randomized maps were generated for each hierarchy level by choosing random coordinates within the FOV and generating voronoi tiles based on those coordinates. We chose to make randomized community maps contiguous because the vast majority of actual communities were contiguous. The number of communities in each randomized community map was equal to the number of communities in the corresponding hierarchy level. Examples of multiple iterations of randomized community maps are shown for hierarchy level

2 (Fig 4.4J, top) and level 5 (Fig. 4.4J, bottom). These randomized maps correspond to the number of communities found in level 2 and 5 for monkey B (Fig. 4.4B, C).

Finally, we compared representation isolation between real community maps and randomized maps. We found that, for all animals, real communities were more bound to individual representations than randomized communities (Fig. 4.4K, white bar, t-test, $p<0.05$). When broken down further, we found that this trend was true for communities in the hand (dark gray bar, $p<0.05$), arm (light gray bar, $p<0.01$), face (purple bar, $p<0.001$), and trunk (green bar, $p<0.01$) representations. In contrast, communities in the leg/tail representation (turquoise bar, $p>0.05$) were not bound to individual representations more so than random communities.

When we compared cortical area isolation between real and randomized communities, we found that the population of real communities were less bound to individual cortical areas than random communities (Fig. 4.4L, white bar, t-test, $p<0.001$). This relationship persisted for communities overlapping the hand (dark gray bar, $p<0.001$), arm (light gray bar, $p<0.05$) and trunk (green bar, $p<0.05$) representations. Communities overlapping the face and leg/tail representations were bound to individual cortical areas at a rate equal to chance (purple and turquoise bars, $p>0.05$).

Taken together, these quantitative results confirm many of the visual observations that we made about community maps. Overall, communities parcellate individual somatotopic representations at a rate better than chance and parcellate individual cortical areas at a rate worse than chance. This indicates that communities bind similar representations across cortical borders, consistent with our observations, and consistent with the somatotopic organization of the microelectrode maps. Thus, RS-ISOI and unsupervised community detection can be used to identify boundaries in somatotopy at a high spatial resolution. Given the invasive nature of microelectrode mapping and the large amount of time required to map large swaths of cortex at a high spatial resolution, the community detection approach shown here may provide a suitable alternative. This finding has exciting implications for future studies involving functional mapping of cortex, both in sensorimotor cortex or other cortical zones.

4.4.7 Consistent Forelimb Communities Between Animals

Next, we turned our attention to communities within the forelimb representation. For each animal, we identified the community that overlapped the largest amount of hand representation in premotor cortex, M1, and S1. The size, spatial arrangement, and topographical overlap of the three hand-overlapping communities was mostly consistent between the three animals (Fig 4.6A-B, E-F, I-J). The premotor communities (green) were in PMv and overlapped mostly hand, followed by arm and face. The M1 communities (red) overlapped slightly more hand than arm. The S1 communities (blue) overlapped almost exclusively the hand representation. The disparity in crossover between arm and hand representations in motor and sensory zones was not surprising given that these representations tend to be somewhat spatially mixed in motor areas, but highly separable in sensory areas (Fig. 4.1D-F).

When we zoomed in even further and looked at subcommunities within the S1 hand communities, we were able to identify three subcommunities in areas 3a and 3b that overlapped 1-2 digits each (Fig 4.6C-D, G-H, K-L). Here, blue communities overlapped primarily D1, followed by D2. Red communities overlapped primarily D2, followed by D3. Green communities overlapped D3 and D4. The fact that these communities mostly overlapped 1-2 digit representations was consistent with known connectivity of individual digits in area 3b (Liao et al., 2013; Négyessy et al., 2013). Consistency between animals at the level of individual digit representations confirmed the robustness of the FC and the clustering approach implemented.

4.4.8 Connectivity Strength Throughout the Sensorimotor Network

Our next objective was to investigate FC strength throughout the sensorimotor network. While the community detection approach provided a high-level perspective of the network structure, connectivity strength between cortical zones was not easily accessible in community maps. Therefore, toward a clear depiction of connectivity strength throughout sensorimotor cortex, we calculated the FC strength of every single seed in each animal (monkey B: 2467 seeds, monkey R: 2869 seeds, monkey C: 3224 seeds). FC strength of a seed was a normalized, weighted sum of the significantly positive correlations overlapping each soma-

totopic representation and cortical area (equation 1 in methods). We examined the spatial extent of connectivity at all 8,560 seeds (Fig. 4.7D). We found that, on average, 50% of pixels connected to a given seed were within 3 mm of the seed. Beyond 3 mm, connectivity was with patches that were in some instances >15 mm from the seed.

When we grouped seeds by their somatotopic identity, we were able to visualize the average connectivity strength between somatotopic representations (Fig. 4.7A). Connectivity strength was normalized such that the strongest connection in the graph was 100% strength. Connectivity was strongest between hand and arm representations and trunk and leg/tail representations, followed by arm and trunk representations. The face representation was relatively isolated from other representations, consistent with our observations from community maps and with previous findings (Card and Gharbawie, 2020; Huntley and Jones, 1991; Liao et al., 2013; Weiss and Keller, 1994). Connectivity strength was also weak between the arm and leg/tail representations and between the hand and trunk representations. We also examined connectivity strength between cortical areas (Fig. 4.7B). We found that all adjacent areas had a strong connectivity. Connectivity between non-adjacent areas was in many cases only marginally weaker than connectivity between adjacent cortical areas (e.g., M1 connectivity with areas 3b, 1, and 2). Connectivity between other areas was weak (e.g., PMv connectivity with areas 3a, 3b, 1, and 2).

These simplified connectivity strength graphs for representations (Fig. 4.7A) or cortical areas (Fig. 4.7B) are a good start to understanding relationships in connectivity strength throughout the sensorimotor network, but they provide an incomplete perspective. For example, connectivity between arm and hand representations may be stronger in motor areas and weaker in sensory areas. Likewise, connectivity between cortical areas may be stronger for some representations than others. In the current iteration, those distinctions cannot be made. Therefore, to attain a more complete perspective of connectivity strength throughout the network, we grouped seeds into nodes defined by both representation and cortical area (e.g., "M1 hand", Fig. 4.7C). Nodes were colored according to their representation and are spatially arranged to roughly match the arrangement of the microelectrode map. Connections with a strength <15% were omitted for visual simplicity. This graph revealed many principles of sensorimotor connectivity. For example, the strongest connectivity in the net-

work existed primarily between hand zones in somatosensory cortex. Connectivity between arm and hand zones was relatively weak in somatosensory cortex, but much stronger in PMd, PMv, and M1. Likewise, connectivity between trunk and leg zones appeared to be stronger in M1 than in somatosensory areas. Finally, the face network was well isolated from other representations in sensory cortex, but had some connectivity with arm and hand representations in premotor areas. Collectively, these observations indicated that connectivity between somatotopic representations was stronger in motor areas than in somatosensory areas.

4.4.9 Connectivity Between Arm and Hand Representations

Next, we examined in more detail the connectivity of the arm and hand representations throughout the sensorimotor network. Toward this objective, the average connectivity strength for M1 hand seeds is shown in Fig. 4.7E. Here, connectivity strength is normalized such that all bars add up to 100%. For simplicity, PMd and PMv are grouped into "PM" and sensory areas 3a, 3b, 1, and 2 are grouped into "S1". M1 hand seeds were equally connected to hand and arm zones in premotor cortex. Within M1, hand seeds were connected to hand zones only slightly more than to arm zones. However, in sensory cortex, M1 hand seeds were preferentially connected to S1 hand zones over S1 arm zones by a large margin. The same organization was present for seeds in all hand zones, not just M1 hand zones (Fig. 4.7F). Thus, connectivity between hand seeds and arm zones was weaker in S1 as compared to PM and M1. Arm seeds showed a surprisingly inverse pattern (Fig. 4.7G). In motor areas, arm seeds preferentially connected to arm zones over hand zones. In sensory cortex, however, arm seeds had a comparable amount of connectivity with hand and arm zones. Additionally, throughout sensorimotor cortex, arm seeds had more connectivity strength with face, trunk and leg/tail zones than hand seeds did.

These results suggest that there is a dichotomy in the connectivity motifs and separability of arm and hand networks between motor and sensory areas. Hand zones are for the most part only connected to hand and arm zones, with a general balance between the two in motor areas but with a strong preference toward hand zones in somatosensory areas. In contrast, arm zones are connected to a wider range of somatotopic representations throughout sensorimotor

cortex, and are more segregated from hand zones in motor areas than in somatosensory areas. This dichotomy points toward differing functional roles for arm and hand networks in sensorimotor cortex, consistent with previous findings concerning intrinsic M1 connections (Card and Gharbawie, 2020).

4.4.10 Somatosensory Input to Motor Areas

Another key feature of sensorimotor organization that may enable coordinated movements is the somatosensory input to cortical motor areas. Somatosensory signals serve as error correction signals during movement planning execution, without which motor performance suffers (Flesher et al., 2021; Monzée et al., 2003; Rothwell et al., 1982). Previous studies have identified corticocortical connectivity between somatosensory and motor areas, but the rules governing these connections are not clear. For example, which motor areas connect with proprioceptive or cutaneous somatosensory zones? To get at these rules, we first examined the connectivity strength of somatosensory hand zones (Fig. 4.7H). We chose the somatosensory hand representation because cortical borders are readily defined here from receptive field properties. Bars in this plot are normalized such that all bars sum to 100%. Indeed, we found a connectivity between the somatosensory and motor hand areas. Surprisingly, connectivity to M1 (13.5%) was stronger than connectivity to area 3a (10.7%, 2-sample t-test, $p<0.001$). Connectivity between somatosensory hand zones and premotor areas (PMv: 2.6%; PMd: 0.7%) was weaker, but still greater than zero, which was impressive given the distance between these cortical zones ($\sim$5-15 mm).

Next, we wished to gain insight into the cortical organization of cutaneous and proprioceptive input to M1. We therefore measured the connectivity of M1 with areas 3a, 3b, 1 and 2, individually (Fig. 4.7I). Areas 3b and 1 are primarily responsive to cutaneous stimuli, whereas area 3a is primarily responsive to proprioceptive stimuli. Area 2 responds to both cutaneous and proprioceptive stimuli. We found that area 3a and area 2 had the strongest connectivity with all motor areas. The connectivity from area 2 to motor areas is particularly noteworthy given that area 2 more distance from the motor areas than area 3a, 3b, and 1. Areas 3b and 1 had comparatively weaker connectivity with M1 and PMv, and no con-

nectivity with PMd. Thus, motor areas appear to be endowed with stronger proprioceptive input than cutaneous input. This result is intuitive when we consider that proprioception is central to movement execution.

4.5 Discussion

We investigated the network architecture of sensorimotor cortex in an effort to understand the organizational principles of sensorimotor corticocortical connectivity. Microelectrode mapping and resting state ISOI (RS-ISOI) allowed us to parcellate sensorimotor cortex and measure the connectivity of thousands of sites within it in vivo and at high spatial resolution. An unsupervised community detection approach was used to identify a hierarchy of communities that were well-aligned with somatotopy. A seed-based quantification identified key relationships between connectivity, somatotopy, and cortical areas. These findings converge to identify key features of sensorimotor network architecture.

4.5.1 Community Detection at the Columnar Scale

We measured the functional connectivity (FC) for thousands of sites throughout sensorimotor cortex to examine network architecture. However, network-wide trends are not readily accessible in a seed-based approach because the connectivity of each seed is independently considered. We therefore used a modularity-based community detection approach to overcome this hurdle and visualize structure at a network scale. Investigating the architecture of whole-brain networks with unsupervised community detection approaches is well-established for RS-fMRI data (e.g., Beckmann and Smith (2004); Beckmann et al. (2005); Calhoun and de Lacy (2017); Damoiseaux et al. (2006); Ferrarini et al. (2009); Kiviniemi et al. (2003)). However, RS-fMRI generally operates at a macroscale, where low contrast and spatial specificity obscure granular details of cortical architecture. Consequently, communities detected from RS-fMRI data are also at least at the macroscale, spanning large portions of the brain.

Applying community detection to RS-ISOI data therefore provides unique opportunity to examine network architecture at a granular scale.

The communities that we detected in the sensorimotor network ranged from 0.5 – 110 mm^2. These communities often overlapped individual somatotopic representations across multiple cortical areas. Furthermore, we found consistent spatial arrangement of communities overlapping key functional zones across animals. Although communities were quantified based on what cortical areas and representations they overlapped, it is important to note that community detection was in no way dependent upon the microelectrode map. Thus, RS-ISOI community detection can be used as a functional mapping tool to identify key functional zones in the absence of any microelectrode mapping. The microelectrode maps that we collected for each animal in this study were collectively composed of 1,211 sites (625 motor sites, 586 sensory sites), which took >50 hours (∼20-25 sites/hr) over the course of >25 experiments (∼50-60 sites/experiment) to collect. This massive commitment of time and energy could potentially be saved in future studies if key functional zones are identified using RS-ISOI community detection. Furthermore, obtaining functional maps with RS-ISOI community detection instead of microelectrode mapping is comparatively less invasive, as it does not require any electrode penetrations into the brain.

RS-ISOI community detection also has potentially exciting applications in brain areas beyond sensorimotor cortex. For example, this approach could similarly be used in conjunction with a seed-based approach to identify high-resolution functional maps in other low-order brain areas where connectivity is bound to somatotopy (e.g., V1). In higher-order brain regions that are difficult to map (e.g., association cortices), RS-ISOI community detection could be utilized to identify community structure at a higher resolution than is feasible with other resting state approaches.

4.5.2 Sensorimotor Connectivity is Functionally Organized

Our results shed light on key organizational principles that guide corticocortical connectivity throughout the sensorimotor cortex. We found that communities of interconnected pixels tended to overlap individual somatotopic representations across cortical areas. A

follow-up seed-based analysis allowed us to examine connectivity motifs between individual network nodes. One of our key findings was that most of the connectivity between sensory areas and M1 was restricted to sensory zones that were primarily proprioceptive. Connectivity between sensory and premotor areas was even more weighted toward proprioceptive sensory zones. However, dense connectivity within primary somatosensory cortex tightly bound proprioceptive and cutaneous zones to one another. These findings were consistent with corticocortical connectivity measured in several tracer studies (Dancause et al., 2006b; Gharbawie et al., 2010; Liao et al., 2013; Stepniewska et al., 1993, 2006). These corticocortical connections between proprioceptive sensory zones and cortical motor areas could serve as routes for error-correction signals to guide movement and movement planning (Flesher et al., 2021; Monzée et al., 2003; Rothwell et al., 1982).

We also observed that connectivity between somatotopic zones was typically stronger in motor and premotor areas than in sensory areas. For example, the sensory face zone was nearly completely isolated from other zones, but motor and premotor face zones had a small amount of connectivity to neighboring hand or arm zones. Likewise, sensory hand zones were mostly separate from other representations, but had considerable connectivity with arm zones in motor and premotor areas. Interestingly, the connectivity of arm zones showed a conflicting relationship, where crossover with hand zones was more pronounced in sensory zones than in motor or premotor zones. Within M1, the discrepancy between connectivity motifs for arm and hand zones was consistent with our findings from chapter 2 (Card and Gharbawie, 2020). Beyond M1, these results point toward functional differences between the arm and hand networks throughout sensorimotor cortex.

This dichotomy could be a result of how the microelectrode map is organized. The amount of cortical territory devoted to arm or hand representations differs between motor and sensory areas. In motor areas, arm and hand zones occupy comparable cortical territories. But in somatosensory zones the hand zone is considerably larger than the arm zone. Moreover, the hand and arm zones are contiguous and non-overlapping in somatosensory cortex, but more intermingled in motor areas. Thus, differences in connectivity between arm and hand zones that we observed could simply be a biproduct of the topographical organization of the sensorimotor network. In chapter 2 (Card and Gharbawie, 2020), we tackled

a similar question in M1 by comparing observed and expected (i.e., chance) connectivity profile of each site. This approach showed that within M1, connectivity of arm sites targeted arm zones at a rate above chance, and hand zones at a rate below chance. We intend to implement a similar analysis for the data presented here before we submit this study for publication. This analysis will allow us to objectively evaluate if the connectivity patterns reporter were mere reflections of the topographical organization of the microelectrode maps.

In summary, our results collectively identify a number of organizing principles for sensorimotor corticocortical connectivity: (1) all seeds had dense local connectivity in a 2-3mm radius, in addition to patchy connections beyond that radius, (2) connectivity binds like representations within and across cortical areas, (3) extent of connectivity between non-matching zones is dependent on cortical area, (4) connections between motor and sensory areas mostly targeted proprioceptive sensory zones. This network-level perspective sheds light on how sensory and motor cortical areas work together to generate skilled movements.

4.5.3 Validating Principles of Sensorimotor Connectivity

In a future analysis that we aim to conduct before this chapter is published, we would like to validate the accuracy of the principles of sensorimotor connectivity that we have identified. One way to accomplish this is with the same unsupervised community detection approach that we used to subdivide the network earlier in this study. We can use our identified connectivity pattern in conjunction with the microelectrode map to generate a simulated FC matrix for each animal. We can then feed this simulated FC matrix into the community detection algorithm. For comparison, we can also feed a randomized FC matrix into the community detection algorithm to generate randomized communities. If the resultant simulated communities are more similar to real detected communities than to randomized communities, then we can be confident that the principles of connectivity that we identified are key building blocks of the network architecture. Because the unsupervised community detection approach takes all connectivity data into account to generate communities, this approach is an excellent way validate our identified principles of sensorimotor connectivity.

4.5.4 Conclusions

We applied unsupervised and supervised analyses to RS-ISOI data to segment the sensorimotor network into meaningful subnetworks and identify the organizational principles of corticocortical connectivity. Consistent results from three animals showed that corticocortical connectivity in sensorimotor cortex was linked to the underlying somatotopy and cytoarchitecture, which is a pattern that is well established in other sensory areas. These results grant insight into how corticocortical connections in sensorimotor cortex may enable the coordination required to generate skilled movements.

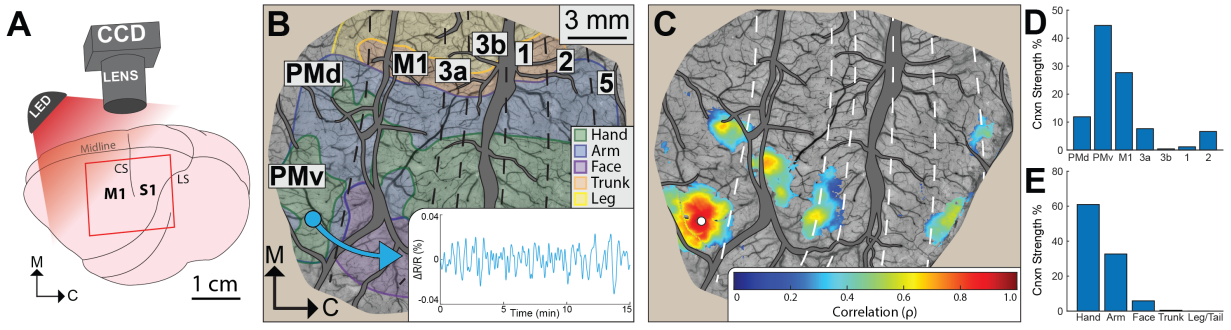

Figure 4.2: Functional connectivity maps measured from RS-ISOI. (A) Schematic of RS-ISOI experimental setup. A CCD is used to record spontaneous hemodynamic fluctuations from sensorimotor cortex under red illumination. (B) Optical image of cortex (528 nm illumination) with cortical borders and zones from microelectrode maps. Large blood vessels are masked in gray. Tan color around the perimeter masks resected dura and skull. Scale bar is same for (C). Seed (blue circle) is in the PMv hand zones. Inset shows the processed time course of reflectance change (ΔR/R%) measured from the seed in 1 RS-ISOI recording. (C) FC map for a PMv hand seed after averaging and statistical thresholding for significantly positive (one-tailed t-test, $p<0.001$) pixels from 13 RS-ISOI recordings. Seed location is same as (B). Color bar is correlation coefficient (ρ). (D) Weighted spatial quantification of the cortical areas overlapped by FC map in (C). (E) Weighted spatial quantification of the somatotopic representations overlapped by FC map in (C).

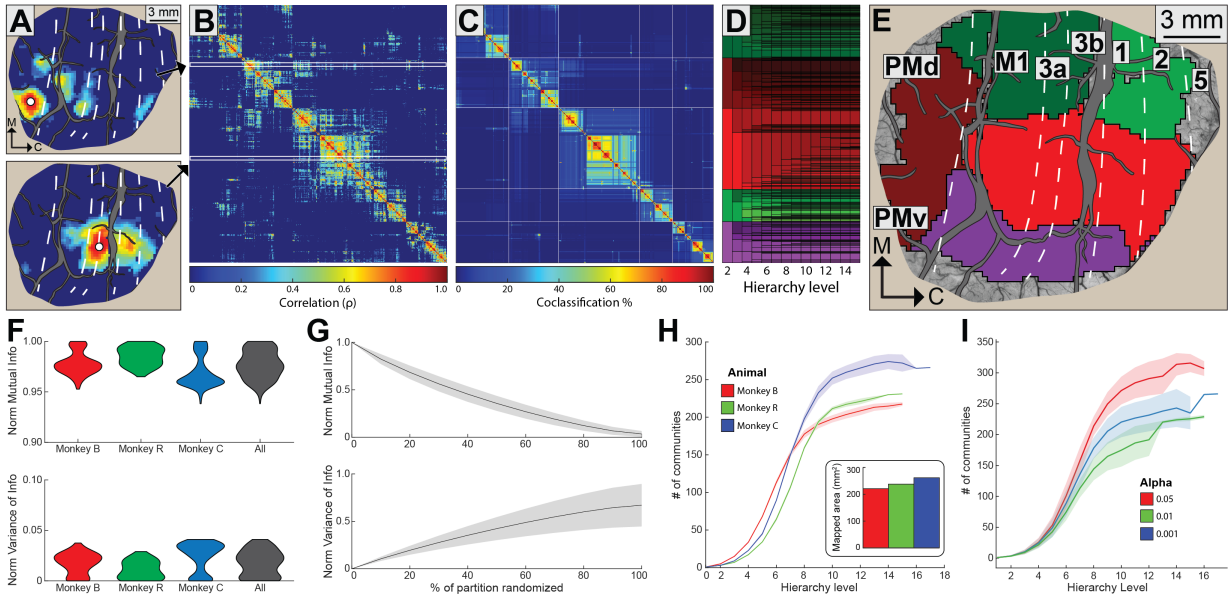

Figure 4.3: Community detection is consistent between iterations. (A) Examples of two FC maps (monkey B). Color bar of correlation coefficient (ρ) from (B) applies here. *Top.* FC map for a PMv hand seed. Same seed as in Fig. 4.2. Scale bar applies to both FC maps. *Bottom.* FC map for seed in the D2 representation of area 3b. (B) FC matrix (monkey B). Correlation coefficients (ρ, color bar) between any two pixels in the FOV are contained in this matrix. Matrix is organized such that each row or column is the FC map for a given seed. FC maps from (A) are located in the rows highlighted with white outlines. (C) Co-classification matrix that shows the probability (%, color bar) that any two pixels were grouped into the same community after 2000 community partitions with a varying resolution parameter (see methods). Row and column order is same as (B). Horizontal and vertical white lines divide the 5 communities in the most superficial hierarchy level (see D and E). (D) Hierarchy tree of community structure. Each column is a level of the hierarchy tree. Divisions within columns are individual communities. Communities in each level are subdivided in a statistically significant manner where possible. Subdivided communities are colored as shades of their parent community. (E) Community map for the most superficial hierarchy level (monkey B). Community colors are consistent with (D). (F) *Top.* Normalized mutual information (MI_n) of community partitions over multiple iterations of community detection. *Bottom.* Same analysis as above but with normalized variance of information (VI_n). High MI_n and low VI_n indicate that community detection generates stable community partitions iteration-to-iteration. (G). MI_n and VI_n between a community partition and a partially randomized version of itself. MIn increases and VI_n decreases as percent randomization increases. Line represents mean value and shaded area is ± 1 SD. (H) Number of communities as a function of hierarchy level, presented for each animal (mean $\pm$ SD). Inset shows total area of mapped cortical territory for each animal. (F) Number of communities detected at varying α thresholds for hierarchical consensus (mean $\pm$ SD).

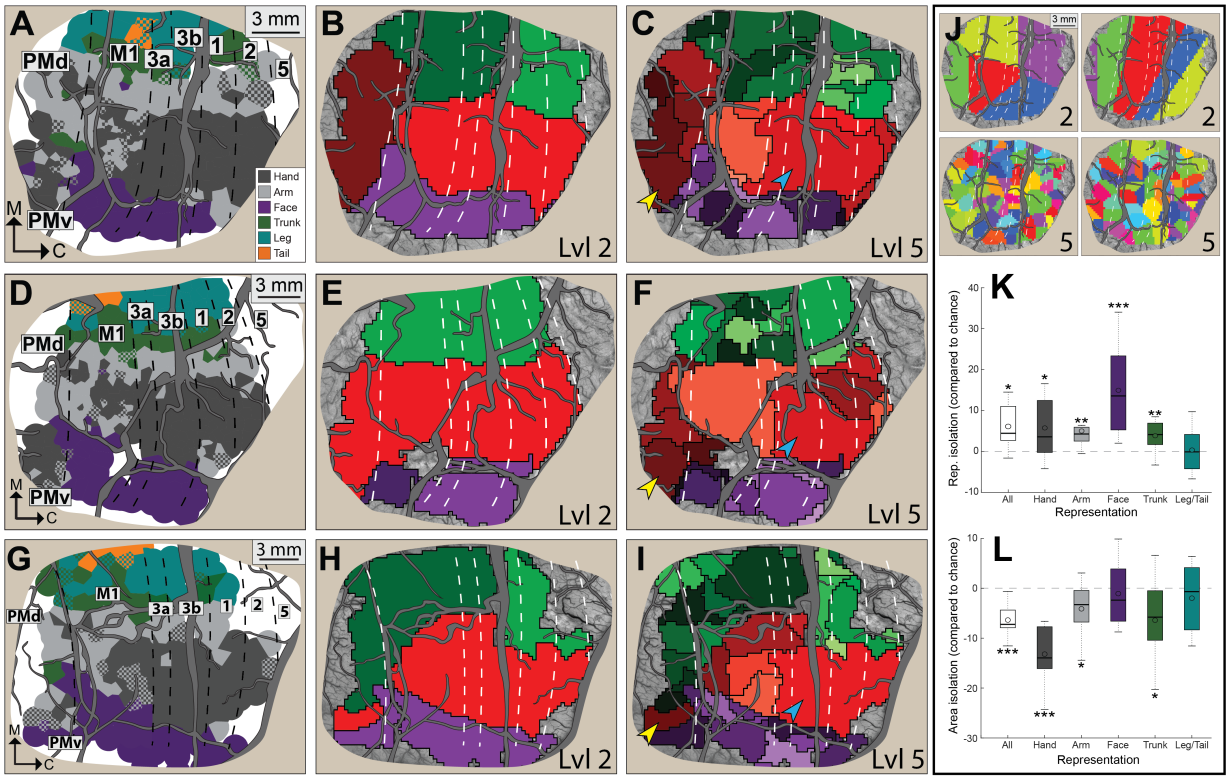

Figure 4.4: Communities are functionally bound and consistent between animals. (A) Map of somatotopic representations and cortical borders (dashed lines) obtained from microelectrode mapping (monkey B). Scale bar applies to (B-C). (B) Community map for hierarchy level 2. Communities were contiguous and appeared to follow the organization of the microelectrode map. Communities are colored to highlight consistencies between animals. Black outlines are community borders. Cortical borders are colored white here to enhance visibility. (C) Community map for hierarchy level 5. Communities are colored as shades of the color of their parent community. Yellow and cyan arrowheads point to PMv hand and somatosensory hand communities, respectively. (D-F) Same as (A-C), but for monkey R. (G-I) Same as (A-C) and (G-F), but for monkey C. (J) Randomly generated contiguous community partition maps (monkey B). Top. Randomized community maps for hierarchy level 2. Number of communities here matches the number of real communities in hierarchy level 2. Bottom. Randomized community maps for hierarchy level 5. (K) Somatotopic representational isolation for real communities compared to randomized communities. Analysis was repeated for subgroups of communities overlapping specific somatotopic representations according to the x-axis. Values above 0 indicate that real communities were isolated to individual somatotopic representations at a rate above chance (one-sample t-test, $*p < 0.05$, $**p < 0.01$, $***p < 0.001$). (L) Cortical area isolation of real communities compared to randomized communities. Values below 0 indicate that real communities span multiple cortical areas at a rate above chance (one-sample t-test, $*p < 0.05$, $**p < 0.01$, $***p < 0.001$).

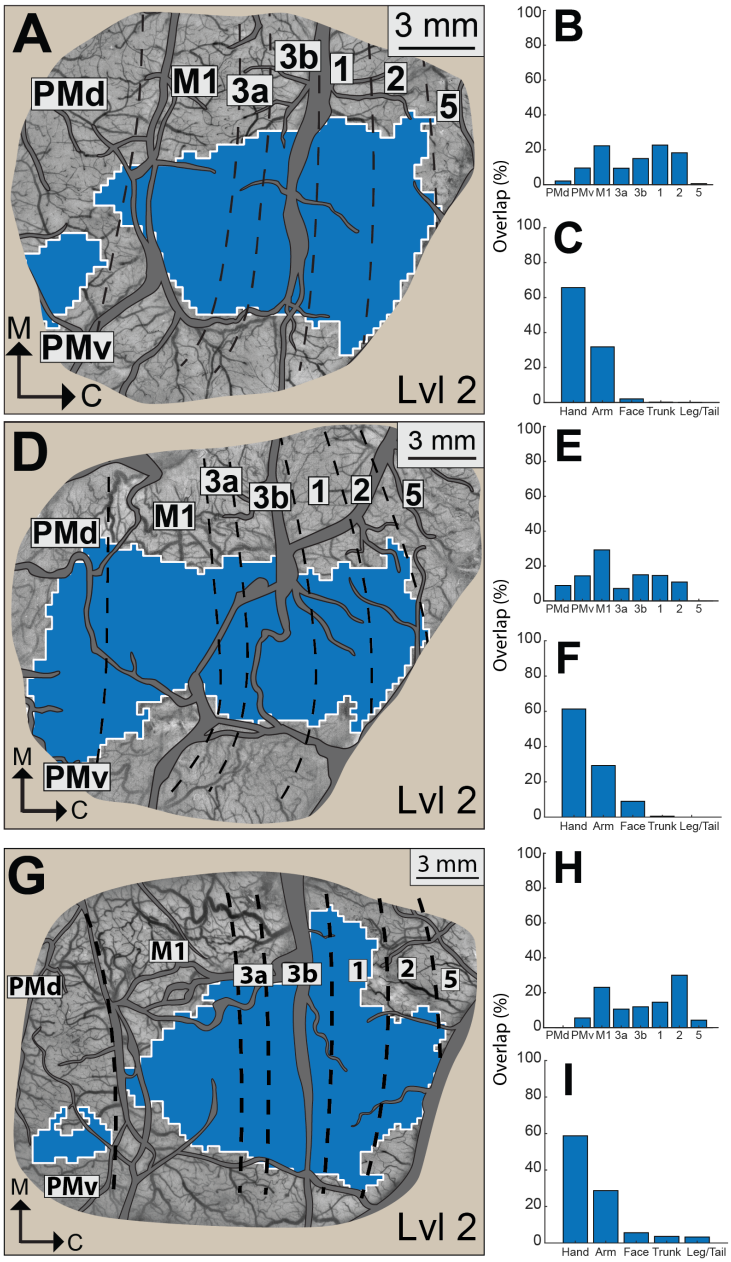

Figure 4.5: Network structure exists within negative correlations. (A) A community from community detection that was applied to an FC matrix with only negative correlations (monkey B). This community overlaps exclusively arm and hand zones. Hierarchy tree level 2. (B) Quantification of the cortical areas overlapped by the community in (A). All bars add up to 100%. (C) Quantification of the somatotopic representations overlapped by the community in (A). All bars add up to 100%. (D-F) Same as (A-C) but for monkey R. (G-I) Same as (A-C) and (D-F) but for monkey C.

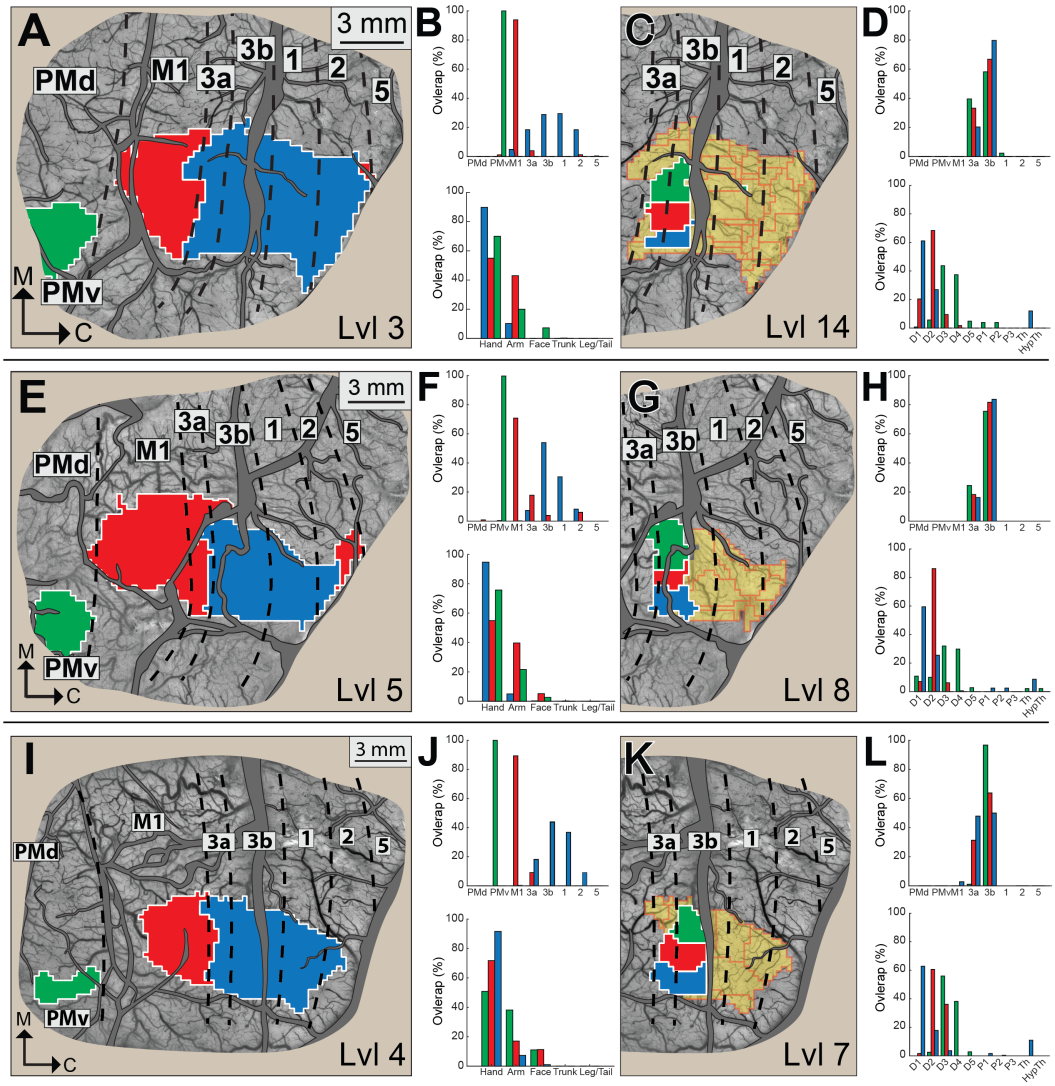

Figure 4.6: Key forelimb communities are spatially consistent across animals. (A) Largest communities overlapping hand zones in premotor cortex (green), M1 (red), and S1 (blue) at community hierarchy level 3 (monkey B). (B) Top. Cortical area overlap by each community from (A). Colors of bars are consistent with community colors. All bars of each color sum to 100%. Bottom. Somatotopic representation overlap by each community from (A). Conventions same as above. (C) Subcommunities of the blue somatosensory hand community from (A) in community hierarchy level 14. Highlighted communities (blue, red, green) are communities in area 3a/3b that mostly overlapped individual digit representations. All communities are shown in the background yellow with orange borders. (D) Overlap of highlighted communities with cortical areas and somatotopic representations. Conventions same as (B). (E-H) Same as (A-D), but for monkey R. Note differences in hierarchy level in the bottom-right of (E) and (G). (I-L) Same as (A-D) and (E-H), but for monkey C. Note differences in hierarchy level in the bottom-right of (I) and (L).

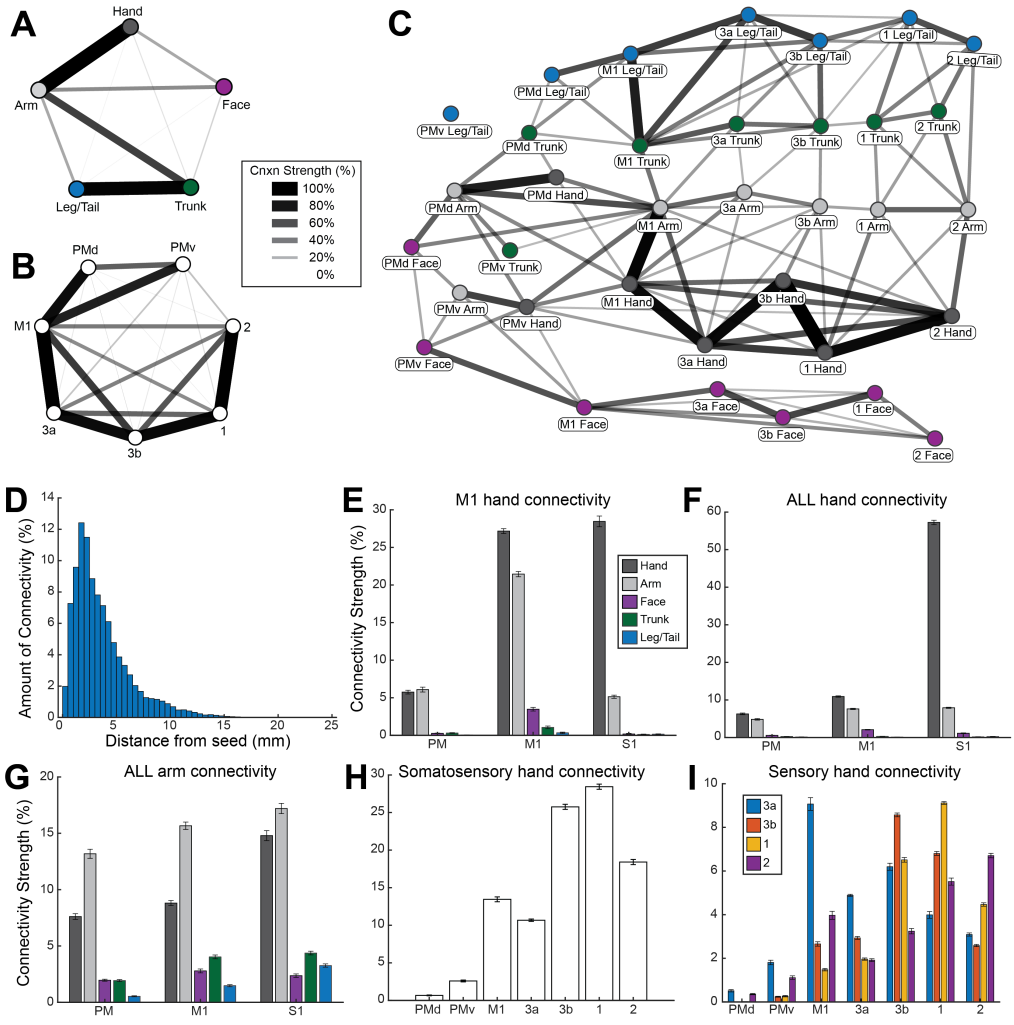

Figure 4.7: Connectivity strength throughout sensorimotor cortex. (A) Average connectivity strength between somatotopic representations for all animals. Line width and opacity represents connectivity strength according to the legend. Nodes (circles) are colored and labeled according to their representation. Connectivity strength is normalized such that the strongest connection in the network is 100%. (B) Same as A, but for cortical areas instead of representations. (C) Same as A and B, but for somatotopic representations segmented by cortical area. Nodes are arranged to roughly match the arrangement of the microelectrode map. Connections with <15% strength are removed for simplicity. (D) Average spatial distribution of connectivity for every seed in all animals (n = 8560). Roughly 50% of connections are within 3 mm of any seed. (E) Average connectivity strength for seeds in the M1 hand representation for all animals (n = 344). Error bars are ±1 SEM. Cortical areas are simplified on the x-axis; PMv and PMd are grouped into "PM"; areas 3a, 3b, 1 and 2 are grouped into "S1". Connectivity strength is normalized such that all bars add up to 100%. (F) Same as (E), but for seeds in the hand representation of any cortical area (n = 2339). (G) Same as (E), but for seeds in the arm representation of any cortical area (n = 1589). (H) Connectivity strength of the S1 hand representation, by cortical area. Same conventions as previous bar plots. (I) Similar to (H), but split by individual somatosensory cortical areas.

5.0 Summary, Limitations, and Future Directions

5.1 Summary

The goal of this dissertation was to identify the functional network architecture of sensorimotor cortex, which contributes to fine motor control. Toward this goal, I developed and benchmarked novel imaging approaches to measure and quantify corticocortical connectivity at high resolution *in vivo*. By measuring the connectivity for many sites throughout the squirrel monkey sensorimotor cortex and quantifying that connectivity in the context of functional maps, I identified relationships between connectivity, somatotopy, and cytoarchitecture. These results grant insight into the neural basis of fine motor control. The novel approaches utilized here overcame limitations of previous connectivity mapping techniques to answer questions about cortical network organization in primates that were otherwise impenetrable.

Previous studies have shown that ISOI can be used in ICMS-evoked (Brock et al., 2013; Friedman et al., 2020; Stepniewska et al., 2011) and resting state (Bauer et al., 2018; Kura et al., 2018; Vasireddi et al., 2016; Vazquez et al., 2014; White et al., 2011) paradigms to measure connectivity at a high spatial resolution. My findings in chapter 3 extend these results by demonstrating that RS-ISOI can reveal cortical connectivity at the columnar resolution in monkeys. I used EEG to quantify and identify the anesthetic state that was most conducive to high quality imaging. Furthermore, I benchmarked RS-ISOI and ICMS+ISOI against neuroanatomical tracers, the gold standard of connectivity mapping, to show that connectivity measured with these approaches is consistent with intrahemispheric monosynaptic connectivity. Benchmarking connectivity measured with ISOI against a well-established connectivity tracing approach was central to trusting that connectivity. A key advantage of the benchmarking approach used in chapter 3 was that comparisons between connectivity tracing approaches were made at matched cortical sites in the same animals. Within-animal comparisons were necessary to benchmark connectivity at the columnar scale due to small animal-to-animal variations in sensorimotor somatotopy (e.g., Fig. 4.1). To the best of my

knowledge, previous comparisons of effective or functional connectivity with neuroanatomical tracers in the primate brain have only been made between different animals, or with a curated repository (e.g., Allen Brain Atlas). My work in chapter 3 therefore serves as an original demonstration of direct correspondence between effective connectivity, functional connectivity, and anatomical connectivity in the primate brain. It also demonstrates the potential utility of ISOI-based approaches for studying cortical network architecture in primates.

The *in vivo* nature of ISOI enabled a longitudinal experimental approach, wherein somatotopy and connectivity were measured for each animal over the course of several experiments across months-years. This longitudinal approach was central to parcellating cortex with high resolution microelectrode mapping. Additionally, multiple experiments were required to measure effective connectivity at dozens of sites per animal, as well as to collect the number of RS-ISOI datasets necessary for averaging and statistical thresholding. Finally, neuroanatomical tracer studies were able to be conducted in the same animals after all other data was collected. Thus, the longitudinal design of these studies was vital to nearly every finding made.

My results identified connectivity profiles for individual sites in sensorimotor cortex that were consistent with those identified in previous studies. For example, connectivity measured at somatosensory sites with ICMS+ISOI in Chapter 2 or RS-ISOI in Chapter 3 corresponded with neuroanatomically traced connections (Liao et al., 2013; Négyessy et al., 2013). However, this work goes further by measuring connectivity for a large number of cortical sites throughout sensorimotor cortex and quantifying that connectivity in relation to somatotopy and cytoarchitecture. Measurement of connectivity for a large number of cortical sites (dozens with ICMS+ISOI, thousands with RS-ISOI) was necessary for identifying trends in connectivity. This approach allowed us to identify key organizational features of corticocortical connectivity throughout sensorimotor cortex. In summary, my results collectively identify a number of organizing principles for sensorimotor corticocortical connectivity: (1) All sites are densely connected to the surrounding 1-3 mm of cortex, and in most cases have additional patches of connectivity beyond that radius. (2) Connectivity is generally motivated by somatotopy first, and cytoarchitecture second. Sensorimotor networks bound

like representations across cortical borders. (3) Extent of connectivity between non-matching zones is dependent on cortical area. (4) Connections between motor and sensory areas mostly targeted proprioceptive sensory zones.

In conclusion, the work presented here identified organizational features of connectivity within sensorimotor cortex using novel imaging-based approaches to map connectivity in primates *in vivo*. This work enhances our understanding of the neural basis of fine motor control and establishes these novel imaging approaches as robust and powerful for studying functional cortical networks.

5.2 Limitations and Future Directions

Of course, the work presented here is not without its limitations. In many cases, these limitations set the stage for future research projects, some of which have already begun to be explored by myself and other members of the Gharbawie lab.

One major limitation of connectivity tracing with the imaging-based approaches adopted here are that the laminar organization of connectivity is not accessible through imaging alone. This limitation is significant given that the laminar organization of a connection determines its functional role (Felleman and Van Essen, 1991). In visual cortex, the identification of feedforward, feedback, and inhibitory connections has informed understanding of functional network architecture (Callaway, 2004). Other functional imaging approaches, such as fMRI, can in some cases localize signal to individual lamina (e.g., Chen et al. (2013)). However, ISOI cannot visualize signals deeper than $\sim$500 μm in cortex due to limits in the penetration depth of illumination. Even within the superficial 500 μm of cortex, ISOI cannot distinguish lamina. However, this limitation can be circumvented by using another approach to measure the laminar organization of connectivity identified with ISOI. One such approach is electrophysiology. Laminar recording probes can be used to measure neural activity at multiple contacts spanning the depth of cortex. In preliminary experiments, we have already begun to use this ISOI + electrophysiology approach to identify the functional role of corticocortical connections in sensorimotor cortex. After identifying connected cortical zones with RS-ISOI,

we place a laminar probe in each zone to simultaneously record spontaneous or evoked neural activity in each zone in an effort to identify the laminar organization of these connections. This information, when combined with this dissertation's findings concerning the organizational features of connectivity, will enhance our understanding of the neural basis of skilled movements.

Another limitation of ISOI that it is quite invasive in the implementation used in the present dissertation. Although it is considerably less invasive than neuroanatomical tracers, which require sacrificing an animal and histologically sectioning the brain to view labeled neurons, ISOI is still far more invasive than fMRI, which is non-invasive. Except in animals with thin skulls (e.g., mice, White et al. (2011)), ISOI requires a craniotomy, and typically a durotomy, to measure hemodynamic signals. This invasive nature disqualifies the application of ISOI in humans, except potentially in situations where the brain is already exposed for medical purposes in the operating room setting. In the work presented in this dissertation, durotomies were also performed on each squirrel monkey to reveal the cortical surface, which were necessary for microelectrode mapping. However, in recent preliminary work, we have successfully measured spontaneous and stimulus-evoked hemodynamic signals through the squirrel monkey dura with ISOI. We have also demonstrated in chapter 4 that RS-ISOI can be used in place of microelectrode mapping to identify certain functional zones. Combined, these findings pave the way for studying connectivity in the squirrel monkey cortex without needing to perform a durotomy, which is a significant reduction in the invasiveness of the approach.

One more limitation of ISOI is the field of view (FOV). Activity in subcortical structures cannot be measured with ISOI, and any future direction to remedy that limitation is difficult to imagine given the principles upon which ISOI operates. This limits applications of ISOI to studying cortical areas, unless paired with another approach that can access subcortical structures, such as electrophysiology or fMRI. Furthermore, cortex in sulci cannot be accessed with ISOI. We mostly avoided this issue by conducting our studies in squirrel monkeys, whose brains are relatively smooth. In this dissertation, the ISOI FOV included $\sim$20 x 25 mm of cortex at a resolution of 13 μm/pixel (74 px/mm), which was sufficient for studying sensorimotor cortex in a single hemisphere but may not be large enough for other

applications. The FOV size could be increased by using a different lens combination or a CCD with a larger sensor. However, this solution will reach a limit of usefulness when the curvature of the brain prevents the entire FOV from being in focus at once. To get around this problem, one could also use multiple cameras to record ISOI at once. This approach, if implemented properly, could enable measurement of hemodynamic signal of the entire cortex of both hemispheres at once, excluding any cortex in sulci.

An additional limitation of the work presented here is that it only provides a perspective of connectivity in the resting, anesthetized brain. This may limit the functional interpretations of some of our results. Although we demonstrated in chapter 3 that RS-ISOI and ICMS+ISOI are consistent with monosynaptic anatomical connectivity, the functional relevance of these connections may be more accessible in a behavioral context. Toward a behavioral context, we have collected some preliminary data wherein we recorded RS-ISOI in an awake (but sedated) macaque. Preliminary results suggest that this resting state data is just as promising as RS-ISOI data collected in squirrel monkeys under anesthesia. In future experiments, this approach can be extended to behaving macaques. Indeed, these types of experiments have already begun in the Gharbawie lab and others (Friedman et al., 2020). When combined with the data presented in this dissertation, behavioral applications of ISOI have the potential to bring more functional context to the sensorimotor network architecture described here.

In conclusion, the work presented in this dissertation is not without limitations. These limitations readily offer opportunities for new research directions, some of them already ongoing, that will expand our understanding of how connectivity throughout the brain achieves function.

Appendix A

RS-ISOI Functional Connectivity GUI

I developed a Matlab tool to visualize functional connectivity measured with RS-ISOI (Fig. A1). The graphical user interface (GUI) enables the user to visualize average functional connectivity (FC) at any cortical site within the field of view (e.g, Fig. A1A). The FC map may also be thresholded to only include statistically positive correlation values, as described in chapter 3. Moreover, functional connectivity maps are quantified according to their overlap with motor and somatosensory microelectrode maps, and that quantification is presented to the user (Fig. A1D). The present example shows data for monkey B, but data for other monkeys is accessible through the same tool. This tool provides a fast and responsive way for researchers to visualize the functional connectivity of any cortical site of interest. Connectivity profiles can therefore be quickly compared between multiple sites in the same animal, or between matched sites in different animals.

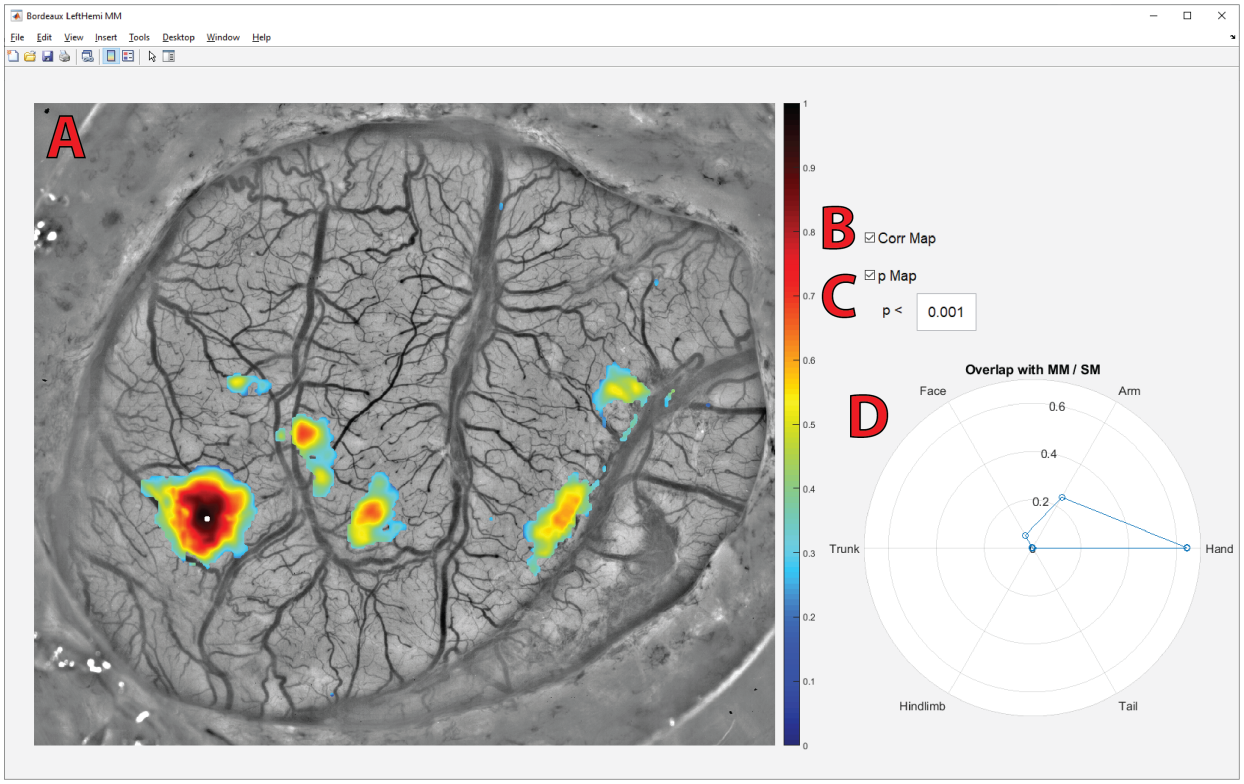

Figure A1: RS-ISOI Functional Connectivity GUI. (A) Functional connectivity of a PMv hand site (monkey B). Background image is a blood vessel map. Cortical borders and somatotopic representations are not shown here but can be seen in Fig. 3.3D. Seed (white dot) is the same as in Fig. 3.3D. Color is indicative of correlation (Pearson) value according to the color bar. Functional connectivity map is the average of 13 imaging runs. Only pixels with significantly positive correlations (one-tailed t-test, $p < 0.001$) are shown. The user can click on any pixel in the map to reveal the functional connectivity of a seed centered on that pixel. (B) Correlation map checkbox. If this box is checked (as in the present case), correlation values are shown. If it is unchecked, a binary map of significantly positive pixels is shown. (C) Significance threshold checkbox. If this box is checked (as in the present case) the functional connectivity map in (A) will be statistically thresholded at the p value shown in the adjacent box (currently 0.001). This p value can be changed by the user to view different statistical thresholds for the functional connectivity map. (D) Connectivity strength of the current functional connectivity map. This polar plot quantifies the strength with which the functional connectivity map overlaps each somatotopic represenation from the motor and somatosensory maps (e.g., Fig 3.1E).

Appendix B

RS-ISOI Community Detection GUI

I developed a Matlab tool to view RS-ISOI community detection results (Fig. B1). The graphical user interface (GUI) enables the user to visualize community detection results across a range of iterations and hierarchy levels. Although multiresolution consensus clustering (MRCC) and hierarchical clustering (HC, Jeub et al. (2018)) were used here, this GUI could be used to view the results of any community detection algorithm, provided that they are correctly formatted. The present example shows community detection results for monkey B, but additional GUIs could be opened to view community detection results for other monkeys. The user may select a community (Fig. B1C) to quantify the cortical areas (Fig. B1E) and somatotopic representations (Fig. B1F) overlapped by that community. Moreover, somatotopic overlap can be viewed at three levels of complexity to aid interpretation (radio buttons above Fig. B1F). Relationships between communities could also be examined, such as cosine similarity (CS) of the somatotopy overlapped by each community, average coclassification values of each pixels in community, and average functional connectivity between communities (Fig. B1D). These features proved to be invaluable as I examined community detection results and compared them across animals.

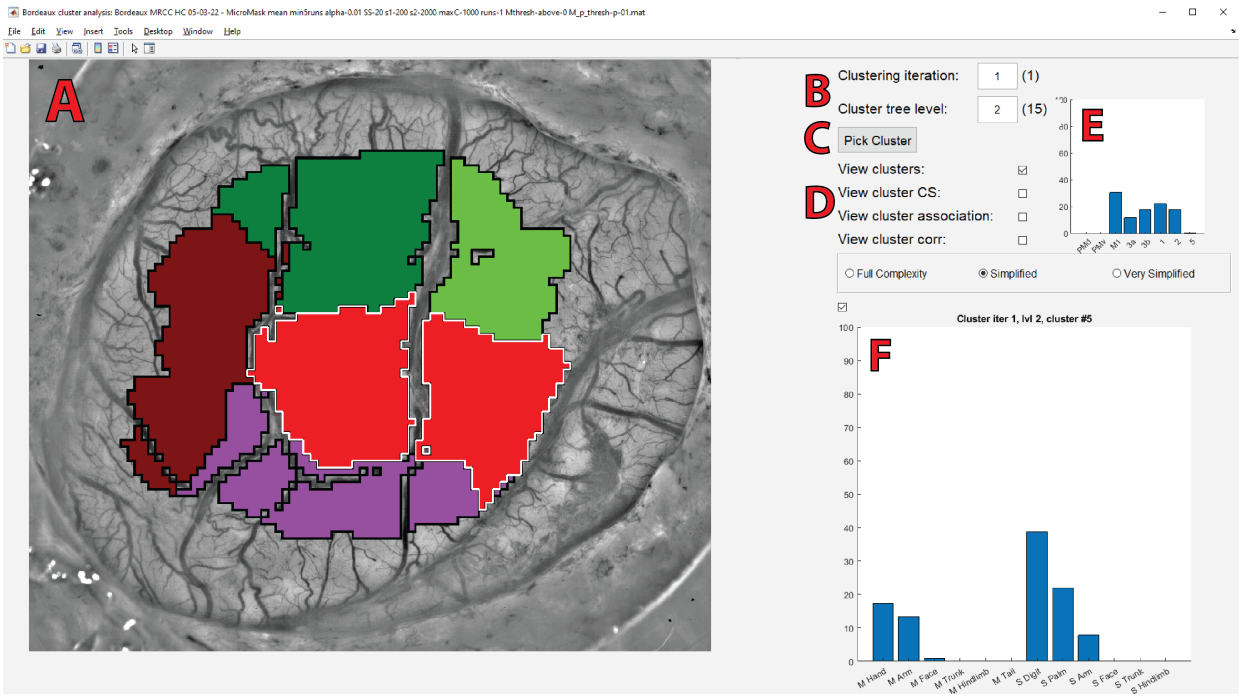

Figure B1: RS-ISOI Community Detection GUI. (A) Map of detected communities in hierarchy level 2 after running multiresolution consensus clustering (MRCC) and hierarchical clustering (HC) on averaged RS-ISOI data (monkey B). Same map as Fig. 4.3E. The five communities here are differentiated by color. The user may select any community to see which cortical areas (E) or somatotopic representations (F) it overlaps. The bright red community is outlined in white because it is currently selected by the user. (B) Community map selection. The user may specifiy which community detection iteration (currently only 1 is available) or hierarchy level (currently level 2 of 15 is selected) that they would like to view. (C) The user may click this button to select a new community to view cortical area and somatotopy overlap for. (D) Alternative view modes. Currently, the GUI is in cluster view mode. "View cluster CS" will enable visualization of the cosine similarity (CS) between somatotopy overlapped by each community. "View cluster association" will enable visualization of the average coclassification between pixels in each community. "View cluster corr" will enable visualization of the average functional connectivity between pixels in each community. (E) Cortical areas overlapped by the currently selected community. (F) Somatotopy overlapped by the currently selected community. The complexity of this bar plot can be changed using the radio buttons above. "Full complexity" will show community overlap with the most complex level of representations (e.g. Digit 1, Digit 2, etc.). "Very simplified" will simplify overlap to "Hand", "Arm", "Face", "Trunk", and "Leg/Tail" representations.

Bibliography

Yusuke Adachi, Takahiro Osada, Olaf Sporns, Takamitsu Watanabe, Teppei Matsui, Kentaro Miyamoto, and Yasushi Miyashita. Functional connectivity between anatomically unconnected areas is shaped by collective network-level effects in the macaque cortex. *Cerebral cortex (New York, N.Y. : 1991)*, 22(7):1586–92, jul 2012. ISSN 1460-2199. doi: 10.1093/cercor/bhr234. URL http://www.ncbi.nlm.nih.gov/pubmed/21893683.

R W Angel, W Alston, and H Garland. Functional relations between the manual and oculomotor control systems. *Experimental neurology*, 27(2):248–57, may 1970. ISSN 0014-4886. doi: 10.1016/0014-4886(70)90218-9. URL http://www.ncbi.nlm.nih.gov/pubmed/5424587.

Corson N. Areshenkoff, Joseph Y. Nashed, R Matthew Hutchison, Melina Hutchison, Ron Levy, Douglas J. Cook, Ravi S. Menon, Stefan Everling, and Jason P. Gallivan. Muting, not fragmentation, of functional brain networks under general anesthesia. *NeuroImage*, 231(January):117830, 2021. ISSN 1095-9572. doi: 10.1016/j.neuroimage.2021.117830. URL https://doi.org/10.1016/j.neuroimage.2021.117830http://www.ncbi.nlm.nih.gov/pubmed/33549746.

Amos Arieli, Doron Shoham, Rina Hildesheim, and Amiram Grinvald. Coherent spatiotemporal patterns of ongoing activity revealed by real-time optical imaging coupled with single-unit recording in the cat visual cortex. *Journal of neurophysiology*, 73(5):2072–93, may 1995. ISSN 0022-3077. doi: 10.1152/jn.1995.73.5.2072.

Vassiliki A Aroniadou and Asaf Keller. The patterns and synaptic properties of horizontal intracortical connections in the rat motor cortex. *Journal of neurophysiology*, 70(4):1553–69, oct 1993. ISSN 0022-3077. doi: 10.1152/jn.1993.70.4.1553. URL http://www.ncbi.nlm.nih.gov/pubmed/7904301.

Mary K L Baldwin, Dylan F. Cooke, and Leah Krubitzer. Intracortical Microstimulation Maps of Motor, Somatosensory, and Posterior Parietal Cortex in Tree Shrews (Tupaia belangeri) Reveal Complex Movement Representations. *Cerebral cortex (New York, N.Y. : 1991)*, 27(2):1439–1456, 2017. ISSN 1460-2199. doi: 10.1093/cercor/bhv329. URL http://www.ncbi.nlm.nih.gov/pubmed/26759478http://www.pubmedcentral.nih.gov/articlerender.fcgi?artid=PMC6075024.

Adam Q. Bauer, Andrew W. Kraft, Grant A. Baxter, Patrick W. Wright, Matthew D. Reisman, Annie R. Bice, Jasmine J. Park, Michael R. Bruchas, Abraham Z. Snyder, Jin-Moo Lee, and Joseph P. Culver. Effective Connectivity Measured Using Optogenetically Evoked Hemodynamic Signals Exhibits Topography Distinct from Resting State Functional Connectivity in the Mouse. *Cerebral cortex (New York, N.Y. : 1991)*, 28(1):370–386, 2018. ISSN 1460-2199. doi: 10.1093/

cercor/bhx298. URL http://www.ncbi.nlm.nih.gov/pubmed/29136125http://www.pubmedcentral.nih.gov/articlerender.fcgi?artid=PMC6057523.

Christian F Beckmann and Stephen M Smith. Probabilistic independent component analysis for functional magnetic resonance imaging. *IEEE transactions on medical imaging*, 23(2):137–52, feb 2004. ISSN 0278-0062. doi: 10.1109/TMI.2003.822821. URL https://linkinghub.elsevier.com/retrieve/pii/B9780444641489000193http://www.ncbi.nlm.nih.gov/pubmed/32977883http://www.ncbi.nlm.nih.gov/pubmed/14964560.

Christian F. Beckmann, Marilena DeLuca, Joseph T. Devlin, and Stephen M. Smith. Investigations into resting-state connectivity using independent component analysis. *Philosophical transactions of the Royal Society of London. Series B, Biological sciences*, 360(1457):1001–13, may 2005. ISSN 0962-8436. doi: 10.1098/rstb.2005.1634. URL https://royalsocietypublishing.org/doi/10.1098/rstb.2005.1634http://www.ncbi.nlm.nih.gov/pubmed/16087444http://www.pubmedcentral.nih.gov/articlerender.fcgi?artid=PMC1854918.

J W Belliveau, D N Kennedy, R C McKinstry, B R Buchbinder, R M Weisskoff, M S Cohen, J M Vevea, T J Brady, and B R Rosen. Functional mapping of the human visual cortex by magnetic resonance imaging. *Science (New York, N.Y.)*, 254(5032):716–9, nov 1991. ISSN 0036-8075. doi: 10.1126/science.1948051. URL https://www.jstor.org/stable/pdf/2879286.pdf?refreqid=excelsior%3Ad358e49b79bc1e58b0af4e5406eafd1ehttp://www.ncbi.nlm.nih.gov/pubmed/1948051.

Sliman J. Bensmaia, Peter V. Denchev, J. Francis Dammann, James C. Craig, and Steven S. Hsiao. The representation of stimulus orientation in the early stages of somatosensory processing. *Journal of Neuroscience*, 28(3):776–786, 2008. ISSN 02706474. doi: 10.1523/JNEUROSCI.4162-07.2008.

Rasmus M. Birn, Erin K. Molloy, Rémi Patriat, Taurean Parker, Timothy B. Meier, Gregory R. Kirk, Veena A. Nair, M. Elizabeth Meyerand, and Vivek Prabhakaran. The effect of scan length on the reliability of resting-state fMRI connectivity estimates. *NeuroImage*, 83:550–8, dec 2013. ISSN 1095-9572. doi: 10.1016/j.neuroimage.2013.05.099. URL http://dx.doi.org/10.1016/j.neuroimage.2013.05.099https://linkinghub.elsevier.com/retrieve/pii/S1053811913006010http://www.ncbi.nlm.nih.gov/pubmed/23747458http://www.pubmedcentral.nih.gov/articlerender.fcgi?artid=PMC4104183.

Bharat Biswal, F Z Yetkin, Victor M. Haughton, and James S. Hyde. Functional connectivity in the motor cortex of resting human brain using echo-planar MRI. *Magnetic resonance in medicine*, 34(4):537–41, oct 1995. ISSN 0740-3194. doi: 10.1002/mrm.1910340409. URL http://www.ncbi.nlm.nih.gov/pubmed/8524021.

Vincent D. Blondel, Jean-Loup Guillaume, Renaud Lambiotte, and Etienne Lefebvre. Fast unfolding of communities in large networks. *Journal of Statistical Mechanics: Theory and*

Experiment, 2008(10):P10008, oct 2008. ISSN 1742-5468. doi: 10.1088/1742-5468/2008/10/P10008. URL https://iopscience.iop.org/article/10.1088/1742-5468/2008/10/P10008.

S. Bohlhalter, C. Fretz, and B. Weder. Hierarchical versus parallel processing in tactile object recognition: A behavioural-neuroanatomical study of aperceptive tactile agnosia. *Brain*, 125(11):2537–2548, 2002. ISSN 00068950. doi: 10.1093/brain/awf245.

Tobias Bonhoeffer and Amiram Grinvald. Iso-orientation domains in cat visual cortex are arranged in pinwheel-like patterns. *Nature*, 353(6343):429–31, oct 1991. ISSN 0028-0836. doi: 10.1038/353429a0. URL http://www.ncbi.nlm.nih.gov/pubmed/1896085.

William H. Bosking, Ying Zhang, Brett Schofield, and David Fitzpatrick. Orientation Selectivity and the Arrangement of Horizontal Connections in Tree Shrew Striate Cortex. *The Journal of Neuroscience*, 17(6):2112–2127, mar 1997. ISSN 0270-6474. doi: 10.1523/JNEUROSCI.17-06-02112.1997. URL http://www.jneurosci.org/lookup/doi/10.1523/JNEUROSCI.17-06-02112.1997.

Andrea A. Brock, Robert M. Friedman, Reuben H. Fan, and Anna W. Roe. Optical imaging of cortical networks via intracortical microstimulation. *Journal of Neurophysiology*, 110 (11):2670–2678, dec 2013. ISSN 00223077. doi: 10.1152/jn.00879.2012. URL http://jn.physiology.org/cgi/doi/10.1152/jn.00879.2012.

Kathy Bruce and Irena Grofova. Notes on a light and electron microscopic double-labeling method combining anterograde tracing with Phaseolus vulgaris leucoagglutinin and retrograde tracing with cholera toxin subunit B. *Journal of Neuroscience Methods*, 45 (1-2):23–33, oct 1992. ISSN 01650270. doi: 10.1016/0165-0270(92)90040-K. URL https://linkinghub.elsevier.com/retrieve/pii/016502709290040K.

Randy L Buckner, Fenna M Krienen, and B T Thomas Yeo. Opportunities and limitations of intrinsic functional connectivity MRI. *Nature neuroscience*, 16(7):832–7, jul 2013. ISSN 1546-1726. doi: 10.1038/nn.3423. URL http://www.ncbi.nlm.nih.gov/pubmed/23799476.

Ed Bullmore and Olaf Sporns. Complex brain networks: graph theoretical analysis of structural and functional systems. *Nature reviews. Neuroscience*, 10(3):186–98, mar 2009. ISSN 1471-0048. doi: 10.1038/nrn2575. URL http://www.ncbi.nlm.nih.gov/pubmed/19190637http://www.nature.com/articles/nrn2575.

Vince D. Calhoun and Nina de Lacy. Ten Key Observations on the Analysis of Resting-state Functional MR Imaging Data Using Independent Component Analysis. *Neuroimaging clinics of North America*, 27(4):561–579, nov 2017. ISSN 1557-9867. doi: 10.1016/j.nic.2017.06.012. URL http://www.ncbi.nlm.nih.gov/pubmed/28985929http://www.pubmedcentral.nih.gov/articlerender.fcgi?artid=PMC5657522.

Edward M Callaway. Feedforward, feedback and inhibitory connections in primate visual cortex. *Neural Networks*, 17(5-6):625–632, jun 2004. ISSN 08936080. doi: 10.1016/

j.neunet.2004.04.004. URL http://www.ncbi.nlm.nih.gov/pubmed/15288888https://linkinghub.elsevier.com/retrieve/pii/S0893608004000887.

C. Capaday, H. Devanne, Louise Bertrand, and Brigitte A. Lavoie. Intracortical connections between motor cortical zones controlling antagonistic muscles in the cat: A combined anatomical and physiological study. *Experimental Brain Research*, 120(2):223–232, may 1998. ISSN 00144819. doi: 10.1007/s002210050396.

Charles Capaday, Christian Ethier, Laurent Brizzi, Attila Sik, Carl van Vreeswijk, and Denis Gingras. On the nature of the intrinsic connectivity of the cat motor cortex: Evidence for a recurrent neural network topology. *Journal of Neurophysiology*, 102(4):2131–2141, oct 2009. ISSN 00223077. doi: 10.1152/jn.91319.2008.

Charles Capaday, Carl van Vreeswijk, Christian Ethier, Jesper Ferkinghoff-Borg, and Doug Weber. Neural mechanism of activity spread in the cat motor cortex and its relation to the intrinsic connectivity. *Journal of Physiology*, 589(10):2515–2528, may 2011. ISSN 00223751. doi: 10.1113/jphysiol.2011.206938.

Nicholas S. Card and Omar A. Gharbawie. Principles of Intrinsic Motor Cortex Connectivity in Primates. *The Journal of neuroscience : the official journal of the Society for Neuroscience*, 40(22):4348–4362, 2020. ISSN 1529-2401. doi: 10.1523/JNEUROSCI.0003-20.2020. URL http://www.ncbi.nlm.nih.gov/pubmed/32327531http://www.pubmedcentral.nih.gov/articlerender.fcgi?artid=PMC7252484.

Nicholas S Card and Omar A Gharbawie. Cortical connectivity is embedded in resting state at columnar resolution. *Progress in neurobiology*, 213(December 2021):102263, mar 2022. ISSN 1873-5118. doi: 10.1016/j.pneurobio.2022.102263. URL https://doi.org/10.1016/j.pneurobio.2022.102263https://linkinghub.elsevier.com/retrieve/pii/S0301008222000491http://www.ncbi.nlm.nih.gov/pubmed/35292269http://www.pubmedcentral.nih.gov/articlerender.fcgi?artid=PMC9080903.

Allen W. Chan, Majid H. Mohajerani, Jeffrey M. LeDue, Yu Tian Wang, and Timothy H. Murphy. Mesoscale infraslow spontaneous membrane potential fluctuations recapitulate high-frequency activity cortical motifs. *Nature Communications*, 6(1):7738, nov 2015. ISSN 2041-1723. doi: 10.1038/ncomms8738. URL http://www.ncbi.nlm.nih.gov/pubmed/26190168http://www.pubmedcentral.nih.gov/articlerender.fcgi?artid=PMC5101061http://www.nature.com/articles/ncomms8738.

Gang Chen, Feng Wang, John C. Gore, and Anna W. Roe. Layer-specific BOLD activation in awake monkey V1 revealed by ultra-high spatial resolution functional magnetic resonance imaging. *NeuroImage*, 64(1):147–55, jan 2013. ISSN 1095-9572. doi: 10.1016/j.neuroimage.2012.08.060. URL http://www.ncbi.nlm.nih.gov/pubmed/22960152http://www.pubmedcentral.nih.gov/articlerender.fcgi?artid=PMC3508288.

Kwanghun Chung and Karl Deisseroth. CLARITY for mapping the nervous system. *Nature Methods*, 10(6):508–513, 2013. ISSN 15487091. doi: 10.1038/nmeth.2481.

D Cordes, V M Haughton, K Arfanakis, J D Carew, P A Turski, C H Moritz, M A Quigley, and M E Meyerand. Frequencies contributing to functional connectivity in the cerebral cortex in "resting-state" data. *AJNR. American journal of neuroradiology*, 22(7):1326–33, aug 2001. ISSN 0195-6108. doi: 10.1007/s10854-014-1833-2. URL http://www.ncbi.nlm.nih.gov/pubmed/11498421http://www.pubmedcentral.nih.gov/articlerender.fcgi?artid=PMC7975218.

J. S. Damoiseaux, S A R B Rombouts, F. Barkhof, P. Scheltens, C. J. Stam, S. M. Smith, and C. F. Beckmann. Consistent resting-state networks across healthy subjects. *Proceedings of the National Academy of Sciences of the United States of America*, 103(37):13848–53, sep 2006. ISSN 0027-8424. doi: 10.1073/pnas.0601417103. URL http://www.ncbi.nlm.nih.gov/pubmed/16945915http://www.pubmedcentral.nih.gov/articlerender.fcgi?artid=PMC1564249.

Numa Dancause, Scott Barbay, Shawn B. Frost, Erik J. Plautz, Mihai Popescu, Philip M. Dixon, Ann M. Stowe, Kathleen M. Friel, and Randolph J. Nudo. Topographically Divergent and Convergent Connectivity between Premotor and Primary Motor Cortex. *Cerebral Cortex*, 16(8):1057–1068, aug 2006a. ISSN 1460-2199. doi: 10.1093/cercor/bhj049. URL http://academic.oup.com/cercor/article/16/8/1057/455347/Topographically-Divergent-and-Convergent.

Numa Dancause, Scott Barbay, Shawn B. Frost, Erik J. Plautz, Ann M. Stowe, Kathleen M. Friel, and Randolph J. Nudo. Ipsilateral connections of the ventral premotor cortex in a new world primate. *The Journal of comparative neurology*, 495(4):374–90, apr 2006b. ISSN 0021-9967. doi: 10.1002/cne.20875. URL http://www.ncbi.nlm.nih.gov/pubmed/16485282http://www.pubmedcentral.nih.gov/articlerender.fcgi?artid=PMC2583355.

Numa Dancause, Vanja Duric, Scott Barbay, Shawn B. Frost, Antonis Stylianou, and Randolph J. Nudo. An additional motor-related field in the lateral frontal cortex of squirrel monkeys. *Cerebral cortex (New York, N.Y. : 1991)*, 18 (12):2719–28, dec 2008. ISSN 1460-2199. doi: 10.1093/cercor/bhn050. URL http://www.ncbi.nlm.nih.gov/pubmed/18424778http://www.pubmedcentral.nih.gov/articlerender.fcgi?artid=PMC2583161.

Marco Davare, Roger Lemon, and Etienne Olivier. Selective modulation of interactions between ventral premotor cortex and primary motor cortex during precision grasping in humans. *Journal of Physiology*, 586(11):2735–2742, 2008. ISSN 00223751. doi: 10.1113/jphysiol.2008.152603.

Melvin Dea, Adjia Hamadjida, Guillaume Elgbeili, Stephan Quessy, and Numa Dancause. Different Patterns of Cortical Inputs to Subregions of the Primary Motor Cortex Hand Representation in Cebus apella. *Cerebral cortex (New York, N.Y. : 1991)*, 26(4):1747–61, apr 2016. ISSN 1460-2199. doi: 10.1093/cercor/bhv324. URL http://www.ncbi.nlm.nih.gov/pubmed/26966266http://www.pubmedcentral.nih.gov/articlerender.fcgi?artid=PMC4785954.

Anna Devor, Andrew K. Dunn, Mark L. Andermann, Istvan Ulbert, David A. Boas, and Anders M. Dale. Coupling of total hemoglobin concentration, oxygenation, and neural activity in rat somatosensory cortex. *Neuron*, 39(2):353–9, jul 2003. ISSN 0896-6273. doi: 10.1016/s0896-6273(03)00403-3. URL http://www.ncbi.nlm.nih.gov/pubmed/12873390.

John P. Donoghue, S. Leibovic, and J.N. N. Sanes. Organization of the forelimb area in squirrel monkey motor cortex: representation of digit, wrist, and elbow muscles. *Experimental Brain Research*, 89(1):1–19, 1992. ISSN 00144819. doi: 10.1007/BF00228996.

Rodney J. Douglas and Kevan A.C. Martin. Neuronal Circuits of the Neocortex. *Annual Review of Neuroscience*, 27(1):419–451, 2004. ISSN 0147-006X. doi: 10.1146/annurev.neuro.27.070203.144152. URL http://www.annualreviews.org/doi/10.1146/annurev.neuro.27.070203.144152.

Richard P. Dum and Peter L. Strick. Frontal lobe inputs to the digit representations of the motor areas on the lateral surface of the hemisphere. *The Journal of neuroscience : the official journal of the Society for Neuroscience*, 25(6):1375–86, feb 2005. ISSN 1529-2401. doi: 10.1523/JNEUROSCI.3902-04.2005. URL http://www.jneurosci.org/cgi/doi/10.1523/JNEUROSCI.3902-04.2005http://www.ncbi.nlm.nih.gov/pubmed/15703391http://www.pubmedcentral.nih.gov/articlerender.fcgi?artid=PMC6726000.

Leeland B. Ekstrom, Pieter R. Roelfsema, John T. Arsenault, Giorgio Bonmassar, and Wim Vanduffel. Bottom-up dependent gating of frontal signals in early visual cortex. *Science*, 321(5887):414–417, jul 2008. ISSN 00368075. doi: 10.1126/science.1153276.

Pei Chun Fang, Neeraj Jain, and Jon H. Kaas. Few intrinsic connections cross the hand-face border of area 3b of new world monkeys. *Journal of Comparative Neurology*, 454(3):310–319, 2002. ISSN 00219967. doi: 10.1002/cne.10433.

Daniel J Felleman and David C Van Essen. Distributed hierachical processing in the primate cerebral cortex. *Cerebral Cortex*, 1(1):1–47, 1991. ISSN 1047-3211. doi: 10.1093/cercor/1.1.1.

Isabelle Ferezou, Florent Haiss, Luc J. Gentet, Rachel Aronoff, Bruno Weber, and Carl C H Petersen. Spatiotemporal dynamics of cortical sensorimotor integration in behaving mice. *Neuron*, 56(5):907–23, dec 2007. ISSN 0896-6273. doi: 10.1016/j.neuron.2007.10.007. URL http://www.ncbi.nlm.nih.gov/pubmed/18054865.

Luca Ferrarini, Ilya M. Veer, Evelinda Baerends, Marie-José van Tol, Remco J. Renken, Nic J A van der Wee, Dirk J. Veltman, André Aleman, Frans G. Zitman, Brenda W J H Penninx, Mark A van Buchem, Johan H C Reiber, Serge A R B Rombouts, and Julien Milles. Hierarchical functional modularity in the resting-state human brain. *Human brain mapping*, 30(7):2220–31, jul 2009. ISSN 1097-0193. doi: 10.1002/hbm.20663. URL http://www.ncbi.nlm.nih.gov/pubmed/18830955http://www.pubmedcentral.nih.gov/articlerender.fcgi?artid=PMC6871119.

Sharlene N. Flesher, John E. Downey, Jeffrey M. Weiss, Christopher L. Hughes, Angelica J. Herrera, Elizabeth C. Tyler-Kabara, Michael L. Boninger, Jennifer L. Collinger, and Robert A. Gaunt. A brain-computer interface that evokes tactile sensations improves robotic arm control. *Science*, 372(6544):831–836, 2021. ISSN 10959203. doi: 10.1126/science.abd0380.

Michael D. Fox and Marcus E. Raichle. Spontaneous fluctuations in brain activity observed with functional magnetic resonance imaging. *Nature Reviews Neuroscience*, 8(9):700–711, sep 2007. ISSN 1471-003X. doi: 10.1038/nrn2201. URL http://www.ncbi.nlm.nih.gov/pubmed/17704812http://www.nature.com/articles/nrn2201.

Robert M. Friedman, Katherine A. Morone, Omar A. Gharbawie, and Anna Wang Roe. Mapping mesoscale cortical connectivity in monkey sensorimotor cortex with optical imaging and microstimulation. *Journal of Comparative Neurology*, 528(17):3095–3107, dec 2020. ISSN 0021-9967. doi: 10.1002/cne.24918. URL https://onlinelibrary.wiley.com/doi/10.1002/cne.24918.

K. C. Gatter, J J Sloper, and T. P.S. Powell. The intrinsic connections of the cortex of area 4 of the monkey, sep 1978. ISSN 00068950. URL https://academic.oup.com/brain/article-lookup/doi/10.1093/brain/101.3.513.

Omar A. Gharbawie, Iwona Stepniewska, Mark J Burish, and Jon H. Kaas. Thalamocortical connections of functional zones in posterior parietal cortex and frontal cortex motor regions in New World monkeys. *Cerebral cortex (New York, N.Y. : 1991)*, 20(10):2391–410, oct 2010. ISSN 1460-2199. doi: 10.1093/cercor/bhp308. URL http://www.ncbi.nlm.nih.gov/pubmed/20080929http://www.pubmedcentral.nih.gov/articlerender.fcgi?artid=PMC2936798.

Omar A. Gharbawie, Iwona Stepniewska, Huixin Qi, and Jon H. Kaas. Multiple parietal-frontal pathways mediate grasping in macaque monkeys. *The Journal of neuroscience : the official journal of the Society for Neuroscience*, 31(32):11660–77, aug 2011. ISSN 1529-2401. doi: 10.1523/JNEUROSCI.1777-11.2011. URL http://www.ncbi.nlm.nih.gov/pubmed/21832196http://www.pubmedcentral.nih.gov/articlerender.fcgi?artid=PMC3166522.

C. Ghez, J. Gordon, and M. F. Ghilardi. Impairments of reaching movements in patients without proprioception. II. Effects of visual information on accuracy. *Journal of Neurophysiology*, 73(1):361–372, 1995. ISSN 00223077. doi: 10.1152/jn.1995.73.1.361.

Charles D. Gilbert and Torsten N. Wiesel. Morphology and intracortical projections of functionally characterised neurones in the cat visual cortex, 1979. ISSN 00280836.

Charles D. Gilbert and Torsten N. Wiesel. Columnar specificity of intrinsic horizontal and corticocortical connections in cat visual cortex. *Journal of Neuroscience*, 9(7):2432–2422, 1989. ISSN 02706474. doi: 10.1523/jneurosci.09-07-02432.1989.

Moshe Godschalk, Andrew R. Mitz, Berber van Duin, and Hans van der Burga. Somatotopy of monkey premotor cortex examined with microstimulation. *Neuroscience Research*, 23 (3):269–279, 1995. ISSN 01680102. doi: 10.1016/0168-0102(95)00950-7.

J. Gordon, M. F. Ghilardi, and C. Ghez. Impairments of reaching movements in patients without proprioception. I. Spatial errors. *Journal of neurophysiology*, 73(1):347–60, jan 1995. ISSN 0022-3077. doi: 10.1152/jn.1995.73.1.347. URL `http://www.ncbi.nlm.nih.gov/pubmed/7714577`.

H. J. J. Gould, C. G. G. Cusick, T. P. P. Pons, and J. H. H. Kaas. The relationship of corpus callosum connections to electrical stimulation maps of motor, supplementary motor, and the frontal eye fields in owl monkeys. *Journal of Comparative Neurology*, 247(3):297–325, 1986. ISSN 10969861. doi: 10.1002/cne.902470303.

Michael S.A. Graziano, Charlotte S.R. Taylor, and Tirin Moore. Complex movements evoked by microstimulation of precentral cortex. *Neuron*, 34(5):841–851, 2002. ISSN 08966273. doi: 10.1016/S0896-6273(02)00698-0.

Michael D Greicius, Kaustubh Supekar, Vinod Menon, and Robert F Dougherty. Resting-state functional connectivity reflects structural connectivity in the default mode network. *Cerebral cortex (New York, N.Y. : 1991)*, 19(1):72–8, jan 2009. ISSN 1460-2199. doi: 10.1093/cercor/bhn059. URL `http://www.ncbi.nlm.nih.gov/pubmed/18403396http://www.pubmedcentral.nih.gov/articlerender.fcgi?artid=PMC2605172`.

Piercesare Grimaldi, Kadharbatcha S. Saleem, and Doris Tsao. Anatomical Connections of the Functionally Defined "Face Patches" in the Macaque Monkey. *Neuron*, 90(6):1325–1342, jun 2016. ISSN 08966273. doi: 10.1016/j.neuron.2016.05.009. URL `https://linkinghub.elsevier.com/retrieve/pii/S0896627316301696`.

Amiram Grinvald, Edmund E. Lieke, Ron D. Frostig, and Rina Hildesheim. Cortical point-spread function and long-range lateral interactions revealed by real-time optical imaging of macaque monkey primary visual cortex. *Journal of Neuroscience*, 14(5 I):2545–2568, may 1994. ISSN 02706474. doi: 10.1523/jneurosci.14-05-02545.1994.

Amiram Grinvald, Hamutal Slovin, and Ivo Vanzetta. Non-invasive visualization of cortical columns by fMRI. *Nature neuroscience*, 3(2):105–7, feb 2000. ISSN 1097-6256. doi: 10.1038/72045. URL `http://www.ncbi.nlm.nih.gov/pubmed/10649563`.

Patric Hagmann, Leila Cammoun, Xavier Gigandet, Reto Meuli, Christopher J. Honey, Van J Wedeen, and Olaf Sporns. Mapping the structural core of human cerebral cortex. *PLoS biology*, 6(7):e159, jul 2008. ISSN 1545-7885. doi: 10.1371/journal.pbio.0060159. URL `http://www.ncbi.nlm.nih.gov/pubmed/18597554http://www.pubmedcentral.nih.gov/articlerender.fcgi?artid=PMC2443193`.

Adjia Hamadjida, Melvin Dea, Joan Deffeyes, Stephan Quessy, and Numa Dancause. Parallel Cortical Networks Formed by Modular Organization of Primary Motor Cortex Outputs.

Current biology : CB, 26(13):1737–1743, 2016. ISSN 1879-0445. doi: 10.1016/j.cub.2016.04.068. URL http://www.ncbi.nlm.nih.gov/pubmed/27322001.

Yaoyao Hao, Alexa Riehle, and Thomas G. Brochier. Mapping horizontal spread of activity in monkey motor cortex using single pulse microstimulation. *Frontiers in Neural Circuits*, 10 (DEC):1–16, 2016. ISSN 16625110. doi: 10.3389/fncir.2016.00104. URL http://journal.frontiersin.org/article/10.3389/fncir.2016.00104/full.

S Q He, R P Dum, and P L Strick. Topographic organization of corticospinal projections from the frontal lobe: motor areas on the lateral surface of the hemisphere. *The Journal of neuroscience : the official journal of the Society for Neuroscience*, 13(3): 952–80, mar 1993. ISSN 0270-6474. doi: 10.1523/JNEUROSCI.13-03-00952.1993. URL http://www.jneurosci.org/content/15/5/3284.long%5Cnpapers://9d5f8f0b-0f0b-459c-b067-2a21bce198bb/Paper/p2495http://www.ncbi.nlm.nih.gov/pubmed/7680069http://www.pubmedcentral.nih.gov/articlerender.fcgi?artid=PMC6576595.

S Q He, R P Dum, and P L Strick. Topographic organization of corticospinal projections from the frontal lobe: motor areas on the medial surface of the hemisphere. *The Journal of neuroscience : the official journal of the Society for Neuroscience*, 15(5 Pt 1):3284–306, may 1995. ISSN 0270-6474. URL http://www.ncbi.nlm.nih.gov/pubmed/7538558http://www.pubmedcentral.nih.gov/articlerender.fcgi?artid=PMC6578253.

C. J. Honey, O. Sporns, L. Cammoun, X. Gigandet, J. P. Thiran, R. Meuli, and P. Hagmann. Predicting human resting-state functional connectivity from structural connectivity. *Proceedings of the National Academy of Sciences of the United States of America*, 106(6):2035–40, feb 2009. ISSN 1091-6490. doi: 10.1073/pnas.0811168106. URL http://www.ncbi.nlm.nih.gov/pubmed/19188601http://www.pubmedcentral.nih.gov/articlerender.fcgi?artid=PMC2634800.

Yuki Hori, David J. Schaeffer, Kyle M. Gilbert, Lauren K. Hayrynen, Justine C. Cléry, Joseph S. Gati, Ravi S. Menon, and Stefan Everling. Comparison of resting-state functional connectivity in marmosets with tracer-based cellular connectivity. *NeuroImage*, 204 (September 2019):116241, jan 2020a. ISSN 10538119. doi: 10.1016/j.neuroimage.2019.116241. URL https://linkinghub.elsevier.com/retrieve/pii/S1053811919308328.

Yuki Hori, David J. Schaeffer, Kyle M. Gilbert, Lauren K. Hayrynen, Justine C. Cléry, Joseph S. Gati, Ravi S. Menon, and Stefan Everling. Altered Resting-State Functional Connectivity Between Awake and Isoflurane Anesthetized Marmosets. *Cerebral cortex (New York, N.Y. : 1991)*, 30(11):5943–5959, 2020b. ISSN 1460-2199. doi: 10.1093/cercor/bhaa168. URL http://www.ncbi.nlm.nih.gov/pubmed/32556184http://www.pubmedcentral.nih.gov/articlerender.fcgi?artid=PMC7899065.

Henrietta Howells, Luciano Simone, Elena Borra, Luca Fornia, Gabriella Cerri, and Giuseppe Luppino. Reproducing macaque lateral grasping and oculomotor networks using resting state functional connectivity and diffusion tractography. *Brain structure and*

function, 225(8):2533–2551, nov 2020. ISSN 1863-2661. doi: 10.1007/s00429-020-02142-2. URL https://doi.org/10.1007/s00429-020-02142-2http://www.ncbi.nlm.nih.gov/pubmed/32936342http://www.pubmedcentral.nih.gov/articlerender.fcgi?artid=PMC7544728.

D H Hubel and T N Wiesel. Shape and arrangement of columns in cat's striate cortex. *The Journal of physiology*, 165(3):559–68, mar 1963. ISSN 0022-3751. doi: 10.1113/jphysiol.1963.sp007079. URL http://www.ncbi.nlm.nih.gov/pubmed/13955384http://www.pubmedcentral.nih.gov/articlerender.fcgi?artid=PMC1359325.

Laurentius Huber, Daniel A. Handwerker, David C. Jangraw, Gang Chen, Andrew Hall, Carsten Stüber, Javier Gonzalez-Castillo, Dimo Ivanov, Sean Marrett, Maria Guidi, Jozien Goense, Benedikt A. Poser, and Peter A. Bandettini. High-Resolution CBV-fMRI Allows Mapping of Laminar Activity and Connectivity of Cortical Input and Output in Human M1. *Neuron*, 96(6):1253–1263.e7, 2017. ISSN 1097-4199. doi: 10.1016/j.neuron.2017.11.005. URL http://www.ncbi.nlm.nih.gov/pubmed/29224727http://www.pubmedcentral.nih.gov/articlerender.fcgi?artid=PMC5739950.

G. W. Huntley and E. G. Jones. Relationship of intrinsic connections to forelimb movement representations in monkey motor cortex: A correlative anatomic and physiological study. *Journal of Neurophysiology*, 66(2):390–413, 1991. ISSN 00223077. doi: 10.1152/jn.1991.66.2.390.

R. Matthew Hutchison and Stefan Everling. Monkey in the middle: why non-human primates are needed to bridge the gap in resting-state investigations. *Frontiers in Neuroanatomy*, 6(JULY 2012):1–19, 2012. ISSN 1662-5129. doi: 10.3389/fnana.2012.00029. URL http://journal.frontiersin.org/article/10.3389/fnana.2012.00029/abstract.

R Matthew Hutchison, Melina Hutchison, Kathryn Y. Manning, Ravi S. Menon, and Stefan Everling. Isoflurane induces dose-dependent alterations in the cortical connectivity profiles and dynamic properties of the brain's functional architecture. *Human brain mapping*, 35(12):5754–75, dec 2014. ISSN 1097-0193. doi: 10.1002/hbm.22583. URL http://www.ncbi.nlm.nih.gov/pubmed/25044934http://www.pubmedcentral.nih.gov/articlerender.fcgi?artid=PMC6869297.

Lucas G S Jeub, Olaf Sporns, and Santo Fortunato. Multiresolution Consensus Clustering in Networks. *Scientific reports*, 8(1):3259, 2018. ISSN 2045-2322. doi: 10.1038/s41598-018-21352-7. URL http://dx.doi.org/10.1038/s41598-018-21352-7http://www.ncbi.nlm.nih.gov/pubmed/29459635http://www.pubmedcentral.nih.gov/articlerender.fcgi?artid=PMC5818657.

B. A. Johnson and R. D. Frostig. Long, intrinsic horizontal axons radiating through and beyond rat barrel cortex have spatial distributions similar to horizontal spreads of activity evoked by whisker stimulation. *Brain Structure and Function*, 221(7):3617–3639, sep 2016. ISSN 18632661. doi: 10.1007/s00429-015-1123-7.

Jon H. Kaas, Randall J. Nelson, Mriganka Sur, Chia Sheng Lin, and Michael M. Merzenich. Multiple representations of the body within the primary somatosensory cortex of primates. *Science*, 204(4392):521–523, may 1979. ISSN 00368075. doi: 10.1126/science.107591.

Itamar Kahn, Mitul Desai, Ulf Knoblich, Jacob Bernstein, Michael Henninger, Ann M. Graybiel, Edward S. Boyden, Randy L. Buckner, and Christopher I. Moore. Characterization of the functional MRI response temporal linearity via optical control of neocortical pyramidal neurons. *The Journal of neuroscience : the official journal of the Society for Neuroscience*, 31(42):15086–91, oct 2011. ISSN 1529-2401. doi: 10.1523/JNEUROSCI.0007-11.2011. URL `http://www.ncbi.nlm.nih.gov/pubmed/22016542http://www.pubmedcentral.nih.gov/articlerender.fcgi?artid=PMC3225054`.

Asaf Keller. Intrinsic Synaptic Organization of the Motor Cortex Intrinsic Synaptic Organization of. *Cerebral Cortex*, 3:430–441, 1993. doi: 10.1093/cercor/3.5.430.

Asaf Keller and Hiroshi Asanuma. Synaptic relationships involving local axon collaterals of pyramidal neurons in the cat motor cortex. *Journal of Comparative Neurology*, 336(2):229–242, 1993. ISSN 10969861. doi: 10.1002/cne.903360206.

Herbert P. Killackey. Anatomical evidence for cortical subdivisions based on vertically discrete thalamic projections from the ventral posterior nucleus to cortical barrels in the rat. *Brain Research*, 51(C):326–331, 1973. ISSN 00068993. doi: 10.1016/0006-8993(73)90383-1.

Dae-Shik Kim, Timothy Q. Duong, and Seong-Gi Kim. High-resolution mapping of iso-orientation columns by fMRI. *Nature Neuroscience*, 3(2):164–169, feb 2000. ISSN 1097-6256. doi: 10.1038/72109. URL `http://www.ncbi.nlm.nih.gov/pubmed/10649572http://www.nature.com/articles/nn0200_164`.

Vesa Kiviniemi, Juha-Heikki Kantola, Jukka Jauhiainen, Aapo Hyvärinen, and Osmo Tervonen. Independent component analysis of nondeterministic fMRI signal sources. *NeuroImage*, 19(2 Pt 1):253–60, jun 2003. ISSN 1053-8119. doi: 10.1016/s1053-8119(03)00097-1. URL `http://www.ncbi.nlm.nih.gov/pubmed/12814576`.

P. Christiaan Klink, Jean-François Aubry, Vincent P. Ferrera, Andrew S. Fox, Sean Froudist-Walsh, Béchir Jarraya, Elisa E. Konofagou, Richard J. Krauzlis, Adam Messinger, Anna S. Mitchell, Michael Ortiz-Rios, Hiroyuki Oya, Angela C. Roberts, Anna Wang Roe, Matthew F S Rushworth, Jérôme Sallet, Michael Christoph Schmid, Charles E. Schroeder, Jordy Tasserie, Doris Y. Tsao, Lynn Uhrig, Wim Vanduffel, Melanie Wilke, Igor Kagan, and Christopher I. Petkov. Combining brain perturbation and neuroimaging in non-human primates. *NeuroImage*, 235(March):118017, 2021. ISSN 1095-9572. doi: 10.1016/j.neuroimage.2021.118017. URL `https://doi.org/10.1016/j.neuroimage.2021.118017http://www.ncbi.nlm.nih.gov/pubmed/33794355`.

Sreekanth Kura, Hongyu Xie, Buyin Fu, Cenk Ayata, David A. Boas, and Sava Sakadžić. Intrinsic optical signal imaging of the blood volume changes is sufficient for mapping the resting state functional connectivity in the rodent cortex. *Journal of neural engineering*, 15(3):035003, 2018. ISSN 1741-2552. doi: 10.1088/

1741-2552/aaafe4. URL http://www.ncbi.nlm.nih.gov/pubmed/29451130http://www.pubmedcentral.nih.gov/articlerender.fcgi?artid=PMC5927826.

H. C. Kwan, W. A. MacKay, J. T. Murphy, and Y. C. Wong. Spatial organization of precentral cortex in awake primates. II. Motor outputs. *Journal of neurophysiology*, 41(5):1120–31, sep 1978. ISSN 0022-3077. doi: 10.1152/jn.1978.41.5.1120. URL http://www.physiology.org/doi/10.1152/jn.1978.41.5.1120http://www.ncbi.nlm.nih.gov/pubmed/100584.

K K Kwong, J W Belliveau, D A Chesler, I E Goldberg, R M Weisskoff, B P Poncelet, D N Kennedy, B E Hoppel, M S Cohen, and R Turner. Dynamic magnetic resonance imaging of human brain activity during primary sensory stimulation. *Proceedings of the National Academy of Sciences of the United States of America*, 89(12):5675–9, jun 1992. ISSN 0027-8424. doi: 10.1073/pnas.89.12.5675. URL http://www.ncbi.nlm.nih.gov/pubmed/1608978http://www.pubmedcentral.nih.gov/articlerender.fcgi?artid=PMC49355.

R. H. LaMotte and V. B. Mountcastle. Disorders in somesthesis following lesions of parietal lobe. *Journal of Neurophysiology*, 42(2):400–419, 1979. ISSN 00223077. doi: 10.1152/jn.1979.42.2.400.

Jose L. Lanciego and Floris G. Wouterlood. Neuroanatomical tract-tracing techniques that did go viral. *Brain structure and function*, 225(4):1193–1224, may 2020. ISSN 1863-2661. doi: 10.1007/s00429-020-02041-6. URL http://www.ncbi.nlm.nih.gov/pubmed/21782932http://www.ncbi.nlm.nih.gov/pubmed/32062721http://www.pubmedcentral.nih.gov/articlerender.fcgi?artid=PMC7271020.

Chia-Chi Liao, Omar A. Gharbawie, Huixin Qi, and Jon H. Kaas. Cortical connections to single digit representations in area 3b of somatosensory cortex in squirrel monkeys and prosimian galagos. *The Journal of comparative neurology*, 521(16):3768–90, nov 2013. ISSN 1096-9861. doi: 10.1002/cne.23377. URL http://www.ncbi.nlm.nih.gov/pubmed/23749740http://www.pubmedcentral.nih.gov/articlerender.fcgi?artid=PMC4000754.

Diana H. Lim, Jeffrey LeDue, Majid H. Mohajerani, Matthieu P. Vanni, and Timothy H. Murphy. Optogenetic approaches for functional mouse brain mapping. *Frontiers in Neuroscience*, 7(7 APR):1–15, 2013. ISSN 16624548. doi: 10.3389/fnins.2013.00054.

Cirong Liu, Frank Q Ye, John D Newman, Diego Szczupak, Xiaoguang Tian, Cecil Chern-Chyi Yen, Piotr Majka, Daniel Glen, Marcello G P Rosa, David A Leopold, and Afonso C Silva. A resource for the detailed 3D mapping of white matter pathways in the marmoset brain. *Nature neuroscience*, 23(2):271–280, 2020. ISSN 1546-1726. doi: 10.1038/s41593-019-0575-0. URL http://www.ncbi.nlm.nih.gov/pubmed/31932765http://www.pubmedcentral.nih.gov/articlerender.fcgi?artid=PMC7007400.

Junjie V. Liu, Yoshiyuki Hirano, George C. Nascimento, Bojana Stefanovic, David A. Leopold, and Afonso C. Silva. fMRI in the awake marmoset: somatosensory-evoked responses, functional connectivity, and comparison with propofol anesthesia. *NeuroImage*,

78:186–95, sep 2013a. ISSN 1095-9572. doi: 10.1016/j.neuroimage.2013.03.038. URL http://dx.doi.org/10.1016/j.neuroimage.2013.03.038http://www.ncbi.nlm.nih.gov/pubmed/23571417http://www.pubmedcentral.nih.gov/articlerender.fcgi?artid=PMC3778909.

Xiao Liu, Xiao Hong Zhu, Yi Zhang, and Wei Chen. The change of functional connectivity specificity in rats under various anesthesia levels and its neural origin. *Brain Topography*, 26(3):363–377, 2013b. ISSN 08960267. doi: 10.1007/s10548-012-0267-5.

Xiping Liu, Siveshigan Pillay, Rupeng Li, Jeannette A. Vizuete, Kimberly R. Pechman, Kathleen M. Schmainda, and Anthony G. Hudetz. Multiphasic modification of intrinsic functional connectivity of the rat brain during increasing levels of propofol. *NeuroImage*, 83:581–92, dec 2013c. ISSN 1095-9572. doi: 10.1016/j.neuroimage.2013.07.003. URL http://dx.doi.org/10.1016/j.neuroimage.2013.07.003http://www.ncbi.nlm.nih.gov/pubmed/23851326http://www.pubmedcentral.nih.gov/articlerender.fcgi?artid=PMC3815996.

M. S. Livingstone and D. H. Hubel. Specificity of intrinsic connections in primate primary visual cortex. *Journal of Neuroscience*, 4(11):2830–2835, 1984. ISSN 02706474. doi: 10.1523/jneurosci.04-11-02830.1984.

N. K. Logothetis, J. Pauls, M. Augath, T. Trinath, and A. Oeltermann. Neurophysiological investigation of the basis of the fMRI signal. *Nature*, 412(6843):150–7, jul 2001. ISSN 0028-0836. doi: 10.1038/35084005. URL http://www.ncbi.nlm.nih.gov/pubmed/11449264.

Nikos K. Logothetis, Mark Augath, Yusuke Murayama, Alexander Rauch, Fahad Sultan, Jozien Goense, Axel Oeltermann, and Hellmut Merkle. The effects of electrical microstimulation on cortical signal propagation. *Nature Neuroscience*, 13(10):1283–1291, 2010. ISSN 10976256. doi: 10.1038/nn.2631. URL http://www.nature.com/neuro/journal/v13/n10/pdf/nn.2631.pdf.

Haidong D. Lu and Anna W. Roe. Optical imaging of contrast response in Macaque monkey V1 and V2. *Cerebral Cortex*, 17(11):2675–2695, 2007. ISSN 10473211. doi: 10.1093/cercor/bhl177.

Haidong D. Lu and Anna W. Roe. Functional organization of color domains in V1 and V2 of macaque monkey revealed by optical imaging. *Cerebral cortex (New York, N.Y. : 1991)*, 18(3):516–33, mar 2008. ISSN 1460-2199. doi: 10.1093/cercor/bhm081. URL http://www.ncbi.nlm.nih.gov/pubmed/17576751http://www.pubmedcentral.nih.gov/articlerender.fcgi?artid=PMC2657473.

Jennifer S. Lund, Takashi Yoshioka, Jennifer S. Lund, Takashi Yoshioka, Jonathan B. Levitt, Jennifer S. Lund, and Jonathan B. Levitt. Comparison of intrinsic connectivity in different areas of macaque monkey cerebral cortex. *Cerebral Cortex*, 3(2):148–162, 1993. ISSN 14602199. doi: 10.1093/cercor/3.2.148.

Ying Ma, Mohammed A. Shaik, Mariel G. Kozberg, Sharon H. Kim, Jacob P. Portes, Dmitriy Timerman, and Elizabeth M. C. Hillman. Resting-state hemodynamics are spatiotemporally coupled to synchronized and symmetric neural activity in excitatory neurons. *Proceedings of the National Academy of Sciences of the United States of America*, 113(52):E8463–E8471, 2016. ISSN 1091-6490. doi: 10.1073/pnas.1525369113. URL http://www.pnas.org/lookup/doi/10.1073/pnas.1525369113http://www.ncbi.nlm.nih.gov/pubmed/27974609http://www.pubmedcentral.nih.gov/articlerender.fcgi?artid=PMC5206542.

R. Malach, Y. Amir, M. Harel, and A. Grinvald. Relationship between intrinsic connections and functional architecture revealed by optical imaging and in vivo targeted biocytin injections in primate striate cortex. *Proceedings of the National Academy of Sciences of the United States of America*, 90(22):10469–10473, nov 1993. ISSN 00278424. doi: 10.1073/pnas.90.22.10469.

Joanne A. Matsubara and D. P. Phillips. Intracortical connections and their physiological correlates in the primary auditory cortex (AI) of the cat. *Journal of Comparative Neurology*, 268(1):38–48, 1988. ISSN 10969861. doi: 10.1002/cne.902680105.

Teppei Matsui, Keita Tamura, Kenji W. Koyano, Daigo Takeuchi, Yusuke Adachi, Takahiro Osada, and Yasushi Miyashita. Direct comparison of spontaneous functional connectivity and effective connectivity measured by intracortical microstimulation: an fMRI study in macaque monkeys. *Cerebral cortex (New York, N.Y. : 1991)*, 21(10):2348–56, oct 2011. ISSN 1460-2199. doi: 10.1093/cercor/bhr019. URL http://www.ncbi.nlm.nih.gov/pubmed/21368090.

Andrei Mayer, Mary K L Baldwin, Dylan F. Cooke, Bruss R. Lima, Jeffrey Padberg, Gabriela Lewenfus, João G. Franca, and Leah Krubitzer. The Multiple Representations of Complex Digit Movements in Primary Motor Cortex Form the Building Blocks for Complex Grip Types in Capuchin Monkeys. *The Journal of neuroscience : the official journal of the Society for Neuroscience*, 39(34):6684–6695, 2019. ISSN 1529-2401. doi: 10.1523/JNEUROSCI.0556-19.2019. URL http://www.ncbi.nlm.nih.gov/pubmed/31235643http://www.pubmedcentral.nih.gov/articlerender.fcgi?artid=PMC6703879.

John E.W. Mayhew, Stephen Askew, Ying Zheng, John Porrill, G. W.Max Westby, Peter Redgrave, David M. Rector, and Ronald M. Harper. Cerebral vasomotion: a 0.1-Hz oscillation in reflected light imaging of neural activity. *NeuroImage*, 4(3 Pt 1):183–93, dec 1996. ISSN 1053-8119. doi: 10.1006/nimg.1996.0069. URL http://www.ncbi.nlm.nih.gov/pubmed/9345508.

Marina Meilă. Comparing clusterings—an information based distance. *Journal of Multivariate Analysis*, 98(5):873–895, may 2007. ISSN 0047259X. doi: 10.1016/j.jmva.2006.11.013. URL https://linkinghub.elsevier.com/retrieve/pii/S0047259X06002016.

Michael M. Merzenich, Jon H. Kaas, Mriganka Sur, and Chia-Sheng -S Lin. Double representation of the body surface within cytoarchitectonic area 3b and 1 in "SI" in the owl

monkey (aotus trivirgatus). *Journal of Comparative Neurology*, 181(1):41–73, sep 1978. ISSN 10969861. doi: 10.1002/cne.901810104.

E Moberg. Criticism and study of methods for examining sensibility in the hand. *Neurology*, 12:8–19, jan 1962. ISSN 0028-3878. doi: 10.1212/wnl.12.1.8. URL http://www.ncbi.nlm.nih.gov/pubmed/14474916.

Sebastian Moeller, Winrich A. Freiwald, and Doris Y. Tsao. Patches with links: A unified system for processing faces in the macaque temporal lobe. *Science*, 320(5881):1355–1359, jun 2008. ISSN 00368075. doi: 10.1126/science.1157436.

Majid H. Mohajerani, David A. McVea, Matthew Fingas, and Timothy H. Murphy. Mirrored bilateral slow-wave cortical activity within local circuits revealed by fast bihemispheric voltage-sensitive dye imaging in anesthetized and awake mice. *The Journal of neuroscience : the official journal of the Society for Neuroscience*, 30(10):3745–51, mar 2010. ISSN 1529-2401. doi: 10.1523/JNEUROSCI.6437-09.2010. URL http://www.ncbi.nlm.nih.gov/pubmed/20220008http://www.pubmedcentral.nih.gov/articlerender.fcgi?artid=PMC6632233.

Majid H. Mohajerani, Allen W. Chan, Mostafa Mohsenvand, Jeffrey LeDue, Rui Liu, David A. McVea, Jamie D. Boyd, Yu Tian Wang, Mark Reimers, and Timothy H. Murphy. Spontaneous cortical activity alternates between motifs defined by regional axonal projections. *Nature neuroscience*, 16(10):1426–35, oct 2013. ISSN 1546-1726. doi: 10.1038/nn.3499. URL http://www.ncbi.nlm.nih.gov/pubmed/23974708http://www.pubmedcentral.nih.gov/articlerender.fcgi?artid=PMC3928052.

Joël Monzée, Yves Lamarre, and Allan M. Smith. The effects of digital anesthesia on force control using a precision grip. *Journal of Neurophysiology*, 89(2):672–683, 2003. ISSN 00223077. doi: 10.1152/jn.00434.2001.

Vernon B. Mountcastle. The columnar organization of the neocortex. *Brain : a journal of neurology*, 120 (Pt 4(4):701–22, apr 1997. ISSN 0006-8950. doi: 10.1093/brain/120.4.701. URL http://www.ncbi.nlm.nih.gov/pubmed/9153131.

K F Muakkassa and P L Strick. Frontal lobe inputs to primate motor cortex: evidence for four somatotopically organized 'premotor' areas. *Brain research*, 177(1):176–82, nov 1979. ISSN 0006-8993. doi: 10.1016/0006-8993(79)90928-4. URL http://www.ncbi.nlm.nih.gov/pubmed/115545.

Kevin Murphy and Michael D. Fox. Towards a consensus regarding global signal regression for resting state functional connectivity MRI. *NeuroImage*, 154(November 2016):169–173, 2017. ISSN 1095-9572. doi: 10.1016/j.neuroimage.2016.11.052. URL http://dx.doi.org/10.1016/j.neuroimage.2016.11.052http://www.ncbi.nlm.nih.gov/pubmed/27888059http://www.pubmedcentral.nih.gov/articlerender.fcgi?artid=PMC5489207.

László Négyessy, Emese Pálfi, Mária Ashaber, Cory Palmer, Balázs Jákli, Robert M. Friedman, Li M. Chen, and Anna W. Roe. Intrinsic horizontal connections process global tactile features in the primary somatosensory cortex: neuroanatomical evidence. *The Journal of comparative neurology*, 521(12):2798–817, aug 2013. ISSN 1096-9861. doi: 10.1002/cne.23317. URL http://www.ncbi.nlm.nih.gov/pubmed/23436325http://www.pubmedcentral.nih.gov/articlerender.fcgi?artid=PMC4157923.

Randolph J. Nudo and Garrett W. Milliken. Reorganization of movement representations in primary motor cortex following focal ischemic infarcts in adult squirrel monkeys. *Journal of Neurophysiology*, 75(5):2144–2149, 1996. ISSN 00223077. doi: 10.1152/jn.1996.75.5.2144. URL http://www.physiology.org/doi/10.1152/jn.1996.75.5.2144.

S. Ogawa, D. W. Tank, R. Menon, J. M. Ellermann, S. G. Kim, H. Merkle, and K. Ugurbil. Intrinsic signal changes accompanying sensory stimulation: functional brain mapping with magnetic resonance imaging. *Proceedings of the National Academy of Sciences of the United States of America*, 89(13):5951–5, jul 1992. ISSN 0027-8424. doi: 10.1073/pnas.89.13.5951. URL http://www.ncbi.nlm.nih.gov/pubmed/1631079http://www.pubmedcentral.nih.gov/articlerender.fcgi?artid=PMC402116.

Seiji Ogawa, Tso-Ming -M Lee, Asha S. Nayak, and Paul Glynn. Oxygenation-sensitive contrast in magnetic resonance image of rodent brain at high magnetic fields. *Magnetic resonance in medicine*, 14(1):68–78, apr 1990. ISSN 0740-3194. doi: 10.1002/mrm.1910140108. URL http://www.ncbi.nlm.nih.gov/pubmed/2161986.

Jeffrey Padberg, Elizabeth Disbrow, and Leah Krubitzer. The organization and connections of anterior and posterior parietal cortex in titi monkeys: Do new world monkeys have an area 2? *Cerebral Cortex*, 15(12):1938–1963, 2005. ISSN 10473211. doi: 10.1093/cercor/bhi071.

Michael C. Park, Abderraouf Belhaj-Saïf, Michael Gordon, and Paul D. Cheney. Consistent features in the forelimb representation of primary motor cortex in rhesus macaques. *The Journal of neuroscience : the official journal of the Society for Neuroscience*, 21 (8):2784–92, apr 2001. ISSN 1529-2401. doi: 10.1523/jneurosci.21-08-02784.2001. URL http://www.jneurosci.org/content/21/8/2784.short%5Cnhttp://www.ncbi.nlm.nih.gov/pubmed/11306630http://www.ncbi.nlm.nih.gov/pubmed/11306630http://www.pubmedcentral.nih.gov/articlerender.fcgi?artid=PMC6762507.

Yu Cheng Pei, Steven S. Hsiao, James C. Craig, and Sliman J. Bensmaia. Shape invariant coding of motion direction in somatosensory cortex. *PLoS Biology*, 8(2), 2010. ISSN 15449173. doi: 10.1371/journal.pbio.1000305.

Wilder Penfield and Edwin Boldrey. Somatic motor and sensory representation in the cerebral cortex of man as studied by electrical stimulation. *Brain*, 60(4):389–443, 1937. ISSN 00068950. doi: 10.1093/brain/60.4.389.

Gita Prabhu, Hideki Shimazu, Gabriella Cerri, Thomas Brochier, Rachel L. Spinks, Marc A. Maier, and Roger N. Lemon. Modulation of primary motor cortex outputs from ven-

tral premotor cortex during visually guided grasp in the macaque monkey. *The Journal of physiology*, 587(Pt 5):1057–69, mar 2009. ISSN 1469-7793. doi: 10.1113/jphysiol.2008.165571. URL http://www.ncbi.nlm.nih.gov/pubmed/19139043http://www.pubmedcentral.nih.gov/articlerender.fcgi?artid=PMC2673775.

Elsie Premereur, Jessica Taubert, Peter Janssen, Rufin Vogels, and Wim Vanduffel. Effective Connectivity Reveals Largely Independent Parallel Networks of Face and Body Patches. *Current biology : CB*, 26(24):3269–3279, dec 2016. ISSN 1879-0445. doi: 10.1016/j.cub.2016.09.059. URL http://dx.doi.org/10.1016/j.cub.2016.09.059http://www.ncbi.nlm.nih.gov/pubmed/27866893.

Elsie Premereur, Peter Janssen, and Wim Vanduffel. Functional MRI in Macaque Monkeys during Task Switching. *The Journal of neuroscience : the official journal of the Society for Neuroscience*, 38(50):10619–10630, 2018. ISSN 1529-2401. doi: 10.1523/JNEUROSCI.1539-18.2018. URL http://www.ncbi.nlm.nih.gov/pubmed/30355629http://www.pubmedcentral.nih.gov/articlerender.fcgi?artid=PMC6580658.

S Ramón y Cajal. *Comparative Study of the Sensory Areas of the Human Cortex*. 1899.

J. C. Rothwell, M. M. Traub, B. L. Day, J. A. Obeso, P. K. Thomas, and C. D. Marsden. Manual motor performance in a deafferented man. *Brain*, 105(3):515–542, 1982. ISSN 00068950. doi: 10.1093/brain/105.3.515.

D. E. Sakas, K. Charnvises, L. F. Borges, and N. T. Zervas. Biologically inert synthetic dural substitutes. Appraisal of a medical-grade aliphatic polyurethane and a polysiloxane-carbonate block copolymer. *Journal of neurosurgery*, 73 (6):936–41, dec 1990. ISSN 0022-3085. doi: 10.3171/jns.1990.73.6.0936. URL http://thejns.org/doi/pdf/10.3171/jns.1990.73.6.0936%5Cnhttp://www.ncbi.nlm.nih.gov/pubmed/2230977http://www.ncbi.nlm.nih.gov/pubmed/2230977.

Marc H Schieber and Lyndon S Hibbard. How somatotopic is the motor cortex hand area? *Science (New York, N.Y.)*, 261(5120):489–92, jul 1993. ISSN 0036-8075. doi: 10.1126/science.8332915. URL http://www.ncbi.nlm.nih.gov/pubmed/8332915.

Marc H. M.H. Schieber. Constraints on somatotopic organization in the primary motor cortex. *Journal of neurophysiology*, 86(5):2125–43, 2001. ISSN 00223077. doi: 10.1152/jn.2001.86.5.2125. URL http://www.physiology.org/doi/10.1152/jn.2001.86.5.2125http://www.ncbi.nlm.nih.gov/pubmed/11698506.

Kurt G. Schilling, Yurui Gao, Matthew Christian, Vaibhav Janve, Iwona Stepniewska, Bennett A. Landman, and Adam W. Anderson. A Web-Based Atlas Combining MRI and Histology of the Squirrel Monkey Brain. *Neuroinformatics*, 17(1):131–145, 2019. ISSN 1559-0089. doi: 10.1007/s12021-018-9391-z. URL http://www.ncbi.nlm.nih.gov/pubmed/30006920http://www.pubmedcentral.nih.gov/articlerender.fcgi?artid=PMC6330248.

Marieke L. Schölvinck, Alexander Maier, Frank Q. Ye, Jeff H. Duyn, and David A. Leopold. Neural basis of global resting-state fMRI activity. *Proceedings of the National Academy of Sciences of the United States of America*, 107(22):10238–10243, 2010. ISSN 00278424. doi: 10.1073/pnas.0913110107.

B. J. Sessle and M. Wiesendanger. Structural and functional definition of the motor cortex in the monkey (Macaca fascicularis). *The Journal of physiology*, 323 (1):245–65, feb 1982. ISSN 0022-3751. doi: 10.1113/jphysiol.1982.sp014071. URL https://onlinelibrary.wiley.com/doi/10.1113/jphysiol.1982.sp014071http://www.ncbi.nlm.nih.gov/pubmed/7097574http://www.pubmedcentral.nih.gov/articlerender.fcgi?artid=PMC1250355.

Kelly Shen, Gleb Bezgin, R Matthew Hutchison, Joseph S Gati, Ravi S Menon, Stefan Everling, and Anthony R McIntosh. Information processing architecture of functionally defined clusters in the macaque cortex. *The Journal of neuroscience : the official journal of the Society for Neuroscience*, 32(48):17465–76, nov 2012. ISSN 1529-2401. doi: 10.1523/JNEUROSCI.2709-12.2012. URL http://www.ncbi.nlm.nih.gov/pubmed/23197737http://www.pubmedcentral.nih.gov/articlerender.fcgi?artid=PMC6621872.

Kelly Shen, Bratislav Mišić, Ben N Cipollini, Gleb Bezgin, Martin Buschkuehl, R Matthew Hutchison, Susanne M Jaeggi, Ethan Kross, Scott J Peltier, Stefan Everling, John Jonides, Anthony R McIntosh, and Marc G Berman. Stable long-range interhemispheric coordination is supported by direct anatomical projections. *Proceedings of the National Academy of Sciences of the United States of America*, 112(20):6473–8, may 2015. ISSN 1091-6490. doi: 10.1073/pnas.1503436112. URL http://www.ncbi.nlm.nih.gov/pubmed/25941372http://www.pubmedcentral.nih.gov/articlerender.fcgi?artid=PMC4443345.

Sameer A. Sheth, Masahito Nemoto, Michael Guiou, Melissa Walker, Nader Pouratian, Nathan Hageman, and Arthur W. Toga. Columnar specificity of microvascular oxygenation and volume responses: implications for functional brain mapping. *The Journal of neuroscience : the official journal of the Society for Neuroscience*, 24(3):634–41, jan 2004. ISSN 1529-2401. doi: 10.1523/JNEUROSCI.4526-03.2004. URL http://www.ncbi.nlm.nih.gov/pubmed/14736849http://www.pubmedcentral.nih.gov/articlerender.fcgi?artid=PMC6729264.

Zhaoyue Shi, Ruiqi Wu, Pai-Feng Yang, Feng Wang, Tung-Lin Wu, Arabinda Mishra, Li Min Chen, and John C. Gore. High spatial correspondence at a columnar level between activation and resting state fMRI signals and local field potentials. *Proceedings of the National Academy of Sciences of the United States of America*, 114(20):5253–5258, 2017. ISSN 1091-6490. doi: 10.1073/pnas.1620520114. URL http://www.ncbi.nlm.nih.gov/pubmed/28461461http://www.pubmedcentral.nih.gov/articlerender.fcgi?artid=PMC5441782.

Amir Shmuel and David A. Leopold. Neuronal correlates of spontaneous fluctuations in fMRI

signals in monkey visual cortex: Implications for functional connectivity at rest. *Human Brain Mapping*, 29(7):751–761, jul 2008. ISSN 10659471. doi: 10.1002/hbm.20580. URL https://onlinelibrary.wiley.com/doi/10.1002/hbm.20580.

I Stepniewska, T M Preuss, and J H Kaas. Architectonics, somatotopic organization, and ipsilateral cortical connections of the primary motor area (M1) of owl monkeys. *The Journal of comparative neurology*, 330(2):238–71, apr 1993. ISSN 0021-9967. doi: 10.1002/cne.903300207. URL http://www.ncbi.nlm.nih.gov/pubmed/7684050.

Iwona Stepniewska, Pei-Chun Fang, and Jon H Kaas. Microstimulation reveals specialized subregions for different complex movements in posterior parietal cortex of prosimian galagos. *Proceedings of the National Academy of Sciences of the United States of America*, 102 (13):4878–83, 2005. ISSN 0027-8424. doi: 10.1073/pnas.0501048102.

Iwona Stepniewska, Todd M. Preuss, and Jon H. Kaas. Ipsilateral cortical connections of dorsal and ventral premotor areas in New World owl monkeys. *The Journal of comparative neurology*, 495(6):691–708, apr 2006. ISSN 0021-9967. doi: 10.1002/cne.20906. URL http://www.ncbi.nlm.nih.gov/pubmed/16506197http://www.pubmedcentral.nih.gov/articlerender.fcgi?artid=PMC6503658.

Iwona Stepniewska, Pei-Chun Y Fang, and Jon H. Kaas. Organization of the posterior parietal cortex in galagos: I. Functional zones identified by microstimulation. *The Journal of comparative neurology*, 517(6):765–82, dec 2009. ISSN 1096-9861. doi: 10.1002/cne.22181. URL http://www.ncbi.nlm.nih.gov/pubmed/19852065http://www.pubmedcentral.nih.gov/articlerender.fcgi?artid=PMC3697764.

Iwona Stepniewska, Robert M. Friedman, Omar A. Gharbawie, Christina M. Cerkevich, Anna W. Roe, and Jon H. Kaas. Optical imaging in galagos reveals parietal-frontal circuits underlying motor behavior. *Proceedings of the National Academy of Sciences of the United States of America*, 108(37):E725–32, sep 2011. ISSN 1091-6490. doi: 10.1073/pnas.1109925108. URL http://www.ncbi.nlm.nih.gov/pubmed/21873212http://www.pubmedcentral.nih.gov/articlerender.fcgi?artid=PMC3174626.

S D Stoney, W D Thompson, and H Asanuma. Excitation of pyramidal tract cells by intracortical microstimulation: effective extent of stimulating current. *Journal of neurophysiology*, 31(5):659–669, 1968. ISSN 0022-3077. doi: 10.1152/jn.1968.31.5.659.

P. L. Strick and J. B. Preston. Two representations of the hand in area 4 of a primate. I. Motor output organization. *Journal of Neurophysiology*, 48(1):139–149, 1982. ISSN 00223077. doi: 10.1152/jn.1982.48.1.139.

Peter L. Strick. Multiple sources of thalamic input to the primate motor cortex. *Brain Research*, 88(2):372–377, 1975. ISSN 00068993. doi: 10.1016/0006-8993(75)90402-3.

Mriganka Sur, R. J. Nelson, and J. H. Kaas. Representations of the body surface in cortical areas 3b and 1 of squirrel monkeys: comparisons with other primates. *The Journal of com-*

parative neurology, 211(2):177–92, oct 1982. ISSN 0021-9967. doi: 10.1002/cne.902110207. URL http://www.ncbi.nlm.nih.gov/pubmed/7174889.

Mriganka Sur, Preston E. Garraghty, and Charles J. Bruce. Somatosensory cortex in macaque monkeys: laminar differences in receptive field size in areas 3b and 1. *Brain Research*, 342 (2):391–395, 1985. ISSN 00068993. doi: 10.1016/0006-8993(85)91144-8.

John Thomas, Dixit Sharma, Sounak Mohanta, and Neeraj Jain. Resting-State functional networks of different topographic representations in the somatosensory cortex of macaque monkeys and humans. *NeuroImage*, 228(July 2020):117694, 2021. ISSN 1095-9572. doi: 10.1016/j.neuroimage.2020.117694. URL https://doi.org/10.1016/j.neuroimage.2020.117694http://www.ncbi.nlm.nih.gov/pubmed/33385552.

Andreas S. Tolias, Fahad Sultan, Mark Augath, Axel Oeltermann, Edward J. Tehovnik, Peter H. Schiller, and Nikos K. Logothetis. Mapping cortical activity elicited with electrical microstimulation using fMRI in the macaque. *Neuron*, 48(6):901–911, 2005. ISSN 08966273. doi: 10.1016/j.neuron.2005.11.034.

J Michael Tyszka, Daniel P. Kennedy, Ralph Adolphs, and Lynn K. Paul. Intact bilateral resting-state networks in the absence of the corpus callosum. *The Journal of neuroscience : the official journal of the Society for Neuroscience*, 31(42):15154–62, oct 2011. ISSN 1529-2401. doi: 10.1523/JNEUROSCI.1453-11.2011. URL http://www.ncbi.nlm.nih.gov/pubmed/22016549http://www.pubmedcentral.nih.gov/articlerender.fcgi?artid=PMC3221732.

Martijn P van den Heuvel, René C W Mandl, René S. Kahn, and Hilleke E Hulshoff Pol. Functionally linked resting-state networks reflect the underlying structural connectivity architecture of the human brain. *Human brain mapping*, 30(10):3127–41, oct 2009. ISSN 1097-0193. doi: 10.1002/hbm.20737. URL http://www.ncbi.nlm.nih.gov/pubmed/19235882http://www.pubmedcentral.nih.gov/articlerender.fcgi?artid=PMC6870902.

Matthieu P. Vanni, Allen W. Chan, Matilde Balbi, Gergely Silasi, and Timothy H. Murphy. Mesoscale Mapping of Mouse Cortex Reveals Frequency-Dependent Cycling between Distinct Macroscale Functional Modules. *The Journal of neuroscience : the official journal of the Society for Neuroscience*, 37(31):7513–7533, 2017. ISSN 1529-2401. doi: 10.1523/JNEUROSCI.3560-16.2017. URL http://www.ncbi.nlm.nih.gov/pubmed/28674167http://www.pubmedcentral.nih.gov/articlerender.fcgi?artid=PMC6596702.

Anil K. Vasireddi, Alberto L. Vazquez, David E. Whitney, Mitsuhiro Fukuda, and Seong-Gi Kim. Functional Connectivity of Resting Hemodynamic Signals in Submillimeter Orientation Columns of the Visual Cortex. *Brain connectivity*, 6(8):596–606, 2016. ISSN 2158-0022. doi: 10.1089/brain.2015.0414. URL http://online.liebertpub.com/doi/10.1089/brain.2015.0414http://www.ncbi.nlm.nih.gov/pubmed/27461173http://www.pubmedcentral.nih.gov/articlerender.fcgi?artid=PMC5069732.

Alberto L. Vazquez, Mitsuhiro Fukuda, Justin C. Crowley, and Seong-Gi Kim. Neural and hemodynamic responses elicited by forelimb- and photo-stimulation in channelrhodopsin-2 mice: insights into the hemodynamic point spread function. *Cerebral cortex (New York, N.Y. : 1991)*, 24(11):2908–19, nov 2014. ISSN 1460-2199. doi: 10.1093/cercor/bht147. URL http://www.ncbi.nlm.nih.gov/pubmed/23761666http://www.pubmedcentral.nih.gov/articlerender.fcgi?artid=PMC4193461.

J. L. Vincent, G. H. Patel, M. D. Fox, A. Z. Snyder, J. T. Baker, D. C. Van Essen, J. M. Zempel, L. H. Snyder, M. Corbetta, and M. E. Raichle. Intrinsic functional architecture in the anaesthetized monkey brain. *Nature*, 447(7140):83–86, may 2007. ISSN 0028-0836. doi: 10.1038/nature05758. URL http://www.nature.com/articles/nature05758.

Zheng Wang, Li Min Chen, László Négyessy, Robert M. Friedman, Arabinda Mishra, John C. Gore, and Anna W. Roe. The relationship of anatomical and functional connectivity to resting-state connectivity in primate somatosensory cortex. *Neuron*, 78(6):1116–26, jun 2013. ISSN 1097-4199. doi: 10.1016/j.neuron.2013.04.023. URL http://www.ncbi.nlm.nih.gov/pubmed/23791200http://www.pubmedcentral.nih.gov/articlerender.fcgi?artid=PMC3723346.

David S. Weiss and Asaf Keller. Specific patterns of intrinsic connections between representation zones in the rat motor cortex. *Cerebral Cortex*, 4(2):205–214, 1994. ISSN 10473211. doi: 10.1093/cercor/4.2.205.

W. I. Welker, Robert M. Benjamin, Raymond C. Miles, and Clinton N. Woolsey. MOTOR EFFECTS OF STIMULATION OF CEREBRAL CORTEX OF SQUIRREL MONKEY (SAIMIRI SCIUREUS). *Journal of Neurophysiology*, 20(4):347–364, jul 1957. ISSN 0022-3077. doi: 10.1152/jn.1957.20.4.347. URL http://www.ncbi.nlm.nih.gov/pubmed/13439407https://www.physiology.org/doi/10.1152/jn.1957.20.4.347.

Brian R. White, Adam Q. Bauer, Abraham Z. Snyder, Bradley L. Schlaggar, Jin-Moo Lee, and Joseph P. Culver. Imaging of functional connectivity in the mouse brain. *PloS one*, 6(1):e16322, jan 2011. ISSN 1932-6203. doi: 10.1371/journal.pone.0016322. URL http://www.ncbi.nlm.nih.gov/pubmed/21283729http://www.pubmedcentral.nih.gov/articlerender.fcgi?artid=PMC3024435.

B T Thomas Yeo, Fenna M. Krienen, Jorge Sepulcre, Mert R. Sabuncu, Danial Lashkari, Marisa Hollinshead, Joshua L. Roffman, Jordan W. Smoller, Lilla Zöllei, Jonathan R. Polimeni, Bruce Fischl, Hesheng Liu, and Randy L. Buckner. The organization of the human cerebral cortex estimated by intrinsic functional connectivity. *Journal of neurophysiology*, 106(3):1125–65, sep 2011. ISSN 1522-1598. doi: 10.1152/jn.00338.2011. URL http://www.ncbi.nlm.nih.gov/pubmed/21653723http://www.pubmedcentral.nih.gov/articlerender.fcgi?artid=PMC3174820.